

Cà foscari University

**STRUCTURAL CHARACTERIZATIONS AND
SPECTROSCOPIC INVESTIGATIONS ON THE POSSIBLE
ANTIBACTERIAL ACTIVITY OF DIFFERENTLY
SURFACE-TREATED SILICON NITRIDES FOR DENTAL
APPLICATIONS**

Master's Degree programme – Second Cycle (D.M. 270/2004) in

Science and Technologies of Bio- and Nano-Materials

Final Thesis

Supervisors:

Ch. Prof. Pietro Riello

Ch. Prof. Giuseppe Pezzotti

Graduant:

Greta Baggio

844921

Ceramic Physics Laboratory, Kyoto Institute of Technology, Sakyo-ku, Matsugasaki, 606-8585 Kyoto, Japan

Department of Dental Medicine, Graduate School of Medical Science, Kyoto Prefectural University of Medicine,
Kamigyo-ku, 602-8566 Kyoto, Japan

Department of Molecular Science and Nanosystems, Cà Foscari University of Venice, Via Torino 155/B, 30172 Venice-
Mestre, Italy

Academic Year 2014/2015

SUMMARY

SUMMARY	2
LIST OF FIGURES	4
LIST OF TABLES	7
ABBREVIATIONS	8
ABSTRACT	10
CHAPTER I: SILICON NITRIDE	11
1.1 Background	11
1.2 Fundamental properties	12
<i>1.2.1 Si₃N₄ production</i>	<i>12</i>
<i>1.2.2 Crystal structure</i>	<i>13</i>
<i>1.2.3 Material properties</i>	<i>15</i>
1.3 Applications	17
<i>1.3.1 Industrial applications</i>	<i>17</i>
<i>1.3.2 Medical applications</i>	<i>19</i>
CHAPTER II: BACTERIAL INTRODUCTION	21
2.1 Description of periodontal diseases	21
2.2 Oral bacteria	26
<i>2.2.1 Gram-positive and Gram-negative bacteria</i>	<i>26</i>
<i>2.2.2 The “red complex”</i>	<i>28</i>
CHAPTER III: EXPERIMENTAL TECHNIQUES	34
3.1 Molecular characterization	34
<i>3.1.1 Raman Spectroscopy</i>	<i>34</i>
3.2 Morphological characterization	37
<i>3.2.1 3D Laser-Scanning Confocal Microscope (CLSM or LSCM)</i>	<i>37</i>
<i>3.2.2 Scanning Electron Microscope (SEM)</i>	<i>39</i>
3.3 Structural characterization	41
<i>3.3.1 X-ray Diffraction (XRD)</i>	<i>41</i>
3.4 Chemical characterization	42
<i>3.4.1 Scanning Chemical Microscope (SCHEM™)</i>	<i>42</i>

CHAPTER IV: MATERIAL AND METHODS	43
4.1 Si₃N₄ material	43
4.1.1 <i>Sample preparation</i>	43
4.1.2 <i>Surface treatments description</i>	44
4.2 Bacterial strains preparation	45
4.2.1 <i>Porphyromonas gingivalis (ATCC 33277)</i>	45
4.2.2 <i>Treponema denticola (ATCC 35405) and Tannerella forsythia (ATCC 43037)</i>	47
4.3 Sample characterization methods	48
4.3.1 <i>Raman Spectroscopy</i>	48
4.3.2 <i>3D Laser-Scanning Confocal Microscope</i>	51
4.3.3 <i>Scanning Electron Microscope</i>	51
4.3.4 <i>X-ray Diffraction (XRD)</i>	51
4.3.5 <i>Fluorescence Microscopy</i>	52
4.3.6 <i>pH Microscopy</i>	52
CHAPTER V: RESULTS AND DISCUSSION	53
5.1 Si₃N₄ surface characterization	53
5.1.1 <i>Raman investigation and surface topography</i>	53
5.1.2 <i>XRD and SEM analyses</i>	59
5.2 Interaction of bacteria and Si₃N₄ surface	69
5.2.1 <i>Labeling the Raman of bacterial strains</i>	69
5.2.2 <i>Monitoring bacteria metabolism by Raman spectroscopy</i>	73
5.2.3 <i>Linking Si₃N₄ surface modulation to bacterial strains metabolism</i>	82
5.3 Fluorescence analysis of P. gingivalis bacterial cell	89
5.4 Chemical reactions at the surface of Si₃N₄ bioceramics	90
CHAPTER VI: CONCLUSION	96
REFERENCES	98

LIST OF FIGURES

Figure 1. Tetrahedral unit in Si ₃ N ₄ .	14
Figure 2. α-Si ₃ N ₄ . Green balls are Si, black are N.	14
Figure 3. β-Si ₃ N ₄ . Green balls are Si, black are N.	14
Figure 4. Si ₃ N ₄ bearing parts.	17
Figure 5. Si ₃ N ₄ medical devices.	19
Figure 6. Comparison between oral healthy and periodontal disease.	21
Figure 7. Difference between the two types of inflammatory disorders.	22
Figure 8. The American Academy of Periodontology Classification of a) gingivitis and b) periodontitis.	23
Figure 9. Three-layer periodontal health model. Inner layer: direct contributing factors; middle layer: oral environment and systemic factors; outer layer: personal factors.	25
Figure 10 a. Gram-positive cell envelope.	26
Figure 10 b. Gram-negative cell envelope.	27
Figure 11. Detailed representation of OM.	27
Figure 12. Components of LPS.	28
Figure 13. Dysbiosis during periodontitis development.	29
Figure 14. Transmission electron microscopy of <i>P. gingivalis</i> .	30
Figure 15. Transmission electron microscopy of <i>T. denticola</i> .	30
Figure 16. Transmission electron microscopy of <i>T. forsythia</i> . Bar = 1 μm.	31
Figure 17. Ultra-thin cross section of whole cell from <i>T. forsythia</i> .	32
Figure 18. Combination of <i>P. gingivalis</i> , <i>T. denticola</i> and <i>T. forsythia</i> found in subgingival plaque that had quantifiable by real-time PCR in 41 sites of 37 individuals previously diagnosed with periodontitis.	33
Figure 19. Diagram of the Rayleigh and Raman processes. Both the low energy (upward arrows) and the scattered energy (downward arrows) have much larger energies than the energy of a vibration.	35
Figure 20. Comparison between anti-Stokes and Stokes intensity lines.	36

Figure 21. Schematic Raman components.	37
Figure 22. Principle of confocal microscope.	38
Figure 23. Diagram of the various components of SEM.	40
Figure 24. T-64000 Raman spectrometer.	49
Figure 25. LabRAM ARAMIS spectroscopic system.	50
Figure 26. Schematic diagram of the production of Si ₃ N ₄ samples.	53
Figure 27. Typical Raman spectrum of β-Si ₃ N ₄ .	54
Figure 28. Raman spectra of β-Si ₃ N ₄ in the 150-250 cm ⁻¹ region, collected on: a) AF-Untreated, b) AF-HF, c) AF-N ₂ , and d) AF-Thermally oxidized.	54
Figure 29. Scanning laser micrographs of: a) AF-Untreated, b) AF-HF, c) AF-N ₂ , and d) AF-Thermally oxidized.	55
Figure 30. Raman spectra of β-Si ₃ N ₄ in the 150-250 cm ⁻¹ region, collected on: a) Pol-Untreated, b) Pol-HF, c) Pol-N ₂ , and d) Pol-Thermally oxidized.	56
Figure 31. Scanning laser micrographs on: a) Pol-Untreated, b) Pol-HF, c) Pol-N ₂ , and d) Pol-Thermally oxidized.	58, 59
Figure 32. XRD pattern of Pol-Untreated sample.	60
Figure 33. XRD pattern of Pol-HF sample.	60
Figure 34. XRD patterns of <i>polished</i> thermally treated samples in N ₂ and in air.	61
Figure 35. XRD patterns of Pol-N ₂ sample and Y ₂ Si ₂ O ₇ in orthorhombic system.	62
Figure 36. XRD patterns of Pol-Thermally oxidized sample and Y ₂ Si ₂ O ₇ in triclinic system.	63
Figure 37. Phase identification in all β-Si ₃ N ₄ samples in XRD patterns.	63
Figure 38. Electron photomicrographs of surface preparations: a) Pol-Untreated and b) Pol-HF.	64
Figure 39. SEM magnification on: a) Pol-Untreated and b) Pol-HF surface.	64
Figure 40 a. Result of EDX performed on Pol-Untreated.	65
Figure 40 b. Result of EDX performed on Pol-HF.	65
Figure 41 c. Electron photomicrograph of Pol-N ₂ surface preparation.	65
Figure 41 d. Electron photomicrograph of Pol-Thermally oxidized surface preparation.	66
Figure 42. Results of EDX performed on Pol-N ₂ .	66

Figure 43. Result of EDX performed on Pol-Thermally oxidized.	67
Figure 44. Raman spectrum in the wavenumber region 142-764 cm^{-1} of Pol-Thermally oxidized sample. It is still possible to see the three intense bands (E_{2g} , A_g , E_{1g}), the signal of He-Ne lamp, and three typical bands of the material highlighted by red rectangles.	67
Figure 45. $\alpha\text{-Y}_2\text{Si}_2\text{O}_7$.	68
Figure 46. Surface representation of: a) Pol- N_2 and b) Pol-Thermally oxidized.	68
Figure 47. Averaged Raman spectra of red complex's components.	69
Figure 48. a) Average spectra of <i>P. gingivalis</i> and b) typical spectrum of macromolecules found in cells.	70
Figure 49. Main peaks identification in <i>P. gingivalis</i> spectrum.	70
Figure 50. Raman spectra comparison between <i>P. gingivalis</i> and Untreated samples.	74
Figure 51. Overlapping of Raman spectra of <i>P. gingivalis</i> , <i>as fired</i> and <i>polished</i> Untreated samples.	75
Figure 52. Raman spectra comparison between <i>T. denticola</i> and Untreated samples.	78
Figure 53. Overlapping of Raman spectra of <i>T. denticola</i> , <i>as fired</i> and <i>polished</i> Untreated samples.	78
Figure 54. Raman spectra comparison between <i>T. forsythia</i> and Untreated samples.	80
Figure 55. Overlapping of Raman spectra of <i>T. forsythia</i> , <i>as fired</i> and <i>polished</i> Untreated samples.	81
Figure 56. Raman spectra overlapping and comparison between <i>P. gingivalis</i> and HF, N_2 and Thermally oxidized samples.	83
Figure 57. Raman spectra overlapping and comparison between <i>T. denticola</i> and HF, N_2 and Thermally oxidized samples.	85
Figure 58. Raman spectra overlapping and comparison between <i>T. forsythia</i> and HF, N_2 and Thermally oxidized samples.	87
Figure 59. Fluorescence microscopic visualization of adherent bacteria on: a) Pol-Untreated and b) Pol-Thermally oxidized.	89
Figure 60. Evolution of pH on Pol-Untreated surface.	90
Figure 61. pH microscopy performed on: a) Pol-Untreated and b) Pol-Thermally oxidized sample.	91
Figure 62. Explanation of the succession of events during the pH experiments on Pol-Untreated Si_3N_4 surface.	91
Figure 63. Schematic description of degradative events on Si_3N_4 surface.	95

LIST OF TABLES

Table 1. Properties of Si ₃ N ₄ ceramics.	15
Table 2. Physical values of materials.	16
Table 3: Composition of BHI (25 g in 1 liter distilled water).	45
Table 4: Composition of FBS.	46
Table 5: Composition of CDC anaerobe 5% sheep blood agar (quantity in 1 liter purified water).	47
Table 6: Composition of Bacto™ Brain Heart Infusion (in 1 liter purified water).	47
Table 7. Peaks position of triplet in <i>as fired</i> samples.	55
Table 8. Peaks position of triplet in Untreated and HF <i>polished</i> samples.	57
Table 9. Peaks position of double triplet in N ₂ <i>polished</i> sample.	57
Table 10. Peaks position in Thermally oxidized <i>polished</i> sample.	58
Table 11. Peaks assignment for bacterial Raman spectra.	71

ABBREVIATIONS

Common abbreviations used in this thesis are listed in alphabetical order.

A	Adenine
AF	As fired
Al ₂ O ₃	Alumina (aluminium oxide)
ATCC	American Type Culture Collection
BHI	Broth-enriched heart infusion
BspA	Bacteroides surface protein
C	Cytosine
CCD	Charge-coupled device
CFDA	5-(and 6)-carboxyfluorescein diacetate
CFU	Colony forming unit
CLSM (o LSCM)	3D Laser-scanning confocal microscope
CM	Cytoplasmic membrane
CVD	Chemical vapor deposition
D-PS	D-phosphate buffer saline
EDX	Energy dispersive X-ray
FBS	Foetal Bovine Serum
G	Guanine
He-Ne	Helium-neon
HF	Hydrofluoric acid
HIP	Hot isostatic pressing
IM	Inner membrane
LPS	Lipopolysaccharides
LTA	Lipoteichoic acids

OM	Outer membrane
PD	Periodontal diseases
PDF	Powder diffraction file
Phe	Phenilalanine
PI	Propidium iodide
P. gingivalis	Porphyromonas gingivalis
Pol	Polished
PP	Periplasm
SCHEM	Scanning chemical microscope
SEM	Scanning electron microscope
Si ₃ N ₄	Silicon nitride
SiAlON	Silicon aluminium oxy-nitride
S-layer or SL	Surface layer
T	Thymine
T. forsythia	Tannerella forsythia
T. denticola	Treponema denticola
XRD	X-ray diffraction
Y ₂ Si ₂ O ₇	yttrium silicate

ABSTRACT

Periodontal diseases are multifactorial infections elicited by a complex of bacterial species that interact with host tissues and cells. One of the most important and studied cluster is the “*red complex*”, which consisted of three specific Gram-negative bacterial species: *Porphyromonas gingivalis*, *Treponema denticola* and *Tannerella forsythia*.

The present study focuses on the spectroscopic, structural (XRD) and morphological (SEM) characterization of different superficial treatments of silicon nitride (Si_3N_4): *Untreated*, *HF etched*, *N₂ bake* and *Thermally oxidized*. In addition, it employs for the first time Raman spectroscopy to investigate and monitor the behavior and biochemical changes of these particular bacterial colonies when in contact with the various analyzed surfaces.

The experimental data obtained by fluorescence and pH microscopy have moreover shown that the lytic activity of bacterial cells is related to a peculiar pH-dependent chemistry developed at the surface of Untreated Si_3N_4 together with the formation of ammonium ions (NH_4^+) in aqueous environment.

The results obtained in this work show that the Si_3N_4 bioceramic surface seems to possess an improved bacteriostatic conduct in dental implants coupled with a unique capacity of downregulation of bacterial metabolisms and a “natural drift” toward a protective chemical action.

Therefore, the extraordinary properties of this material can promote its use in dentistry.

Keywords: Si_3N_4 surface, bacteria, Raman spectroscopy, SEM, XRD, pH microscopy, antibacterial activity.

CHAPTER I: SILICON NITRIDE

1.1 Background

Silicon nitride (Si_3N_4) is a non-oxide ceramic material developed for industrial applications and intensively studied and researched for many years.

The discovery of the existence of Si_3N_4 on Earth dates back to more than 150 years ago [1]. Around 1860 several proposals were promoted on the role of this compound during the formation of the Earth: it was assumed that silicon reacted with nitrogen to form Si_3N_4 , and the reaction of the red-hot Si_3N_4 with water may have been responsible for the formation of ammonia and the introduction of nitrogen into organic compounds and life. Moreover, according to the theory developed in 1939 by the researcher Lord Rayleigh, it has been hypothesized that, during the prehistoric era, when the atmosphere was chemically reducing and rich in ammonia, the prehistoric rocks of Earth's crust contained higher quantities of silicon and other nitrates than the atmosphere [2]. Although Si_3N_4 is rarely observed in nature, the evidence for the natural existence of this material in the galaxy has come from the detailed study of particles of meteoritic rock, with possible origins in ancient supernovae [3, 4]. The mineralogical analyses by scanning and transmission electron microscopy showed that in the residues of three primitive chondrites was possible to find traces of a new mineral, called nierite, which presented structural and spatial characteristics comparable to those of synthetic $\alpha\text{-Si}_3\text{N}_4$.

The first synthetic preparation probably was developed in 1859 by Deville and Wöhler [5], but they termed silicon nitride without specifying its chemical composition. Only in 1879, Schützenberger reported a product with the composition of the tetranitride, but despite the development of different synthesis techniques in the first decade of the '900, this ceramic product remained a chemical curiosity for nearly fifty years. In fact, commercial interest and reports of its usefulness as a refractory material appeared in the early 1950s with the publication by the Carborundum Company (Niagara Falls, New York) of several patents [6] on its manufacture and application. Furthermore, by 1955, Si_3N_4 was an important accepted refractory material, with applications including a bonding phase for silicon carbide (SiC) and oxide refractories, a mold wash resisting attack by molten nonferrous metals, and a thermocouple sheath material able to withstand numerous cycles

at high temperature four times better than an equivalent alumina (Al_2O_3) article. The development of Si_3N_4 ceramics as potential high temperature structural engine materials markedly accelerated in the early 1960s, and an important breakthrough came in 1961 with the realization of a fully dense and much stronger form obtained by hot-pressing Si_3N_4 powder in the presence of small amounts of a metal oxide, such as MgO [7].

In 1971, started in the United States a very large program of development work on this non-oxide ceramic. The Advanced Research Project Agency (ARPA) of the U.S. Department of Defense placed a US \$17 million contract to develop a five year research project with two important industrial giant: the Ford Motor Company (Dearborn, MI) and the Westinghouse Electric Corporation (Pittsburg, PA). The aim was to demonstrate the practicability of stationary and mobile ceramic-containing gas-turbine engines with Si_3N_4 as the major and leading candidate material [8, 9].

In the past fifty years, many different aspects has been explored and has been conducted substantial additional work of study and development on the Si_3N_4 , primarily by the ceramic, electronic and recently in biomedical field. Despite the scientific and industry communities have a lot of information on this ceramic compound, even today there are difficulties in defining Si_3N_4 as a materials class. As a result, Si_3N_4 has been and is still today one of the most extensively studied ceramics in history.

1.2 Fundamental properties

1.2.1 Si_3N_4 production

In the last fifty years, ceramic and mechanical properties of Si_3N_4 have been significantly improved by refining processing methods and using additives to create composite structures [1, 10, 11]. In literature there are three different strategies of production and processing of this material known as reaction bonding, sintering and pressing-assisted sintering, respectively [12-14].

The first technique, the higher-strength reaction-bonded form of single-phase material, seems to have been developed mainly in the 1950s for refractory products from the nitridation of silicon powder, with the intention of producing Si_3N_4 powder. In the reaction, the article is typically heated in N_2 at temperatures between 1200° and 1400°C , where the

Si reacted with N_2 to form Si_3N_4 and bond the particle together. This process was immediately recognized and appreciated because it allowed the production of complex shaped components without the need for time-consuming and expensive finishing operations. The resulting material presented high porous (typically 25-35%), low density and low strength (200-300 MPa).

During the second process, that is the sintering, Si_3N_4 powders mixed with additives (typically Y_2O_3 and Al_2O_3) are, instead, compacted and heated in an N_2 atmosphere of 10-20 MPa pressure at temperatures greater than $1700^\circ C$. The densification process takes place thanks to the presence of additives, which react with the native SiO_2 layer on the Si_3N_4 powder to form a liquid phase that surrounds its particles. On cooling, the liquid phase solidifies to form an amorphous or a partially crystallized glassy phase at the boundaries of the Si_3N_4 grains.

Finally, hot pressing and hot isostatic pressing (HIP) are the common methods of pressure-assisted sintering developed around the late 1960s, and these are used to address inadequate densification of sintered Si_3N_4 . In hot pressing sintering, the powder with the addition of additives is positioned in a graphite die and subjected to a pressure equal to 50 MPa and at a temperature above $1700^\circ C$, while in HIP the sample is encapsulated in a metal cap and cooked at the same temperature but at a pressure of about 150-200 MPa. The Si_3N_4 that is obtained with this procedure gains improvements in strength, although at a higher manufacturing cost. To solve this problem, a compromise was to combine the two techniques to obtain a new method, called sinter-HIP. In the first phase is used sintering method to produce Si_3N_4 with isolated pores, and then, in the second part, is employed the HIP technique without encapsulation in a metal cap in order to achieve a relatively high strength limiting also the production costs.

As a consequence of these three processing, the forms of Si_3N_4 are different not only in density, in pore and grain structure, but also in resulting mechanical, thermal and thermo-mechanical properties.

1.2.2 Crystal structure

Silicon nitride exists in three crystallographic structures designated as α , β and γ phase [1, 15]. It has been generally accepted that the two major common forms are α and β phase

because can be produced under normal pressure condition [16], while γ phase can only be synthesized under high pressures and temperatures [17].

After publication in 1957 of preliminary structural data [18], in the same year Hardie and Jack [19] and in 1958 Ruddlesden and Popper [20] described in a complete and detailed way the α - and β - Si_3N_4 compositions by presenting an “idealized” structural model. In both phases, the basic building unit comprises a silicon-nitrogen tetrahedron in which a silicon

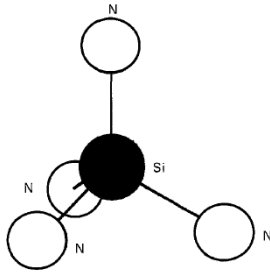


Fig. 1. Tetrahedral unit in Si_3N_4 .

atom lies at the center of the tetrahedron, while the four nitrogen atoms are located at each corner as shown in Fig. 1. The tetrahedral structures SiN_4 are joined by sharing corners in such a way that each nitrogen is common to the other three basic units. Thus, each silicon atom has four nitrogen atoms as nearest neighbours and each nitrogen has three silicon atoms as nearest neighbours.

Detailed X-ray diffractometry (XRD) examination also revealed that α - and β - Si_3N_4 had hexagonal structures [21], with the c -axis dimension of the unit cell of α phase approximately twice that of the β phase.

Several experiments have been performed to determine with certainty all elements of these structures. The α - Si_3N_4 (Fig. 2) has a space group of $P31c$, and the layers of atoms are linked along the $[001]$ direction in the sequence ABCDABCD, where the CD layer is similar to that AB except that it is rotated by 180° on the c -axis. This phase presents an average Si-N bond length equal to 0.1738 nm.

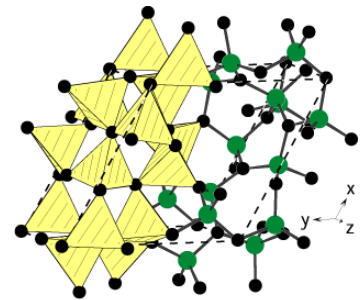


Fig. 2. α - Si_3N_4 . Green balls are Si, black are N.

To β - Si_3N_4 was, instead, assigned the spatial group $P6_3/m$. The structure is composed of puckered rings of alternating Si and N atoms, which can be considered as layers with a stacking sequence ABAB that form long continuous channels in the c direction (Fig. 3). This repeated AB sequence is the same in both phases. Moreover, the average Si-N bond length is 0.173 nm, although there are

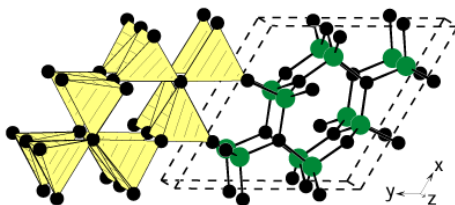


Fig. 3. β - Si_3N_4 . Green balls are Si, black are N.

four distinct values ranging from 0.1704-0.1767 nm. Exists also an important relationship between α - and β - Si_3N_4 , because the two distinctive forms are respectively the low- and high temperature modifications.

This observation arises from the examination that during nitridation of sintering process the proportion of α phase increases with decreasing

temperature, and that above 1400°C the α phase transforms to the β . However, if the previous statement was true, it should be possible to observe the reverse transformation at temperatures below 1400°C, from β -Si₃N₄ to α -Si₃N₄. Instead, this has never been observed experimentally, since calculations show that α phase has a slightly higher free energy than the β phase, a difference equal to 30 KJ mol⁻¹, and most likely is this energy that prevents the inverse transformation [15]. In this way, the β phase is the thermodynamically more stable modification at all temperatures, and for this reason most of the samples produced and used in industrial and biomedical field are precisely in the form of β -Si₃N₄.

Also the present study employed and analyzed β -Si₃N₄ samples.

1.2.3 Material properties

Si₃N₄ belongs to a new generation of ceramics developed in order to be widely used in structural applications at high temperatures. Because of the good combination of its properties, Si₃N₄ is one of the most promising materials in this class. In particular, this compound has high strength at high temperatures, good thermal stress resistance due to the low coefficient of thermal expansion, and relatively good resistance to oxidation compared to other high-temperature structural materials. Moreover, this element has a low density equal to 3.2 g cm⁻³, which corresponds to about 40% of the density of high temperature superalloys, and this feature may offer components of lower weight and therefore is sometimes an important advantage over other high-temperature materials. Additionally, Si₃N₄ does not have a real melting point but decomposes under 0.1 MPa N₂ at 1900°C [22]. The main characteristics of this material are indicated in Table 1.

Table 1. Properties of Si₃N₄ ceramics.

Description	Value	Description	Value
Theoretical density (g cm ⁻³)	3.19-3.202	Thermal conductivity (RT) (Wm ⁻¹ K ⁻¹)	15-50
Coefficient of thermal expansion (20-1500°C) (10 ⁻⁶ °C ⁻¹)	2.9-3.6	Thermal diffusivity (RT) (cm ² sec ⁻¹)	0.08-0.29
Specific heat (J kg ⁻¹ °C ⁻¹)	700	Electrical resistivity (RT) (Ωcm)	~10 ¹³
Fracture toughness (MNm ^{-3/2}):	3.4-8.2	Flexural strength (RT) (MN m ⁻²):	400-950

Like other ceramics, Si₃N₄ is, however, a brittle element. In 2000, Chen and Ardell reviewed the measurement of the fracture toughness of different brittle and semi-brittle products and reported the physical properties of the materials tested [23], confirming the data on Si₃N₄ previously reported in 1987 by Ziegler et al. [22].

Table 2. Physical values of materials.

Material	Vickers hardness, H (GPa)	Young's modulus, E (GPa)	Poisson's ratio, ν	Grain size (μm)
ZnS	1.40 \pm 0.06	74.5	0.280	20-35
GC	6.10 \pm 0.31	120	0.243	1
Si ₃ N ₄	12.55 \pm 0.63	299	0.270	0.59
Ti ₃ Si ₃	11.65 \pm 0.84	156	0.283	5-6
SiC	34.2 \pm 1.28	342.3	0.19	0.047
Ni ₃ Ge	3.2	178	0.35	26

As reported in Table 2, Si₃N₄ has a Vickers hardness of 12-13 GPa, a Young's modulus of 299 GPa, a Poisson's ratio of 0.270, and a typical grain size of 0.59 μm .

In the last two decades, Si₃N₄ was investigated as potential candidate for orthopedic and dental applications in the human body. The key characteristics that makes it so interesting are low friction, fracture toughness, wear resistance, thermal shock resistance and excellent radiographic visibility as a partially-radiolucent material.

Several studies have reported that this non-oxide ceramic does not demonstrate toxic behavior during in vivo tests or inflammatory response while promoting cell culture growth [24-26], but despite all these promising elements, in literature there are some controversy about its biocompatibility and its use as biomaterial in medicine [27-29]. An obstacle may be related to the esthetic appearance, because Si₃N₄ has a light-gray to black color, very differently than the white-colored ceramics (as Al₂O₃ or ZrO₂), which are much more similar to the natural color of bones. Another reason could be tied to the cost of production of this non-oxide material, which is slightly higher than that of the oxide ceramic. Furthermore, all the results that have been obtained to date are only laboratory experimental data and consequently is difficult to have secure evidence of its behavior once in contact with physiological fluids.

1.3 Applications

1.3.1 Industrial applications

In the description of the history of Si_3N_4 was mentioned that the beginning of production and commerce of this ceramic came in the 1950s, but only in the 1960s and 1970s was reached the major driving force for its development as a refractory material.

One of the main applications was and still is in automobile industry, in particular for diesel and spark-ignited engines. In the first is included glowplugs for faster start-up, precombustion chamber for lower emissions, and turbocharger for reduced engine lag and emissions, while in the second Si_3N_4 was used for rocker arm pads for lower wear, turbocharger for lower inertia and less engine lag, and in exhaust gas control valves for increased acceleration. Most of these components are manufactured in United States and Japan, although considerable developed work has also been conducted in Germany and other European Union country [1]. In the United States are used ceramic-engine components to reduce emission, in Japan to improve performance, and, as example of production level, is estimated that annually are manufactured more than 300000 sintered Si_3N_4 turbochargers [30].

Another important field of application of this material are roller and ball bearings. These compounds, which are illustrated in Fig. 4, are harder than metal and this reduces contact with the bearing track. As result, the performances than traditional metal bearings are



Fig. 4. Si_3N_4 bearing parts.

considerably improve: the friction is reduced by up to 80%, the lifetime increases from 3 to 10 times, the speed increases to 80%, the weight of the material decreases to 60%, and is possible to achieve a higher corrosion resistance and higher operation temperature [1, 30]. A prestigious example that can be mentioned is the purpose of these compounds in the main engine of the NASA's Space Shuttle [31].

Finally, further uses which may be quote are cutting tips for high-speed metal cutting, components for handling and die-casting of low-melting and reactive aluminum, and insulator and chemical barrier in manufacturing integrated circuits and microchips.

Before moving to the next description, it is interesting to specify an annotation concerning an "alternative" engineered material to Si_3N_4 .

In the previous description, have been indicated the remarkable engineering properties of this material, but, it was also said that, unfortunately, it does not lend itself to ease of fabrication.

The discovery in 1972 of an isomorphous form of Si_3N_4 called SiAlON made independently in the UK by Jack and Wilson, and in Japan by Osama et al, brought the advantages of a material based upon Si_3N_4 and, in the same time, stimulated enormous interest and triggered off investigations on a worldwide scale.

SiAlON, which is the acronym for Silicon Aluminium Oxy-Nitride, is an isomorphous structure of $\beta\text{-Si}_3\text{N}_4$ by equivalent exchange of Al-O for Si-N, where the charge deficit caused by substituting Al for Si is balanced by substituting of N by O. Moreover, SiAlONs exist in three basic forms, each of which is isostructural with one of the two common forms of Si_3N_4 , alpha (α) and beta (β), and with silicon oxynitride.

The chemical composition of these materials can be written as $\text{Si}_{6-z}\text{Al}_z\text{O}_z\text{N}_{8-z}$, where z represents the number of Al-O pairs substituting for Si-N pairs and its value is between $0 < z \leq 4.2$. The compounds have a $P6_3$ space groups and the hexagonal structures of $\beta\text{-Si}_3\text{N}_4$ are still maintained. Therefore, in these structures, the replaced Al atom is 4-coordinated and the O atom is 3-coordinated, and these changes can obviously lead to a new organization and a different distribution of the atoms in the final composition.

These ceramics are produced by combining a mixture of raw materials including silicon nitride, alumina, aluminium nitride, silica and the oxides of a rare earth element, such as yttrium, which are introduced as additives to improve the sintering process.

They are a specialist class of high-temperature refractory objects, and furthermore, are exceptionally corrosion and wear resistant and exhibit high strength, good thermal shock resistance, low thermal expansion and good oxidative resistance up to above $\sim 1000^\circ\text{C}$.

The relationship between SiAlON and Si_3N_4 is similar to that between brass and pure copper. In the later case, copper atoms are replaced by zinc to give a better and stronger alloy than the mother metal. In the case of SiAlON, there is substitution of Si by Al with corresponding atomic replacement of N by O, to satisfy vacancy requirements. The resulting solution, SiAlON, has intrinsically superior properties to the original pure material Si_3N_4 .

Precisely for this reason, after its discovery, SiAlON has found a prominent place in industrial applications, replacing the use of Si_3N_4 .

1.3.2 Medical applications

Despite the Si_3N_4 has attracted the attention of the scientific community only in the last years, and although there are many doubts and disputes about the use of this material in medicine, it is interesting to describe its different experimental applications in biomedical field.

The first concerns the use of Si_3N_4 in total joint replacements, especially for knee and hip prostheses. Several studies [27, 32, 33] demonstrate that the non-oxide ceramic under some tests conditions and tribological point of view presents a very low wear rate and low friction, as well as an excellent behavior in water as lubricant material [32, 34]. Other research [35], however, has pointed out the fact that this advanced material is not suitable for body prostheses, consequently to the formation of surface SiO_2 , which could chip off, inducing a catastrophic third body wear.

It is also considering the Si_3N_4 as a possible candidate for mini-osteo-fixation systems (plates, screws, etc.), for example in maxillofacial surgery in substitution of metallic implants, and in implantations in otorhinolaryngology and traumatology fields for ossicular chain reconstruction prostheses, disks for reconstruction of anterior or lateral skull base defects, and applications in traumatic damages [36].

Always in surgery, reaction bonded Si_3N_4 resulted a successful implant material for spinal fusion and intervertebral spacers in terms of resistance to slippage, implant/bone fusion, resistance to subsidence, potential for reaction and decrease of pain [29, 37]. The various medical uses of Si_3N_4 are depicted in Fig. 5.



Fig.5. Si_3N_4 medical devices.

Because it thinks that Si_3N_4 is capable of create interfaces compatible either with fabrication processing and biological systems, it was used for the development of multiwell drug-release devices [38], micro electromechanical systems (Bio-MEMS) [39], 3-d

microelectrode arrays (MEA) [40], micro-machined neural probes, drug delivery micropumps and micro fabricated immunoisolation biocapsules [41].

Finally, in 2012, begins the study on the possible antibacterial activity of Si_3N_4 compared to polyetheretherketone (PEEK) and titanium to understand their respective susceptibility to bacterial infection [42].

The present study is focused not only on the examination and on characterization of different $\beta\text{-Si}_3\text{N}_4$ surfaces, but is also conducted to investigate their presumed antibacterial activity with the aim of bringing new results and information, which can lead to the use of such material also in dentistry field.

CHAPTER II: BACTERIAL INTRODUCTION

2.1 Description of periodontal diseases

The human oral cavity is a complex ecosystem that contains a large number of bacterial colonizers that thrive in a dynamic environment.

Since health is the most common state of a host, it has been speculated that the autochthonous flora and the host have co-evolved and interact in a balanced fashion that is beneficial to both of them. Such situation, however, is not well defined in the oral cavity because colonizing organisms have the potential to impact and modify the normal physiological status of the epithelium and its development. Since interactions of host and microbial cells are inherently unstable, disease may arise due to a perturbation occurring between host and bacteria [43].

Periodontal diseases (PD) are the most commonly known chronic inflammatory disorders in human mouth, which are caused by a pathogenic microbiota in the subgingival biofilm through specific adherence interactions and accumulation of virulence factors.

The inflammation is provoked and maintained by the dental plaque accumulated on the tooth surface, called bacterial biofilm, and in the gingival pocket, specified as subgingival plaque (Fig. 6).



Fig. 6. Comparison between oral healthy and periodontal disease.

These pathological conditions have been recognized since more than five millennia as shown in writings found in ancient Egyptian and Chinese manuscripts, but the first modern writings were by Abu I Quasim, also known as Abuccis of Cordova (Spain), only in the 10th century.

More recently, knowledge and descriptions of treatment of periodontal disease were made by Pierre Fauchard, who wrote the first dental textbook “*The Surgeon Dentist*” in 1728, and John Hunter, who composed “*The Natural History of the Human Teeth*” in 1771 and “*A Practical Treatise on the Diseases of the Teeth*” in 1778.

Although there was already a considerable body of writings on dentistry, the discovery of the idea that bacteria contribute to oral disease is attributed to Antoni Von Leeuwenhoek. He was a 17th century scientist and correspondent of the Royal Society of London and the first who observed and described these microorganisms like “animacules” around the teeth and related them by inference to disease [44, 45].

Usually these multifactorial infectious are divided into two different types, gingivitis and periodontitis (Fig. 7). Gingivitis is an inflammatory lesion of soft marginal gingiva without loss of periodontal supporting tissues; periodontitis, instead, is defined as an inflammation in gingival tissues with loss or destruction of periodontal attachment including the periodontal ligament and alveolar bone.



Fig. 7. Difference between the two types of inflammatory disorders.

In 1999, the World Workshop for the Classification of Periodontal Diseases and Conditions defined the eight categories of periodontal illnesses depending on the clinical manifestation of gingivitis and periodontitis [44, 46].

In the same year, these classes were also included in the American Academy of Periodontology Classification (Fig. 8) becoming a complete and detailed encyclopedic description, which allows effective communication between health care professionals using a common language [44].

- (a)
- | | |
|--|---|
| <p>I. Gingival Diseases</p> <p>A. Dental plaque-induced gingival diseases*</p> <ol style="list-style-type: none"> 1. Gingivitis associated with dental plaque only <ol style="list-style-type: none"> a. without other local contributing factors b. with local contributing factors (See VIII A) 2. Gingival diseases modified by systemic factors <ol style="list-style-type: none"> a. associated with the endocrine system <ol style="list-style-type: none"> 1) puberty-associated gingivitis 2) menstrual cycle-associated gingivitis 3) pregnancy-associated <ol style="list-style-type: none"> a) gingivitis b) pyogenic granuloma 4) diabetes mellitus-associated gingivitis b. associated with blood dyscrasias <ol style="list-style-type: none"> 1) leukemia-associated gingivitis 2) other 3. Gingival diseases modified by medications <ol style="list-style-type: none"> a. drug-influenced gingival diseases <ol style="list-style-type: none"> 1) drug-influenced gingival enlargements 2) drug-influenced gingivitis <ol style="list-style-type: none"> a) oral contraceptive-associated gingivitis b) other 4. Gingival diseases modified by malnutrition <ol style="list-style-type: none"> a. ascorbic acid-deficiency gingivitis b. other <p>B. Non-plaque-induced gingival lesions</p> <ol style="list-style-type: none"> 1. Gingival diseases of specific bacterial origin <ol style="list-style-type: none"> a. <i>Neisseria gonorrhoea</i>-associated lesions b. <i>Treponema pallidum</i>-associated lesions c. streptococcal species-associated lesions d. other 2. Gingival diseases of viral origin <ol style="list-style-type: none"> a. herpesvirus infections <ol style="list-style-type: none"> 1) primary herpetic gingivostomatitis 2) recurrent oral herpes 3) varicella-zoster infections b. other | <ol style="list-style-type: none"> 3. Gingival diseases of fungal origin <ol style="list-style-type: none"> a. <i>Candida</i>-species infections <ol style="list-style-type: none"> 1) generalized gingival candidosis b. linear gingival erythema c. histoplasmosis d. other 4. Gingival lesions of genetic origin <ol style="list-style-type: none"> a. hereditary gingival fibromatosis b. other 5. Gingival manifestations of systemic conditions <ol style="list-style-type: none"> a. mucocutaneous disorders <ol style="list-style-type: none"> 1) lichen planus 2) pemphigoid 3) pemphigus vulgaris 4) erythema multiforme 5) lupus erythematosus 6) drug-induced 7) other b. allergic reactions <ol style="list-style-type: none"> 1) dental restorative materials <ol style="list-style-type: none"> a) mercury b) nickel c) acrylic d) other 2) reactions attributable to <ol style="list-style-type: none"> a) toothpastes/dentifrices b) mouthrinses/mouthwashes c) chewing gum additives d) foods and additives 3) other 6. Traumatic lesions (factitious, iatrogenic, accidental) <ol style="list-style-type: none"> a. chemical injury b. physical injury c. thermal injury 7. Foreign body reactions 8. Not otherwise specified (NOS) |
|--|---|

- (b)
- | | |
|--|---|
| <p>II. Chronic Periodontitis[†]</p> <ol style="list-style-type: none"> A. Localized B. Generalized <p>III. Aggressive Periodontitis[†]</p> <ol style="list-style-type: none"> A. Localized B. Generalized <p>IV. Periodontitis as a Manifestation of Systemic Diseases</p> <ol style="list-style-type: none"> A. Associated with hematological disorders <ol style="list-style-type: none"> 1. Acquired neutropenia 2. Leukemias 3. Other B. Associated with genetic disorders <ol style="list-style-type: none"> 1. Familial and cyclic neutropenia 2. Down syndrome 3. Leukocyte adhesion deficiency syndromes 4. Papillon-Lefèvre syndrome 5. Chediak-Higashi syndrome 6. Histiocytosis syndromes 7. Glycogen storage disease 8. Infantile genetic agranulocytosis 9. Cohen syndrome 10. Ehlers-Danlos syndrome (Types IV and VIII) <ol style="list-style-type: none"> 11. Hypophosphatasia 12. Other C. Not otherwise specified (NOS) <p>V. Necrotizing Periodontal Diseases</p> <ol style="list-style-type: none"> A. Necrotizing ulcerative gingivitis (NUG) B. Necrotizing ulcerative periodontitis (NUP) <p>VI. Abscesses of the Periodontium</p> <ol style="list-style-type: none"> A. Gingival abscess B. Periodontal abscess C. Pericoronal abscess | <p>VII. Periodontitis Associated With Endodontic Lesions</p> <ol style="list-style-type: none"> A. Combined periodontic-endodontic lesions <p>VIII. Developmental or Acquired Deformities and Conditions</p> <ol style="list-style-type: none"> A. Localized tooth-related factors that modify or predispose to plaque-induced gingival diseases/periodontitis <ol style="list-style-type: none"> 1. Tooth anatomic factors 2. Dental restorations/appliances 3. Root fractures 4. Cervical root resorption and cemental tears B. Mucogingival deformities and conditions around teeth <ol style="list-style-type: none"> 1. Gingival/soft tissue recession <ol style="list-style-type: none"> a. facial or lingual surfaces b. interproximal (papillary) 2. Lack of keratinized gingiva 3. Decreased vestibular depth 4. Aberrant frenum/muscle position 5. Gingival excess <ol style="list-style-type: none"> a. pseudopocket b. inconsistent gingival margin c. excessive gingival display d. gingival enlargement (See I.A.3. and I.B.4.) 6. Abnormal color C. Mucogingival deformities and conditions on edentulous ridges <ol style="list-style-type: none"> 1. Vertical and/or horizontal ridge deficiency 2. Lack of gingiva/keratinized tissue 3. Gingival/soft tissue enlargement 4. Aberrant frenum/muscle position 5. Decreased vestibular depth 6. Abnormal color D. Occlusal trauma <ol style="list-style-type: none"> 1. Primary occlusal trauma 2. Secondary occlusal trauma |
|--|---|

Fig. 8. The American Academy of Periodontology Classification of a) gingivitis and b) periodontitis.

Unfortunately, these disorders are a very prevalent condition and there is not a globally accepted method for their measurement yet. According to World Health Organization (WHO), they are one of worst dental diseases that affects the world.

Several research have reported that in the United States these illnesses are an important public health problems, and the annual cost of periodontal therapy exceeds \$14 billion. Moreover, recent studies completed by the Center for Disease and Prevention has found that approximately more than a half the American population aged 18 years have PD in its early stages, increasing to up to 75% after 35 years of age. Its mild and moderate forms are present in the 30% to the 50% of the adult population, and the severe generalized form in 5% to 15% [47, 48]. Furthermore, this pathological condition has a higher prevalence in men than in women, and highest in the Latin population of South America (Mexican, Brazilian, Columbians and Chilean people) [49].

In the last 40 years in developed European countries some conflicting evidence and data have been collected on the performance of inflammatory conditions [50].

In 1981, Anderson reported a decline in gingivitis and improvement in dental cleanliness in English children aged 12 years between 1963 and 1978, while Cutress in 1986 observed in New Zealand a reduction in prevalence of gingivitis between 1976 and 1982 in the 15- to 19-year-old adolescents from a 98% to a 79% of subjects.

By contrast, Curilovic et al. in 1977 found that in Zurich between 1957 and 1975 the prevalence of PD in 7- to 17- year-old children was unchanged and its severity had increased. Moreover, between 1983 and 1993 gingival health and dental cleanliness in 5- to 15- year-old children in the United Kingdom deteriorated and this inflammatory conditions increased from 19% to 53% in 1983 and from 26% to 63% in 1993 [50].

Most of data that have been presented consider only gingivitis because firstly it is difficult to demonstrate improvements in periodontitis in children and adolescents, and in second instance is unusual to find significant amounts of periodontal destruction in these age groups.

As PD are multifactorial, it is important to understand their etiological factors and pathogenesis for recognize and understand all the associated risk factors [50-52].

In Fig. 9 is reported a model that contains three layers of elements that can influence periodontal health.

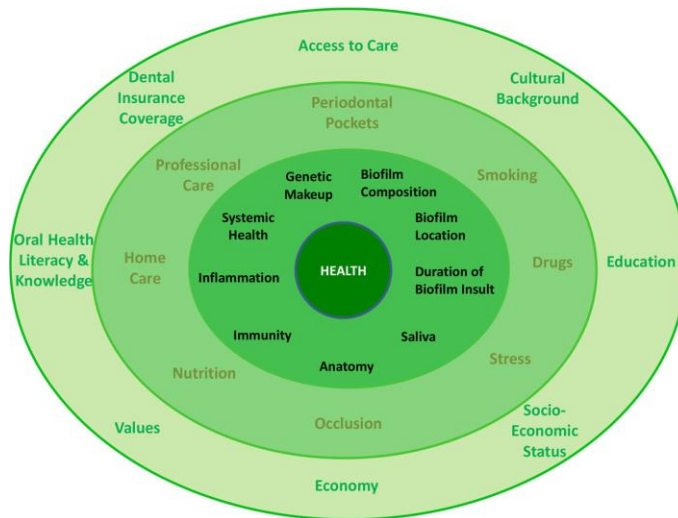


Fig. 9. Three-layer periodontal health model. Inner layer: direct contributing factors; middle layer: oral environment and systemic factors; outer layer: personal factors.

These layers are:

- a) Biologically entities in the inner layer that have a direct effect on the periodontium. These elements also represent non-modifiable risk factors and include biofilm composition, biofilm location, duration of biofilm insult, saliva, anatomy, inflammation, system health and genetic makeup.
- b) Environmental and systemic factors that can influence biological components and are positioned in the middle layer. They are connected to modifiable risk elements and consist of periodontal pockets, smoking, drugs, stress, occlusion, nutrition, home care and periodontal care.
- c) General and personal conditions, which can influence both the previously factors and is located to the outer layer. This level gather together access to care, cultural background, education, socio-economic status, economy, values, oral health literacy and knowledge and dental insurance coverage.

So, it is important not only reduce the possible risk factors that may cause the occurrence of periodontal infections, but also to recognize the symptoms and treat them promptly because these disorders may have a possible role for other systemic illnesses (e.g. coronary heart disease) [50].

2.2 Oral bacteria

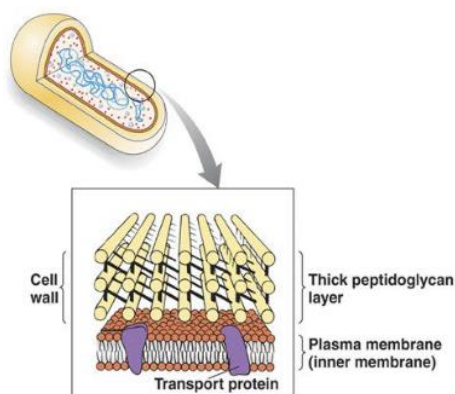
An important concept is the tight relationship between the imbalance caused by microorganisms and periodontal diseases.

The trigger for the initiation of disorders is the presence of bacterial complexes that colonize the sulcular regions between the tooth surface and the gingival margin.

2.2.1 Gram-positive and Gram-negative bacteria

Over the last few decades, several research groups have carefully examined the microbial ecology at sites of periodontal health, gingivitis, and periodontitis. They estimated that nearly 700 bacterial taxa and phylotypes can colonize the human oral cavity, but remains unclear how this myriad of bacteria coexist, compete, or synergize to initiate the disease processes [53-56]. However, it is known that there is a distinctive bacterial flora important for the maintenance of oral health, composed mainly by Gram-positive bacteria, that is different from that involved in oral diseases, consisting of Gram-negative microbes [56]. The primary difference between Gram-positive and Gram-negative bacterial species is the cell envelope, which has the role to protect the cytoplasm and is the first and major line of defense against threats from the environment. It represents a dynamic structure that defines the shape of the bacterium and preserves its cell osmotic integrity. This structure also plays a variety of adaptive roles: provides a sensory interface and molecular sieve, controls both information flow and the transport of solutes, and is the target for numerous antibiotics. Effectively, the monitoring and maintenance of cell envelope integrity is crucial for cell survival [57, 58].

The Gram-positive cell envelope shown in Fig. 10 a) differs in several key ways from its Gram-negative counterpart shown instead in Fig. 10 b). First and foremost, the outer



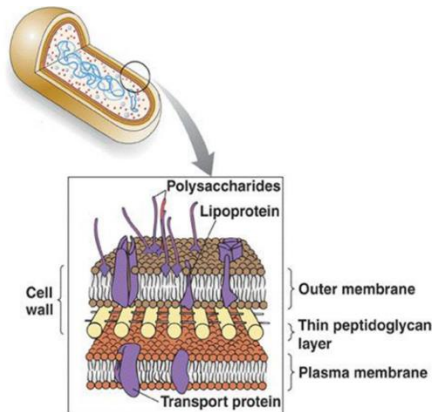
(a) Gram-positive cell wall

Fig. 10 a. Gram-positive cell envelope.

membrane is absent and the cell envelope consists only of two functional layers that enclose the cellular contents surrounded by a thick cell wall, called peptidoglycan. The Gram-positive peptidoglycan is a three-dimensional multi-layered net-like structure consisting of sugar polymers covalently connected via oligopeptides (Fig. 10 a)). This element contains many meshes and it can reach about 30-100 nm thickness, that can withstand high turgor pressures

(up to 20 atm) exerted on the plasma membrane. Collectively, these polymers can account for over 60% of cell wall's mass of these microorganisms making them major contributors to envelope structure and function.

On the contrary, the cell walls of Gram-negative bacteria are more chemically complex,



(b) Gram-negative cell wall

Fig. 10 b. Gram-negative cell envelope.

thinner and less compact compared to those described above. The envelope consists of three principal layers: the outer membrane (OM), the peptidoglycan cell wall, and the cytoplasmic (CM) or inner membrane (IM).

The two concentric membrane layers delimit an aqueous cellular compartment that Peter Mitchell in 1961 first called the periplasm (PP), which controls molecular traffic entering and leaving the cell [57].

Starting from the inside and proceeding outward, the

first layer encountered is the IM (Fig. 10 b)). Like other biological membranes, the IM (or CM) is composed of a phospholipid bilayer and contains the receptors that sense the environment and control the transport systems of nutrients and waste products. Moreover, includes many of the membrane proteins that function in energy production, lipid biosynthesis, secretion and transport of proteins especially toward the OM.

The chemical composition of peptidoglycan layer in Gram-negative bacteria is similar to that in Gram-positive, but its structure is very different. Firstly, it is not the outermost layer, but lies between the IM and the OM. Secondly, since the OM indirectly helps to stabilize the IM, the peptidoglycan mesh surrounding bacterial cells is only a few nanometers thick and makes up only 5-20% of the cell wall.

Finally, the outermost mesh of Gram-negative cell envelope is the OM. This particular structure is a distinguishing feature, because Gram-positive microorganisms lack this organelle. It plays a major role in protecting this class of organisms from the external agents by excluding toxic molecules and providing an additional stabilizing layer around the cell. As shown in Fig. 11, the OM is an asymmetrical membrane, which holds phospholipids and lipopolysaccharides

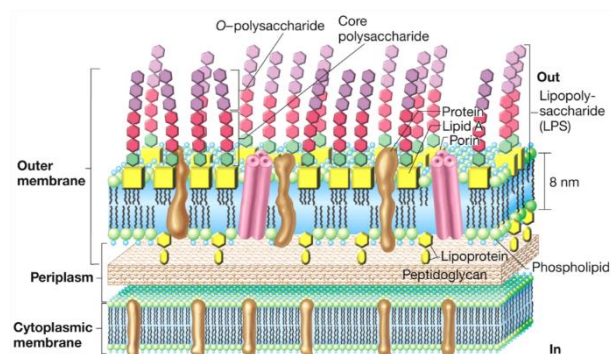


Fig. 11. Detailed representation of OM.

(LPS) in its inner and outer leaflet, respectively. LPS plays a critical part in the barrier function of the OM and is a harmful substance classified as an endotoxin, because it induces a strong response from the normal animal immune system. It also increases the negative charge of the cell membrane and helps stabilize the overall membrane structure. LPS is composed of three parts (Fig. 12): the lipid A, the core and the O-antigen [57, 59, 60].

The first is a phosphorylated glucosamine disaccharide decorated with multiple hydrophobic fatty acids that anchor all the components of LPS into the bacterial membrane. Its moiety is rather well conserved among Gram-negative bacteria, and its domain is responsible for much of the toxicity of this taxa. When the immune system lyses bacterial cells, fragments of membrane containing lipid A are released into the circulation and cause fever, diarrhea, and possible fatal endotoxic shock (also called septic shock).

The core polysaccharide is much more variable between bacteria species and the domain always contains an oligosaccharide component that attaches directly to lipid A.

Lastly, the repetitive extended polysaccharide chain, called the O-antigen or O side-chain, is the most variable part of LPS and shows even a high degree of variability between different strains of the same species. The O antigen, if present, is attached to the core oligosaccharide, and comprises the outermost domain of the LPS molecule. The presence or absence of O chains determines whether the LPS is considered rough or smooth and it was noticed that bacteria with rough LPS usually have more penetrable cell membranes to hydrophobic antibiotics than those with smooth LPS.

It is essential to describe and understand the organization and the cellular structure of Gram-negative bacteria, which are responsible for the PD, in order to better comprehend and interpret the data presented in this study.

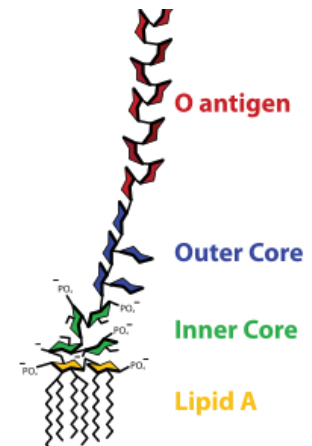


Fig. 12. Components of LPS.

2.2.2 The “red complex”

Several works support the notion that a single bacterial species cannot cause the onset and progression of PD, but there must be the formation of microbial groups or complexes in subgingival pockets responsible for the beginning of the inflammatory and destructive processes. These studies have demonstrated that the transition from a healthy oral

environment to periodontitis, as shown in Fig. 13, is triggered by a specific “set” of microorganisms [56, 61-64].

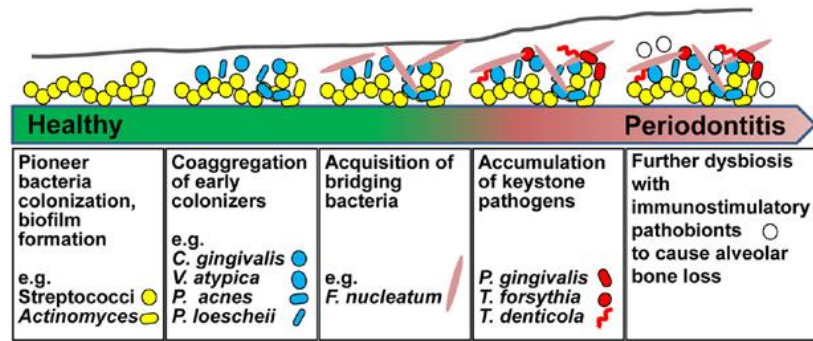


Fig. 13. Dysbiosis during periodontitis development.

Since the oral cavity contains hundreds of bacteria, they were cataloged into six groups to simplify their study and interaction.

The yellow cluster consists of species of Streptococcus, including Streptococcus sanguis and Streptococcus oralis, while the purple cluster is composed of Actinomyces odontolyticus and Veillonella parvula. These bacteria are the pioneer colonizers on the surface of host epithelium and tooth and are responsible for the formation of biofilms.

The Capnocytophaga spp, Campylobacter concisus and Eikenella corrodens form the green complex, whereas the Actinomyces species form the blue one. This group of bacteria exists in the biofilm milieu, but less cognitively associated with other individual bacterial species.

The orange cluster consisted of Fusobacterium spp., Prevotella spp., Micromonas micros (Peptostreptococcus micros), Campylobacter spp., Eubacterium spp. and Streptococcus constellatus. These species act as scaffold to “bridge” multiple bacteria and to facilitate colonization by additional biofilm-forming community members thanks to both their physiological capabilities to use and release nutrient substances in the biofilms, and the recognition that they can bind to the early colonizers and to members of the red complex. Finally, the red complex includes three specific Gram-negative bacterial species that are the main subject of investigation of this study: *Porphyromonas gingivalis* (*P. gingivalis*), *Treponema denticola* (*T. denticola*), and *Tannerella forsythia* (*T. forsythia*). This cluster is considered the most significant complex in PD progression, because the members intensify in number and prevalence with increasing clinical parameters of disorders [56, 64].

- *Porphyromonas gingivalis*

This bacterium belongs to the phylum Bacteroidetes. It is a non-motile, rod-shaped (Fig.

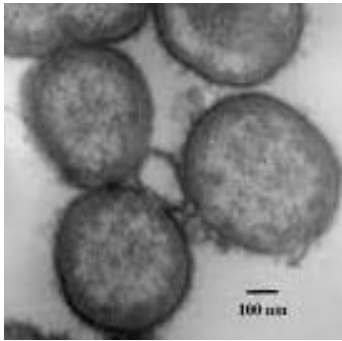


Fig. 14. Transmission electron microscopy of *P. gingivalis*.

14), saccharolytic and strict anaerobic pathogenic species. The bacterial cell may present variable dimensions between 0.4 and 0.8 μm in width and between 1 and 3 μm in length, and when it grows on blood agar containing media, produces black-pigmented colonies.

The frequency of *P. gingivalis* in periodontitis is estimated within the range of 60 to 100%, while it is found in 11 to 25% of healthy subjects. Among the three species that constitute the red complex, *P. gingivalis* is in fact considered the major pathogen, and during the development of diseases it is normally found in micro-colonies in the top layer of subgingival plaque. This well-adapted opportunistic pathogen of the oral mucosa may be also an important mediator in the development of a number of multifactorial and seemingly unrelated chronic disorders, such as rheumatoid arthritis and orodigestive cancers [56, 65-67].

- *Treponema denticola*

This microorganism is a member of the Spirochetes's order and van Leeuwenhoek discovered it more than 350 years ago. It is motile, slender, saccharolytic, obligatory anaerobic and highly proteolytic bacterium. This class presents helical morphology with cell dimensions between 0.1 and 0.2 μm in width and 5 and 15 μm in length (Fig. 15). Spirochaetes form a single cluster because they have developed a range of unique characteristics, including virulence determinants, metabolic pathways, solute transport systems, and surface-binding proteins. It is believed that all treponemes descend from a common spirochetal ancestor and have undergone extensive horizontal gene transfer with Archae and possibly with eukaryotic organisms.

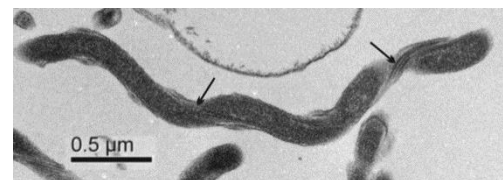


Fig. 15. Transmission electron microscopy of *T. denticola*.

T. denticola is a very strange microorganism because it is evolutionarily quite distinct from both Gram-positive and Gram-negative eubacteria, but in the same time it has

characteristics of both species: it is chemically similar to the first class for the lipoteichoic acids (LTA), but similar to the second for the function of LPS.

During periods of oral health, the number and distribution of these types of bacteria are low or nearly undetectable. However, with the emergence of PD there is a large and rapid increase of bacterial cells and is estimated that *T. denticola* accounts for approximately 50% of the total bacteria present in a periodontal lesion. Moreover, it tends to inhabit the deeper periodontal pockets and is possible to locate it on the surface of dense subgingival bacterial biofilm.

Only in recent years with the development of continuous culture it has been possible to obtain more information on *T. denticola* thanks to transcriptomic and proteomic bacterial analyses, because it was very difficult to grow these bacterial cells on the surface of agar plates using standard methods [56, 68-70].

- *Tannerella forsythia*

The bacterium is a non motile, saccharolytic and strictly anaerobic species of the Cytophaga-Bacteroidetes family. It was initially a taxonomic enigma because it did not look like described species of oral or enteric Gram-negative anaerobic rods, particularly in its cell morphology and slow and fastidious growth requirement.

Originally isolated in the 1970s from dental plaque collected from subjects diagnosed with advanced periodontitis, this bacteria was described for the first time in 1986 by Dr. Tanner et al. of Forsyth Dental Center (Boston). The microorganism was initially placed into the *Bacteroides* genus and named as *Bacteroides forsythus*, but subsequent, phylogenetic analyses based on DNA fingerprinting allowed a reclassification by Sakamoto et al. as lacking a similarity to the genus *Bacteroides* or any of the known genus at the time. Thus, in 2002, a new genus *Tannerella* was formed and the bacteria named *Tannerella forsythia* in honor of its discoverer and the place of discovery.

Typically, the cells appear to be long filaments or medium rods with fusiform or rounded

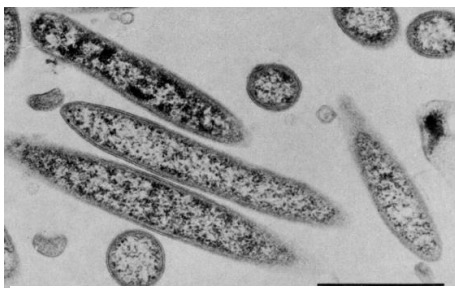


Fig. 16. Transmission electron microscopy of *T. forsythia*. Bar = 1 μm .

ends (Fig. 16) and they are approximately $3.5 \pm 1 \mu\text{m}$ in length and $0.6 \pm 1 \mu\text{m}$ in diameter. These microorganisms possess a typical Gram-negative cell envelope profile consisting of a CM, a PP, and an OM. Additionally, the surface of the OM is completely covered with a regularly 2D crystalline surface layer (S-layer, SL) with a thickness about of

22 nm. The cell surface architecture of *T. forsythia* is so far unique in comparison with other S-layer-carrying bacteria: it is the only known Gram-negative species that is covered with a glycosylated SL, with, again uniquely, two SL glycoproteins simultaneously present, as shown in Fig. 17. The exact role of this monolayer is not yet known, but there are indications that it might be an important virulence factor, mediates adhesion and/or invasion to human gingival epithelial cells and also plays an important part in the initial stage of oral infection.

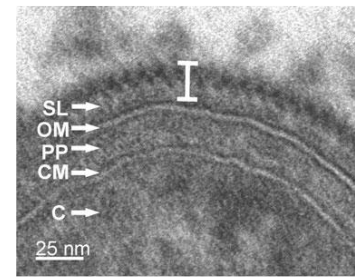


Fig. 17. Ultra-thin cross section of whole cell from *T. forsythia*.

In closing, in presence of active PD *T. forsythia* is located in the intermediate layer of subgingival plaque and is frequently isolated along with *P. gingivalis*. In spite of the overwhelming evidence implicating *T. forsythia* in PD, this bacterium remains an understudied organism. This is partly due to the fastidious growth requirement for its cells culturing, as well as the fact that its genetic manipulations are difficult to perform. Moreover, there are no gene complementation systems currently available for this particular microorganism. [56, 71-74].

An interesting element of red complex is that its members, *P. gingivalis*, *T. denticola* and *T. forsythia*, are normally found together in subgingival plaque because the microbial interaction is more relevant for disease progression than individual species.

There are, however, conflicting studies especially on the synergy of bacteria.

As shown in Fig. 18, Dashper et al. (2011) report that *P. gingivalis* is rarely detected without the presence of *T. denticola* or *T. forsythia*, and they suppose that *T. forsythia* could be more prevalent than *P. gingivalis* in periodontal plaque and may colonize it before the other two complex's members [75-77].

Moreover, from the graphic it is possible to assume that the synergy between *P. gingivalis* and *T. denticola* is almost absent, while it is enough pronounced between *P. gingivalis* and *T. forsythia* and more between *T. denticola* and *T. forsythia*.

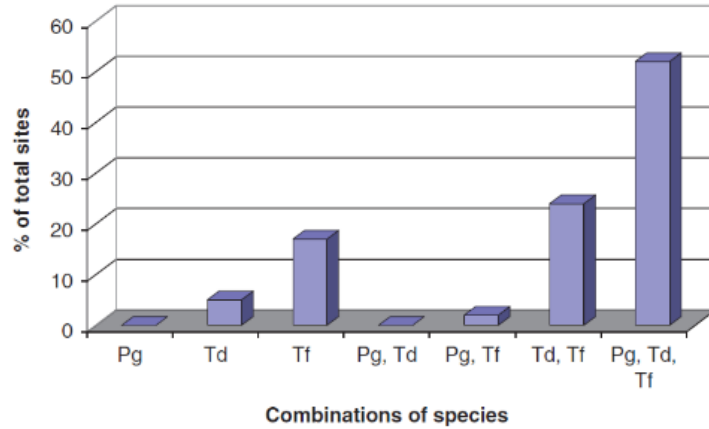


Fig. 18. Combination of *P. gingivalis*, *T. denticola* and *T. forsythia* found in subgingival plaque that had quantifiable by real-time PCR in 41 sites of 37 individuals previously diagnosed with periodontitis.

These data are in contradiction with the results of Suzuki et al (2013) and Tan et al. (2014), which demonstrate that there is a synergistic pathogenesis between *P. gingivalis* and *T. denticola*. These two bacteria display in vitro a symbiotic relationship for the utilization of nutrients, the promotion of growth and the production of biofilm. Therefore, this suggest that there is an intimate rapport between these two species that has evolved to enhance their survival and virulence, although the physiochemical interactions that result in the observed symbiotic and synergistic effects during their co-culture remain largely unknown [61, 77]. Furthermore, Zhu et al. (2013) affirm that *T. forsythia* may not co-localize spatially with the other two species, and not display synergy in biofilm formation as *P. ginigvalis* and *T. denticola* [78].

CHAPTER III: EXPERIMENTAL TECHNIQUES

3.1 Molecular characterization

3.1.1 Raman Spectroscopy

The main spectroscopic techniques used to detect vibrations in molecules are based on the processes of Infrared adsorption and Raman scattering. They are widely employed to provide information on chemical structures and physical forms and to identify substances and molecules from their characteristic spectral pattern, called “fingerprinting”. Moreover, it is used to define quantitatively or semi-quantitatively the amount of a substance in a sample and to measuring particle size and size distribution down to size less than 1 μm .

Historically, the phenomenon of inelastic scattering of light was first predicted by Adolf Smekal in 1923 [79] but first observed experimentally in 1928 by the Indian scientist Sir C. V. Raman together with K. S. Krishnan [80]. In the year following its discovery, Raman scattering was described both in terms of *classical* theory and *quantum* theory.

The older classical theory is based on the wave theory of light and is deficient in that it does not take into account the quantized nature of vibration. In addition, it is not able to explain as much about the relationship between molecular properties and Raman scattering as quantum theory. For this reason, it was necessary to introduce a different approach to explain totally this technique, based on quantum theory.

When light beam interacts with matter, the incident photons that make up the light can be absorbed or scattered, or cannot interact with the material and can pass straight through it. If the energy of a photon corresponds to the energy gap between the ground state of a molecule and an excited state, it can be absorbed and the molecule promoted to the higher energy excited state. This change is measured in absorption spectroscopy by the detection of the loss of that energy of radiation from the light.

However, it is also possible for the photon to interact with the molecule and scatter from it. In this case, there is no need for the photon to have an energy, which matches the difference between two energy levels of the molecule.

Therefore, when the light interacts with the molecule and distorts (polarizes) the cloud of electrons round the nuclei, it forms a short-lived state called a “virtual state”. However, this state is not stable and the photon is quickly re-radiated. The energy changes detected

in vibrational spectroscopy are those required to cause nuclear motion. If only electron cloud distortion is involved in scattering, the photons will be scattered with very small frequency changes, as the electrons are comparatively light. This scattering process is regarded as elastic scattering with emission of a photon of the same energy as the excitation photon, indicated as E_0 . Scattered radiation of the same frequency as the source is called *Rayleigh scattering*.

Nevertheless, if nuclear motion is induced during the scattering process, energy will be transferred either from the incident photon to the molecule or from the molecule to the scattered photon. In this case, the process is inelastic and the energy of the scattered photon is different from that of the incident photon by one vibrational unit, causing the phenomenon known as *Raman scattering*. This event on the other hand is much rarer, which involves only one in 10^6 - 10^8 of the photons scattered.

Fig. 19 shows the basic processes which occur for one vibration. At room temperature, the majority of the molecules are present in the lowest energy level, indicated as ground state. Since the virtual states are not real states of the molecule but are created when the laser interacts with the electrons and causes polarization, the energy of these states is determined by the frequency of the light source used.

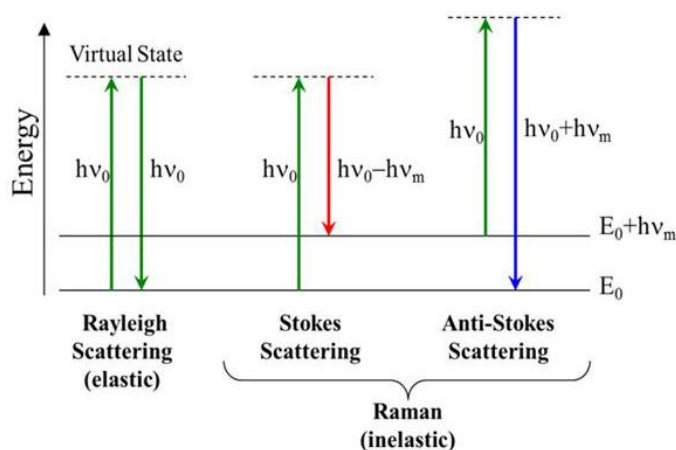


Fig. 19. Diagram of the Rayleigh and Raman processes. Both the low energy (upward arrows) and the scattered energy (downward arrows) have much larger energies than the energy of a vibration.

The elastic process that appears in the left part of the image is known as *Rayleigh scattering*. It will be the most intense process since most photons scatter this way. It does not involve any energy change and consequently the light returns to the same energy state.

Proceeding toward the right, as shown in Fig. 19, a molecule in the ground state ($v = 0$) can adsorb photon of energy $h\nu_0$ and reemit a photon of energy $h\nu_0 - h\nu_m$.

When the scattered radiation is of a lower frequency than the excitation radiation, it is so called *Stokes scattering*.

Finally, *anti-Stokes* occurs when some molecules can already be present in an excited vibrational level $E_0 + h\nu_m$ due to thermal energy. Scattering inelastically from this state to the ground state, they produce a Raman signal of energy $h\nu_0 + h\nu_m$ and a radiation of a higher frequency than that of the source.

The relative intensities of the two inelastic Raman processes depend on the population of the various states of the molecule. The populations of energy states can be expressed by the Boltzmann factor $e^{-h(\nu_1-\nu_0)/kT}$ but, at room temperature, the number of molecules expected to be in an excited vibrational state other than any really low-energy ones will be

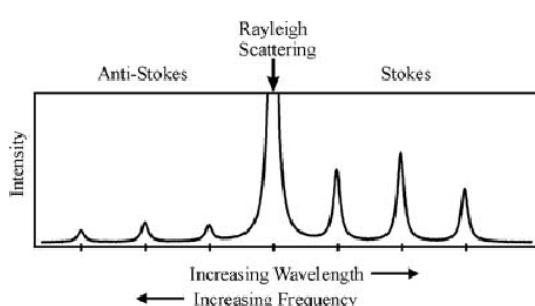


Fig. 20. Comparison between anti-Stokes and Stokes intensity lines.

small. Thus, the anti-Stokes line will be much weaker than the Stokes line because, in thermal equilibrium, the vibrational energy states are less populated than the ground level (Fig. 20). Intense Raman scattering occurs from vibrations that cause a change in the polarizability of the electron cloud round the molecule.

Usually, symmetric vibrations cause the largest changes and give the greatest scattering. The information that the Raman spectrum can give descend almost exclusively by Stokes lines, because they are related to the functional groups of the analyzed sample. The Rayleigh radiation provides no information, as it has the same energy in each sample, while the anti-Stokes lines are generally difficult to be revealed because of their low intensity.

Typically, the instrumentation for Raman spectroscopy consists of a laser source, a sample illumination system, and a suitable spectrometer, as shown in Fig. 21.

The sample to be analyzed is illuminated with a laser beam, and the electromagnetic radiation from the illuminated spot is collected with a lens and sent through a monochromator. At this point, the elastic scattered radiation, which corresponding to the laser line or rather the Rayleigh scattering, is filtered out, while the rest of the collected light is dispersed onto a detector by either a notch filter or a band pass filter.

One of the major difficulty of this technique is to separate the weak inelastically scattered light from the intense Rayleigh scattered laser light, since the first is much less intense than the second.

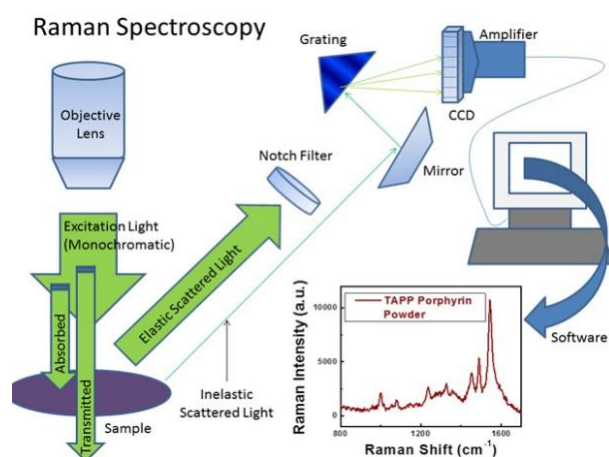


Fig. 21. Schematic Raman components.

The first instrumentations, in fact, were equipped with holographic gratings, which determine the resolution and the range of wavelength that a spectrophotometer can handle, and multiple dispersion stages to achieve a high degree of laser rejection. Moreover, photomultipliers were the detectors of choice for dispersive Raman setups, which resulted in long acquisition times. To date, modern Raman almost employs notch or edge filters for laser rejection and charge-coupled devices (CCD) detectors. In the end, the transducer converts Raman signal into a proportional electrical signal that is processed by computer data system.

3.2 Morphological characterization

3.2.1 3D Laser-scanning Confocal Microscope (CLSM or LSCM)

Confocal laser scanning microscope is a technique for obtaining high-resolution optical images with depth selectivity. The key feature of this microscopy is its ability to acquire in-focus images from selected depths, a process known as optical sectioning. Images are acquired point-by-point and reconstructed with a computer, allowing three-dimensional reconstructions of topologically complex objects. Comparing different techniques, it is

possible to notice that the conventional microscope “sees” as far into the specimen as the light can penetrate, while the confocal microscope only “sees” images on one depth level at a time. In effect, the CLSM achieves a controlled and highly limited depth of focus.

The principle of confocal microscopy was originally patented by Marvin Minsky in 1957, but it took another thirty years to improve and to develop lasers suitable for this instrument. Therefore, it became a standard technique toward the end of the 1980s. In fact, in 1978, Thomas and Cristoph Cremer designed a laser scanning process, which scans the three dimensional surface of an object point-by-point by means of a focused laser beam, and creates the over-all picture by electronic means similar to those used in scanning electron microscopes [81].

In this microscope, a laser beam passes through a light source aperture and then is focused by an objective lens into a small focal volume within or on the surface of a specimen. The scattered and reflected laser light from the illuminated spot passes back through the objective lens, and a beam splitter has the role to separate off some portion of the light into the detection apparatus. After passing a pinhole, the light intensity is detected by a photodetection device, transforming the light signal into an electrical one that is recorded by a computer.

The detector aperture obstructs the light that is not coming from the focal point, as shown by the dotted gray line in Fig. 22. The out-of-focus light is then suppressed, because most of the returning light is blocked by the pinhole and permits one to obtain images of planes at various depths within the sample. Finally, the detected light

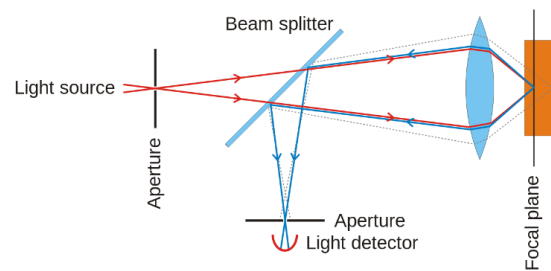


Fig. 22. Principle of confocal microscope.

originating from an illuminated volume element within the specimen represents one pixel in the resulting image, and a whole image is obtained pixel-by-pixel and line-by-line.

Confocal microscopy provides the capacity for direct, noninvasive, serial optical sectioning of intact, thick, and living specimens with a minimum of sample preparation. For all these reasons, this technique is widely used in numerous biological science disciplines, from cell biology and genetics to microbiology and development biology. Nevertheless, it is also used in quantum optics, nano-crystal imaging and spectroscopy.

3.2.2 Scanning Electron Microscope (SEM)

A scanning electron microscope is an instrumentation capable of producing images of a sample by scanning it with a focused beam of electrons that interact with the atoms in the sample. This interaction producing various signals that can be detected and that contain information about the sample's surface topography and composition. The electron beam is generally scanned in a raster scan pattern, and the beam's position is combined with the detected signal to make an image. SEM can produce very high-resolution images of a sample surface, revealing details less than 1 nm in size. Moreover, specimens can be observed in high vacuum, in low vacuum, in wet conditions, and at a wide range of cryogenic or elevated temperatures.

The most common SEM mode is the detection of secondary electrons emitted by atoms excited by the electron beam. The number of secondary electrons that can be detected depends on the angle at which beam meets surface of specimen. By scanning the sample and collecting the secondary electrons with a special detector, is possible to create an image displaying the topography of the analyzed surface.

From the beginning of electron microscopy, the imaging of solid samples was an important goal, especially because the methods for producing thin samples for analyses were only developed later. Historically, during the 1930s Max Knoll tried to test a very different way of imaging solid samples for the study of the targets of television camera tubes, inventing in 1935 the scanning electron microscopy. About two years later, in 1938 Manfred von Ardenne developed the first and true scanning electron microscope with high magnification by scanning a very small raster with a demagnified and finely focused electron beam, thanks to the invention and introduction of a sub-micron probe [82]. Ardenne applied the scanning principle not only to achieve magnification but also to purposefully eliminate the chromatic aberration otherwise inherent in the electron microscope. He further discussed the various detection modes, possibilities and theory of SEM, together with the construction of the first high magnification SEM. Further work was reported by Zworykin's group, followed by the Cambridge groups in the 1950s and early 1960s headed by Charles Oatley [83], all of which finally led to the marketing of the first commercial instrument in 1965 by Cambridge Scientific Instrument Company as the "Stereoscan".

Briefly, in a typical SEM (Fig. 23) an electron beam is thermionically emitted from an electron gun fitted with a tungsten filament cathode. In thermionic electron gun is normally used tungsten for several reasons: it has the highest melting point, the lowest vapour pressure of all metals, it is low cost, and finally allows to be heated for electron emission. Depending on requirements, it is possible to use also other types of electron emitters, such as lanthanum hexaboride (LaB₆) or zirconium oxide cathodes. Then, the electron beam,

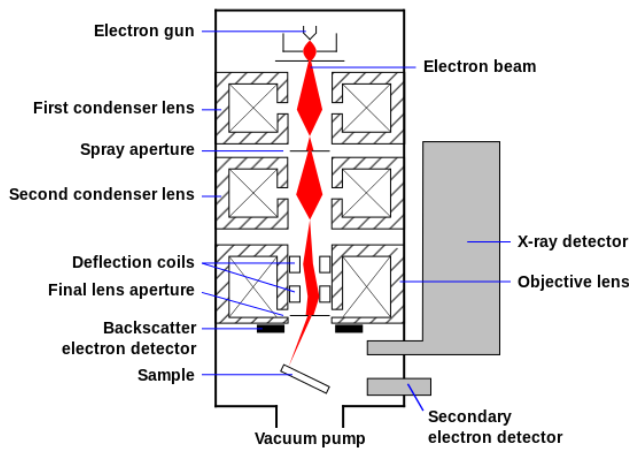


Fig. 23. Diagram of the various components of SEM.

which typically has an energy ranging from 0.2 keV to 40 keV, is focused by one or two condenser lenses to a spot about 0.4 nm to 5 nm in diameter. The beam passes through pairs of scanning coils or pairs of deflector plates in the electron column, typically in the final lens, which deflect the beam in the x and y axes so that it scans in a raster fashion over a rectangular area of the sample surface.

When the primary electron beam interacts with the sample, the electrons lose energy by repeated random scattering and absorption within a teardrop-shaped volume of the specimen known as the interaction volume, which extends from less than 100 nm to approximately 5 μm into the surface. The energy exchange between the electron beam and the sample results in the reflection of high-energy electrons by elastic scattering, emission of secondary electrons by inelastic scattering, and the emission of electromagnetic radiation, each of which can be detected by specialized detectors. The beam current absorbed by the specimen can also be detected and used to create images of the distribution of specimen current. Electronic amplifiers of various types are used to amplify the signals, which are displayed as variations in brightness on a computer monitor. Each pixel of computer videomemory is synchronized with the position of the beam on the specimen in the microscope, and the resulting image is therefore a distribution map of the intensity of the signal being emitted from the scanned area of the specimen. Finally, the image is saved into a computer data storage.

3.3 Structural characterization

3.3.1 X-ray Diffraction (XRD)

X-ray diffraction is a rapid analytical tool primarily employed for phase identification of a crystalline material. It can provide information on unit cell dimensions and measure the average spacing between layers or rows of atoms.

This technique is most widely used for the determination of average bulk composition and the identification of unknown crystalline materials and solids (e.g. minerals, inorganic compounds). Moreover, it has a wide application in various fields, from geology, environmental science, material science, engineering to biology.

The discovery of the fundamental principles of XRD was made in 1912 by Max von Laue [84], who discovered that crystalline substances act as three-dimensional diffraction gratings for X-ray wavelengths similar to the spacing of planes in a crystal lattice.

X-ray diffraction is based on constructive interference of monochromatic X-rays and a crystalline sample. These X-rays are generated by a cathode ray tube, filtered to produce monochromatic radiation, collimated to concentrate, and directed toward the sample. The interaction of the incident rays with the sample produces constructive interference (and a diffracted ray) when conditions satisfy Bragg's Law:

$$n\lambda = 2d \sin \theta.$$

where n is a positive integer, λ is the wavelength of incident wave, d is the interplanar distance, and θ is the scattering angle.

This law relates the wavelength of electromagnetic radiation to the diffraction angle and the lattice spacing in a crystalline sample. Then, these diffracted X-rays are detected, processed and counted.

All possible diffraction directions of the lattice should be obtained due to the random orientation of the powdered material by scanning the sample through a range of 2θ angles. Subsequently, the conversion of the diffraction peaks to d-spacings allows identification of the mineral because each mineral has a set of unique d-spacings.

Typically, this is achieved by comparison of d-spacings with standard reference patterns.

3.4 Chemical characterization

3.4.1 Scanning Chemical Microscope (SCHEM™)

Scanning chemical microscopy (SCHEM) is a technique that falls within the class of scanning probe microscopy (SPM) that is used to measure the local electrochemical behavior of liquid/solid, liquid/gas and liquid/liquid interfaces.

This particular tool can be employed to visualize the distribution map of local pH value formed on the surface of solid substances with high spatial resolution, since it is possible to express the degree of acidity or alkalinity of a liquid solution by pH value.

The analysis of the solid sample, which may be in the form of a flat sheets, fibers, disks, granules, etc., is performed by placing the specimen in contact with the gel film on top of the pH imaging sensor.

The pH level of the film changes in accordance with its contact with the analyzed material, and successively, the variations of the pH in the film are measured at multiple points by flat sensor.

By imaging and mapping these local changes in the pH levels at various points in the film, this technology allows to obtain a lot of specific surface chemical information of solid material based on pH distribution that was previously impossible or much harder to get.

This experimental instrument can be employed across various and numerous range of field, from material science to that of biology and biomedicine.

CHAPTER IV: MATERIALS AND METHODS

4.1 Si₃N₄ material

4.1.1 Samples preparation

Amedica Corporation (Salt Lake City, UT 84119, USA) produced Si₃N₄ used in this study. The samples present same geometry and are circular disks of Ø 12.7 mm × 3 mm. In addition, they were fabricated in order to obtain the “*as-fabricated* or *as-sintered*” material, called the Untreated sample in this work, and two different surface morphologies, designated “*as fired*”, and “*as polished*”.

The synthesis of disks followed the conventional ceramic fabrication techniques. In this process, Si₃N₄ powder (Ube SN E-10, Ube City, Japan) was mixed with Y₂O₃ (Grade C, H. C. Starck, Munich, Germany) and Al₂O₃ (SA8-DBM, Baikowski/Malakoff, Charlotte, NC) sintering aids and cold-pressed at room temperature into disk-shaped samples. Progressively, the biomaterials were sintered in a nitrogen atmosphere with a temperature higher than 1700°C to close porosity, and further were densified by hot isostatic pressing using a temperature above 1650°C and N₂ gas pressures higher than 200 MPa.

The disk surfaces of Si₃N₄ were, then, divided into two groups for the synthesis of the different morphologies.

The first group, called as fired, was produced with one major face left as fired and the remaining faces ground flat using a 1000 grit diamond-impregnated wheel on a surface grinder (ACC 12-24DX Grind-X, Okamoto Corp., Vernon Hills, IL).

The second group, designated as polished, was lapped on the major face using 6 µm diamond (Engis, Wheeling, IL) on a lapping machine (Lapmaster, Mt. Prospect, IL), and subsequently polished using colloidal silica (Leco, St. Joseph, MI).

All samples were, afterwards, exposed to ultrasonic cleaning in deionized water of 17.5 MX cm resistivity (750II, Myron L Company, Carlsbad, CA) for 30 minutes to remove contaminants [85].

Finally, to probe the effect of surface chemistry on the bacterial response, the surfaces were modified by wet chemical etching and by oxidation treatment described in Section 4.1.2.

4.1.2 Surface treatments description

Experiments were conducted on three different surface treatments, “*HF etched*”, “*N₂ bake*” and “*Thermally oxidized*”, which will be indicated in this work simply as HF, N₂ and Thermally oxidized. The following describes the synthesis techniques:

- Wet Chemical Etching: *HF etched* - Si₃N₄ were immersed for 45 seconds in a 5 wt.% of hydrofluoric acid (HF) solution and then transferred into a continuously refreshed DI water bath for 30 minutes. Samples were dried under a stream of filtered N₂ and stored in a desiccator containing hygroscopic media (Indicating Drierite, W.A. Hammond DRIERITE Co., Xenia, OH) under partial vacuum (~100 Torr) to slow spontaneous re-oxidation.
- Nitrogen Heat Treatment: *N₂ bake* - Samples were placed in a batch furnace (Centorr Vacuum Industries, Nashua, NH) and evacuated to 250 mTorr. Later, they were back-filled with filtered N₂ and subsequently heated to 1400°C for 30 minutes. This heat treatment could be seen potentially as an alternative to the HF etching treatment because it was hypothesized that re-exposing Si₃N₄ to a N₂ atmosphere at high temperatures might increase the density of surface amines relative to hydroxyl groups.
- Oxidation Treatment: *Thermally oxidized* - This process is based on the procedure developed in 1976 by Raider et al., who demonstrated that Si₃N₄ chemically deposited using chemical vapor deposition technique (CVD) is readily oxidized upon exposure to ambient atmosphere at 1070°C [86]. Also another study written in 1996 by Butt et al. showed similar results for two commercially-produced Si₃N₄ powders [87]. In this way, following the Raider’s protocol, the samples were oxidized using an open-air kiln (Deltech, Denver, CO) for 7 hours at 1070°C. This treatment was employed because it was believed that it should completely oxidize the surface, yielding the maximum concentration of hydroxyl groups and pushing the surface composition as far as possible to the oxide end of the nitride-oxide spectrum as possible.

4.2 Bacterial strains preparation

P. gingivalis, *T. denticola* and *T. forsythia*, the three oral bacteria that compose the “*red complex*”, were examined in the present study.

All the strains were purchased from the American Type Culture Collection (ATCC), a Global Bioresource Center housed in a Manassan (Virginia, USA), and supplied by the Department of Immunology of Kyoto Prefectural University of Medicine, Graduate School of Medical Science (Kyoto, Japan).

Although the three species have different preferred growth media, identical procedures were used during the preparations of culture pellet and Petri dishes.

4.2.1 *Porphyromonas gingivalis* (ATCC 33277)

a) Culture conditions

Microbial cells of *P. gingivalis* ATCC® 33277™ were taken from stocks stored at -80°C and heated in a water sonicator (IWAKI Sonicator SHK-200B) up to 37°C.

In a 300 ml flask (Pyrex) were added 200 ml of deionized water and 5 g of broth-enriched heart infusion (BHI) (Nissui Pharmaceutical, Tokyo), which is a solution in water of essential nutritional components for the bacterial growth (Table 3).

Table 3: Composition of BHI (25 g in 1 liter distilled water).

Components	Quantity (g)
Sodium Chloride	5.0
Peptones	10.0
Heart extract	10.0

After obtaining a homogeneous solution, 10 ml of BHI were collected and paid into testing tubes for autoclaving at 121°C for 20 minutes. Later the sterilization, the tubes were stored in a refrigerator at 4°C.

Using a laminar flow cabinet (Brand Bio-Lab), 100 µl of *P. gingivalis*'s cell suspension were added to each testing tube containing 10 ml of BHI and were supplemented 2 ml of Foetal Bovine Serum (FBS) (Biological Industries). This serum is the widely used growth

supplement for cell culture media because it contains more growth factors, a high content of embryogenic growth element that satisfies metabolic requirement for the culture of cells, and has a very low level of antibodies (Table 4).

Table 4: Composition of FBS.

Components	Units	Components	Units
Alanine Transaminase (ALT)	7 μ /L	Albumin	2.9 g/dL
Alkaline Phosphatase	405 μ /L	Bilirubin	0.14 mg/dL
Aspartate Aminotransferase (AST)	23 μ /L	Calcium	13.6 mg/dL
Lactate Dehydrogenase	969 μ /L	Cholesterol	33 mg/dL
Hemoglobin	14.8 mg/dL	Blood Urea Nitrogen (BUN)	18 mg/dL
Chloride	103.3 MMol/L	Glucose	62.7 mg/dL
Potassium	>10 MMol/L	Sodium	140 MMol/L

Finally, the testing tubes were incubated (Espec BNA-111) at 37°C for one week under anaerobic condition, that was obtained by use of sterile butyl rubber stoppers on testing tubes, so that an anaerobic gas headspace is retained.

b) Preparation of culture pellet and Petri dishes

Bacterial culture in enriched BHI medium was harvest by centrifugation (IWAKI centrifuge, TC Mate CFS-300) at 3000 rpm for 10 minutes. The supernatant was eliminated and the resulting pellet was suspended in 50 ml D-phosphate buffer saline (D-PBS) (Nacalai Tesque, Kyoto) to remove residual growth media. Since the initial density of microbial culture was 5×10^5 colony forming unit (CFU), the dilution with D-PBS allows obtaining a final bacterial density equal to 10^{10} CFU.

Thereafter, 100 μ l of liquid solution were transferred in Petri dishes containing CDC anaerobe 5% sheep blood agar (BD, Becton, Dickinson and Company, Sparks, MD USA) (Table 5), and were added Si₃N₄'s samples on agar surface.

Obviously, all discs of Si₃N₄ were autoclaved in laboratory (Tomy LSX-500) before use to prevent contamination.

Table 5: Composition of CDC anaerobe 5% sheep blood agar (quantity in 1 liter purified water).

Components	Quantity (g)	Components	Quantity (g)
Pancreatic digest of casein	15.0	Agar	20.0
Papaic digest of soy beam	5.0	Yeast extract	5.0
Sodium chloride	5.0	Hemin	0.005
Vitamin K ₁	0.01	L-Cysteine	0.4

Ultimately, dishes were incubated at 37°C in an anaerobic cabinet under anaerobic gas mixture (10% CO₂, 10% H₂, 80% N₂) (AnaeroPack®-Anaero, Mitsubishi Gas Chemical Co., Japan) for almost two weeks.

4.2.2 *Treponema denticola* (ATCC 35405) and *Tannerella Forsithya* (ATCC 43037)

a) Culture conditions

Pathological samples of *T. denticola* ATCC® 35405™ and *T. forsythia* ATCC® 43037™, conserved at -80°C, were heated up to 37°C using a water sonicator (IWAKI Sonicator SHK-200B).

In a 200 ml flask (Pyrex) were suspended 3.7 g of Bacto™ Brain Heart Infusion (BD, Becton, Dickinson and Company, Sparks, MD USA) (Table 6) in 100 ml of purified water.

Table 6: Composition of Bacto™ Brain Heart Infusion (in 1 liter purified water).

Components	Quantity (g)	Components	Quantity (g)
Calf brains	7.7	Dextrose	2.0
Beef heart	9.8	Sodium chloride	5.0
Proteose peptone	10.0	Disodium phosphate	2.5

The preparation was mixed thoroughly, heated with frequent agitation and boiled for 1 minute to completely dissolve the powder. After this operation, the solution was divided into 10 testing tubes each of 10 ml and autoclaved at 121°C for 15 minutes. Later the sterilization, the tubes were stored in a refrigerator at 4°C.

Using a laminar flow cabinet (Brand Bio-Lab), 100 μ l of *T. denticola* and *T. forsythia* cell suspension were added separately in 10 ml of broth previously prepared supplemented with 2 ml of FBS (Biological Industries).

Finally, each testing tubes was closed with sterile butyl rubber stopper and incubated (Espec BNA-111) under anaerobic condition for one week at 37°C.

b) Preparation of culture pellet and Petri dishes

The same operations performed for the preparation of *P. gingivalis*'s culture pellet and Petri dishes have been performed for *T. denticola* and *T. forsythia* bacterial strains.

4.3 Samples characterization methods

4.3.1 Raman Spectroscopy

All the experimental Raman analyses and data of Si₃N₄ samples reported in this thesis were conducted using two different spectroscopic instruments.

The characterization and exploration of treated surfaces were obtained through the *Jobin-Yvon T-64000 Raman Spectrometer* (Horiba/Jobin-Yvon., Kyoto, Japan) in Ceramic Physics Laboratory of Kyoto Institute of Technology (Kyoto, Japan).

Instead, the investigation of the possible interaction between different surfaces morphologies and treatments and bacterial strains was performed using the *LabRAM ARAMIS HR800* (Horiba/Jobin-Yvon., Kyoto, Japan) at the Kyoto Integrated Science and Technology Bio-Analysis Center (Kyoto, Japan).

- *Jobin-Yvon T-64000 Raman Spectrometer and data analysis*

Raman spectra were acquired using a confocal (optical) microprobe at room temperature and a single monochromator equipped with a nitrogen-cooled 1024 \times 256 pixels CCD camera (CCD-3500V, Horiba Ltd., Kyoto, Japan).

An overall view of Raman instrument is shown in Fig. 24.



Fig. 24. T-64000 Raman spectrometer.

The excitation frequency used in the experiments was the 532 nm blue line of an Ar-ion laser operating at a power of 100 mW, and was used a 1800 gr/mm (grooves per millimeter) grating with a resolution approximately of 0.15 cm^{-1} . In fact, the gratings determine the resolution and the range of wavelength that a spectrophotometer can handle.

The spectrum integration time was typically 30 seconds, averaging the recorded spectra over three successive measurements.

A confocal configuration of the Raman probe was adopted throughout all the experiments, using a $100\times$ objective lens in order to exclude the photons scattered from out-of-focus regions of the probe. The samples were placed on an x–y axes motorized stage (lateral resolution of $0.1 \mu\text{m}$), which allowed the collection of maps on the surface. Moreover, finely tuned z-axis displacements allowed the collection of spectra at different depths.

A signal from a He-Ne lamp was taken throughout all measurements as an internal reference for Raman peak positions.

Lastly, Raman data were analyzed by using commercially available software (LabSpec, Horiba/Jobin-Yvon, Kyoto, Japan), and band parameters were obtained through fitting the raw experimental spectra with Lorentzian curves [85].

- *LabRAM ARAMIS and data analysis*

Spectra of bacterial interaction with different surfaces were collected using a biological confocal Raman (Fig. 25), whose emissions was monitored by a single monochromator connected with an air-cooled CCD detector (Andor DV420-OE322; 1024×256 pixels).

Compared with the previous instrument, this is a full automatic Raman system in which the laser and gratings are handled by computer.



Fig. 25. LabRAM ARAMIS spectroscopic system.

Before starting the acquisition of sample's spectra, it was performed the wavelength calibration of spectroscopic machine by measuring silicon wafer and evaluating the first-order phonon band of silicon at 520 cm^{-1} .

Experimental measurements were conducted with an excitation source equal to 633 nm helium-neon (He-Ne) laser with a power of 10 mW that operates at a wavelength in the red part of the visible spectrum.

The development of high power mid-infrared (mid-IR) and near-infrared (near-IR) lasers was a key factor for the acquisition of Raman spectra of biological materials. Firstly, the high background signal associated with molecular fluorescence can be eliminated since photons do not possess the required energy to excite such transition and in this manner is possible to prevent thermal effects on samples. Secondly, mid and near-IR laser induce less photodamage compared UV or other sources [88, 89].

All Raman data were recorded with an exposure time of 60 seconds and with a number of accumulation equal to four in the $492\text{-}2370\text{ cm}^{-1}$ spectra range. For the experiments it was used a 600 gr/mm grating, a D.03 holographic notch filter to control the intensity of the laser light that hits sample's surface, and a $100\times$ objective lens. Moreover, was employed a $100\text{ }\mu\text{m}$ cross-slit and a $200\text{ }\mu\text{m}$ confocal pinhole that controls the thickness of the plane of focus.

Raman spectral acquisition and preprocessing of preliminary data such as baseline subtraction and smoothing were carried out using commercially available software (LabSpec, Horiba/Jobin-Yvon, Kyoto, Japan). All spectra were analyzed in the 600-1750

cm⁻¹ wavenumber region and normalized to a range from 0 to 1 with reference to the peak of greatest intensity (1244 cm⁻¹). The Raman spectrum of each superficial treatment was calculated as the average of six measurements at different arbitrary sites on the sample and, in the end, analysis data were processed with available software package (Origin 8.5, OriginLab Co., Northampton, MA, USA).

4.3.2 3D Laser-Scanning Confocal Microscopy

Micrographs of the selected surfaces were collected by means of a 3D laser-scanning microscope (VK-X200K Series, Keyence, Osaka, Japan). The surface has been analyzing recital of random points on the entire extension of the material. Five images were collected for each point using a 10×, 50×, and 150× objective lens, with a numerical aperture of 0.9. In this work were included only the images belonging to 150× magnification.

4.3.3 Scanning Electron Microscopy

Microstructural characterizations on Si₃N₄ surfaces were conducted using a field emission gun scanning electron microscope (FEG-SEM) (ZEISS SIGMA VP, Germany) equipped with variable pressure (VP-SEM) and with a working range of 1-30 kV. Material analysis at high resolution was provided by EDX system (Brucher Quantax 200, Berlin, Germany).

4.3.4 X-ray Diffraction

XRD patterns were acquired using a PW3830 X-ray generator PAWalytical operated at 40 kV and 30 mA, using a Cu anode material and diffracted Beam PW1752 Curved graphite monochromator.

Diffraction patterns were recorded over a range of 5° to 140° 2θ, with step size of 0.05°. The identification of secondary phases was conducted with the available software Christallographica through the comparison of spectra taken experimentally and those present in the ICDD PDF-4 Database.

4.3.5 Fluorescence Microscopy

The investigation of bacterial culture was observed by fluorescence microscopy (BZ-X700; Keyence, Osaka, Japan) after 24 h exposure to the Si₃N₄ surface. The coloring of the bacterial cells was carried out with propidium iodide (PI) and 5-(and 6)-carboxyfluorescein diacetate (CFDA) solutions (Bacstain-PI solution and Bacstain-CFDA, respectively; Dojindo Lab., Osaka, Japan). PI colored dead membrane-injured bacteria with red emission, while CFDA stained green the living bacteria.

4.3.6 pH Microscopy

Local pH experiments were conducted using a recently launched device (pH microscope, SCHEM-110; Horiba, Kyoto, Japan), capable of measuring and mapping local pH values at the surface of solids. In performing the pH mapping experiment, the Si₃N₄ sample was fully embedded into an acidic gel consisting of artificial saliva, KCl, and agar (a jelly-like substance obtained from polysaccharide agarose contained in algae agarophytes). The pH-imaging sensor consisted of a flat semiconductor plate with a total sensing area of 2.5 × 2.5 cm. The highest spatial resolution and the pH sensitivity of the sensor were 100 μm and 0.1 in pH, respectively. The sensor was equipped with a light addressable potentiometric sensor, proton-sensitive, and capable of perceiving the protons coming from the electrolyte. A light beam was directed from the backside of the sensor with a bias voltage applied between the electrolyte and the backside. Since the characterization of the AC photocurrent, which is induced by the modulated illumination from the backside of the sensor, depended on the amount of protons at the sensor surface, the pH value could be determined to a high degree of precision by measuring the local value of electric current. The detected current signals were then converted into a color scale pixel, with each pixel arranged to the pH image using image analysis software (Image Pro Plus, Media Cybernetics, MD, USA) in order to generate a visual pH map around the embedded Si₃N₄ sample. The mapping experiments were repeated after increasing periods of time since the sample was embedded into the acidic gel.

CHAPTER V: RESULTS AND DISCUSSION

5.1 Si₃N₄ surfaces characterization

5.1.1 Raman investigation and surface topography

Before starting the discussion of the data, in Fig. 26 a diagram is illustrated to summarize the steps of the synthesis of Si₃N₄ samples studied in this work, in order to make easier and faster their recognition and comparison during the analysis.

The green arrows represent the initial process of synthesis, which allows to obtain from the powder of Si₃N₄ the Untreated samples in the two superficial morphologies, *as fired*, that is characterized by nanostructure features, and *polished*, which has a smooth face. The difference between the two morphologies is that the latter has undergone further machining process than the first. The red arrows, instead, represent the different manufacturing processes, that is to say chemical and thermal treatments.

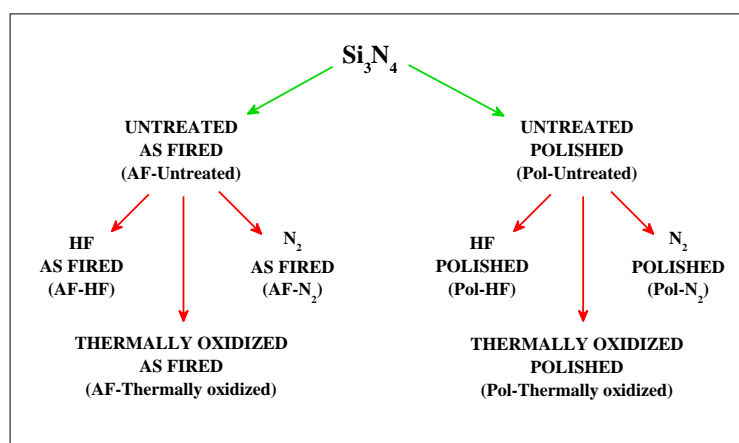


Fig. 26. Schematic diagram of the production of Si₃N₄ samples.

In figure 27 it is reported a representative spectrum of β -Si₃N₄ in the 142-764 cm⁻¹ wavenumber region. It is possible to observe the signal from a He-Ne lamp collected in all experimental measurements (peak that falls approximately to 500 cm⁻¹) and the three intense Raman bands appearing at about 180, 201, and 224 cm⁻¹ that represent the E_{2g} , A_g , and E_{1g} active vibrational modes of the skeletal Si-N bonds in the β -Si₃N₄ structure, respectively [90].

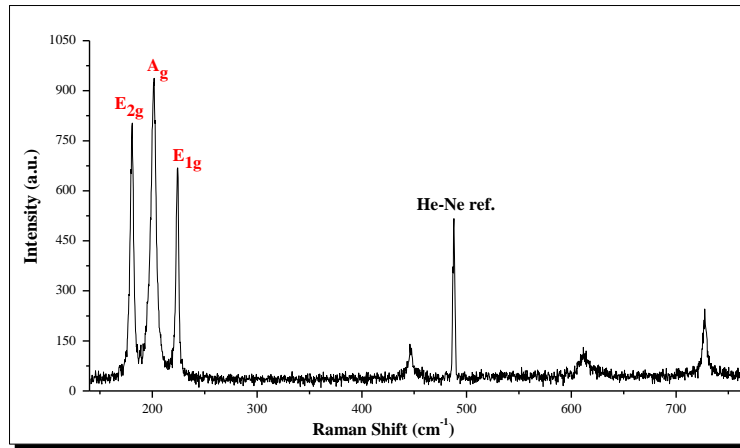


Fig. 27. Typical Raman spectrum of β - Si_3N_4 .

Since the three bands mentioned above represent the region of greatest spectroscopic interest, the results of Raman spectra of different sample surfaces will be presented considering only the $150\text{-}250\text{ cm}^{-1}$ range. Furthermore, firstly the spectra of the *as fired* surfaces are described; secondly the results of *polished* surfaces are illustrated.

- *As fired surface morphology*

The spectroscopic investigations conducted on these samples are shown in Fig. 28.

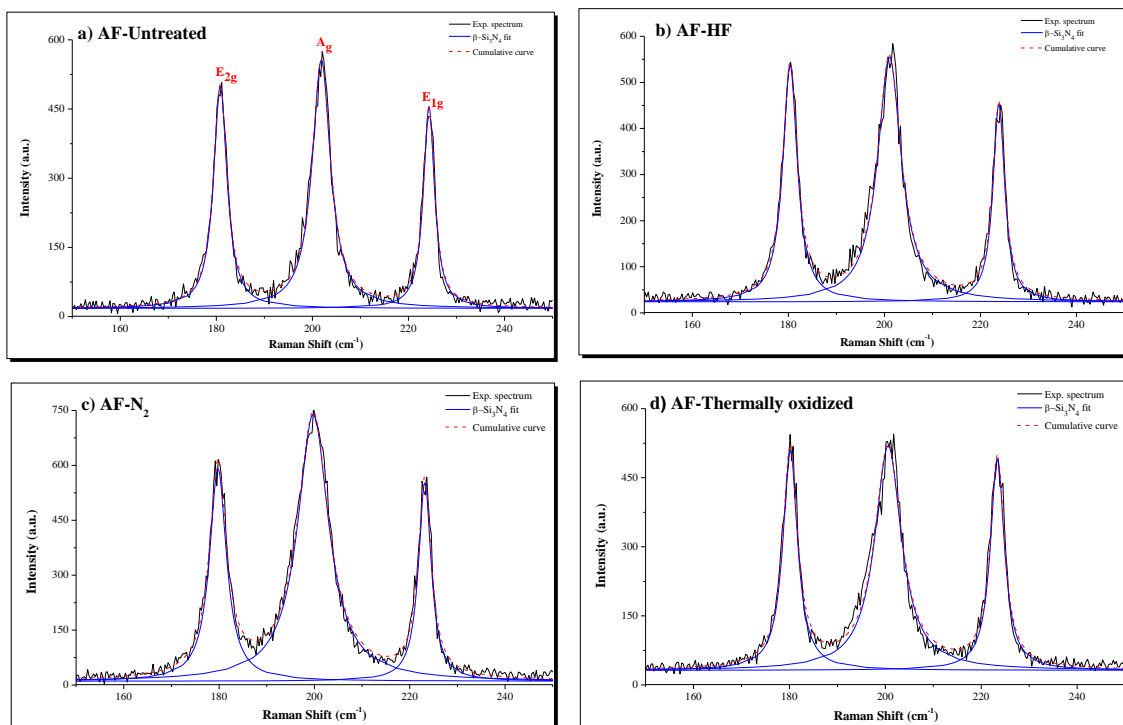


Fig. 28. Raman spectra of β - Si_3N_4 in the $150\text{-}250\text{ cm}^{-1}$ region, collected on the: a) AF-Untreated, b) AF-HF, c) AF- N_2 , and d) AF-Thermally oxidized.

The Raman spectra of the four different treatments have not demonstrated significant and substantial differences. The position of triplet's peaks, indicated in Table 7, is about the same in all samples, and also their relative intensity order, that follows the tendency $A_g > E_{2g} > E_{1g}$, remains unchanged in all manufacturing processes.

Table 7. Peaks position of triplet in *as fired* samples.

Superficial treatment	Center max		
	E_{2g}	A_g	E_{1g}
AF-Untreated	180.81	201.86	224.27
AF-HF	180.35	201.05	223.83
AF-N ₂	179.77	199.76	223.17
AF-Thermally oxidized	180.17	200.59	223.36

Furthermore, these observations are supported by surface's micrographs collected by a 3D laser-scanning microscope (CLSM or LSCM) (Fig. 29).

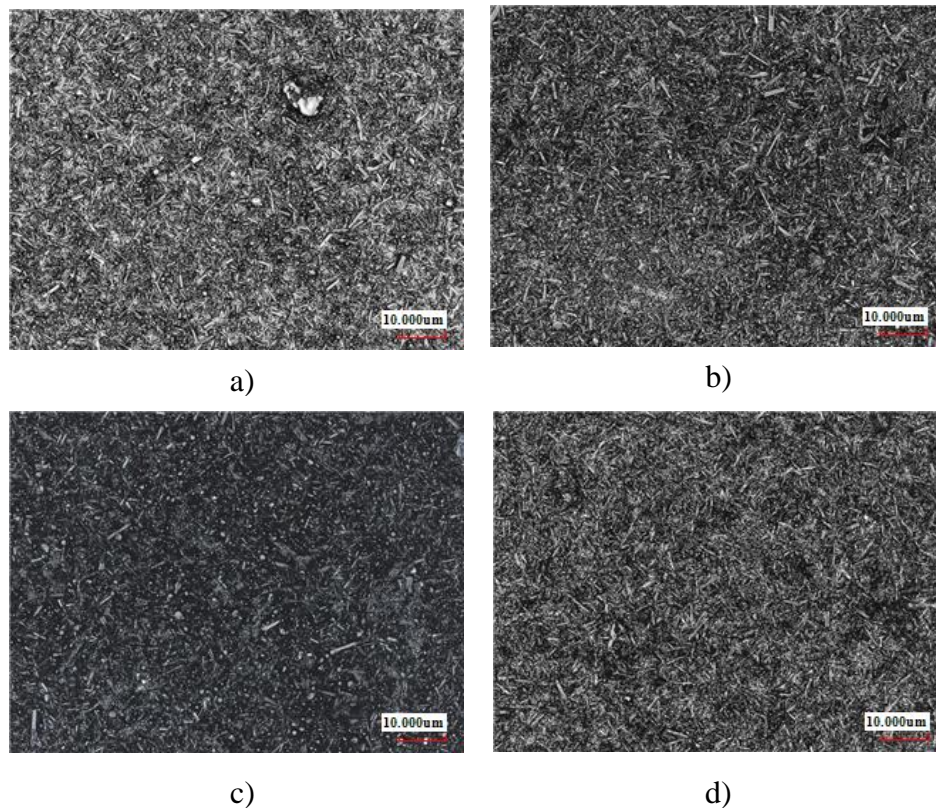


Fig. 29. Scanning laser micrographs of: a) AF-Untreated, b) AF-HF, c) AF-N₂, and d) AF-Thermally oxidized.

As seen in images, it is possible to identify remarkable similarities between the four figures, because using this magnification (150×) in each treatment the same texture appears and all samples exhibit classic protruding anisotropic and hexagonal β - Si_3N_4 grains.

Therefore, it could say that the surface chemistry and morphology of the examined *as fired* Si_3N_4 could not be varied significantly through the thermal and chemical treatments, and that all surfaces exhibit anisotropic and stochastically oriented β - Si_3N_4 grains.

- *Polished surface morphology*

Raman analyses conducted on *polished* samples have revealed a very particular superficial behavior of these treatments, in some cases discordant with previous data.

Figure 30 allows to underline the significant and marked diversity between the Raman spectra of various treatments.

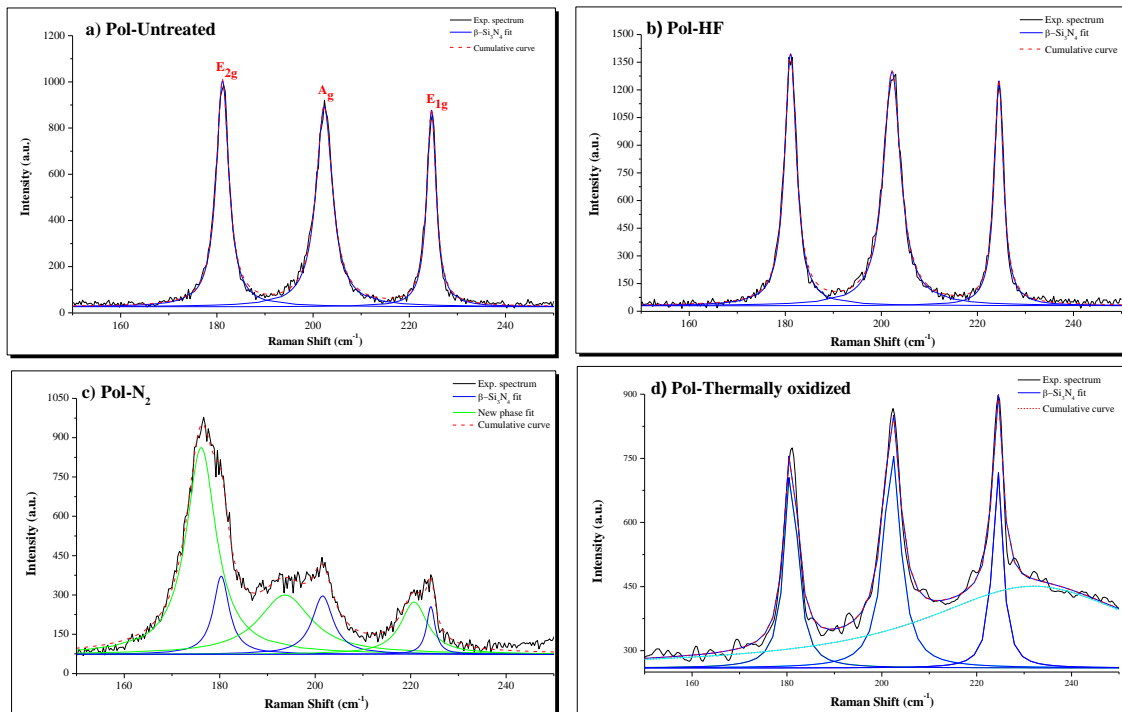


Fig. 30. Raman spectra of β - Si_3N_4 in the 150-250 cm^{-1} region, collected on: a) Pol-Untreated, b) Pol-HF, c) Pol- N_2 , and d) Pol-Thermally oxidized.

Also in this case, as in the previous data and interpretation, the Pol-Untreated and Pol-HF samples (Fig. 30 a) and b), respectively) present equal Raman performance. The relative intensity among bands belonging to the shown triplet remained unchanged and no

significant broadening can be detected in any of the triplet constituents. Moreover, it is not identified a significant change in the position of E_{2g} , A_g , and E_{1g} , as reported in Table 8.

Table 8. Peaks position of triplet in Untreated and HF *polished* samples.

Superficial treatment	Center max		
	E_{2g}	A_g	E_{1g}
Pol-Untreated	181.17	202.33	224.63
Pol-HF	181.10	202.23	224.48

However, one clear difference could be recognized. The trend of relative intensity is modified, since the first two are reversed, as compared to the *as fired* samples, with the intensity order that becoming $E_{2g} > A_g > E_{1g}$. In the first approximation, these distinct features can be depending on the optical configuration and on the crystallographic orientation of the surface crystallites of β - Si_3N_4 ceramics [90].

A drastic morphological change is, instead, observed in Raman spectrum collected from the sample thermally treated in N_2 (Pol- N_2), as shown in Fig. 30 c).

From data processing, it is still possible to identify the original triplet belonging to the Pol-Untreated and Pol-HF samples, and to observe both identical peaks position (Table 9) and the same intensity order.

Nevertheless, it is present an additional triplet that is significantly broadened and shifted toward lower emission frequencies.

Table 9. Peaks position of double triplet in N_2 *polished* sample.

Superficial treatment	Center max		
	E_{2g}	A_g	E_{1g}
Pol- N_2	180.32	201.56	224.23
	New triplet peaks position		
	176.11	193.67	220.72

These phenomena that affect only new peaks and not the classic bands of triplet could be explained by the occurrence of two events: a recrystallization process of the sample

surface, and a following heat treatment composition variation. In fact, the morphological differences detected in the N₂-annealed sample cannot only be due to internal stresses, but they could be interpreted in terms of stoichiometry changes.

Lastly, the Pol-Thermally oxidized sample shown in Fig. 30 d) does not exhibit this additional and shifted triplet, and the triplet peaks position are unchanged (Table 10).

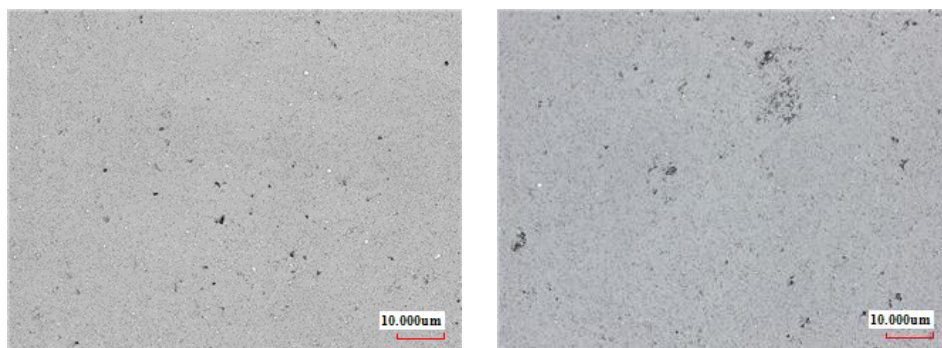
Table 10. Peaks position in Thermally oxidized *polished* sample.

Superficial treatment	Center max		
	E _{2g}	A _g	E _{1g}
Pol-Thermally oxidized	180.89	202.15	224.40

However, it presents several differences. Primarily, there is the appearance of a background and the absolute intensities of all three bands decrease; secondly, the spectrum could yet be deconvoluted into the main triplet overlapped to a quite broad emission centered at approximately 230 cm⁻¹; thirdly, the trend of triplet's band intensities is inverted in comparison to Pol-Untreated and Pol-HF samples, because it is presented as E_{1g} > A_g > E_{2g}.

The morphological study has again marked these observations and the differences between the superficial treatments.

The micrographs collected by a CLSM are given in Fig. 31.



a)

b)

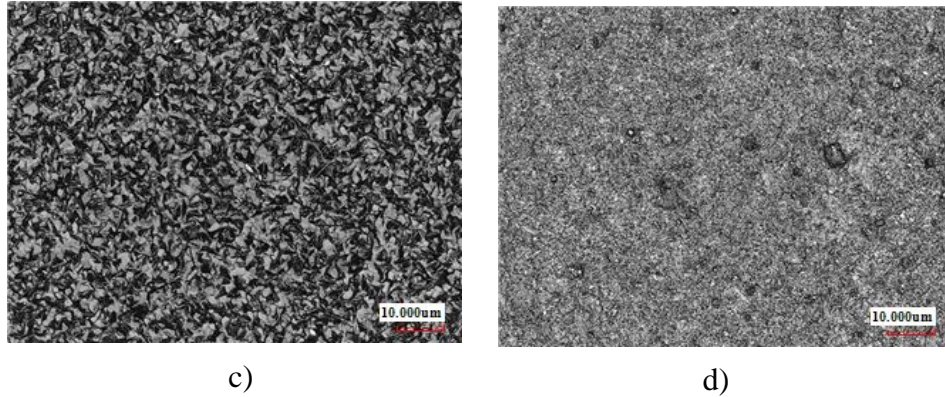


Fig. 31. Scanning laser micrographs on: a) Pol-Untreated, b) Pol-HF, c) Pol-N₂, and d) Pol-Thermally oxidized.

As in the previous case, the Pol-Untreated and Pol-HF specimens manifest extremely equal surfaces, and their images seem to be those of the same sample. The surface is completely smooth and the characteristic hexagonal and elongated β -Si₃N₄ grains are not visible.

On the contrary, both thermally-treated (Pol-N₂ and Pol-Thermally oxidized) exhibit an anomalous and complex texture, particularly after the N₂ thermal process.

Because all these samples have undergone a process of polishing, any their morphological variations are strongly evident even at this scale of magnification. In fact, the previous *as fired* bioceramics, which have not been subject to this procedure, do not present these superficial differences.

Both the investigation techniques just now described and used for the characterization have revealed a substantial change and modification of the surface layer of Si₃N₄. Nevertheless, they have not provided a clear and complete explanation of the formation of this unknown crystalline material.

Therefore, it is necessary to introduce other analytical techniques that allow this identification and provide additional information about the material investigated in this work.

5.1.2 XRD and SEM analyses

The accuracy of the XRD quantification method in analyzing Si₃N₄ materials gives a possible explanation of the appearance of these outsider layers in *polished* compounds. The XRD of the *as fired* samples will not be reported here, because they do not show significant differences from those *polished*.

Figures 32 and 33 show the patterns of Pol-Untreated and Pol-HF samples, respectively, in the 10-80° 2 θ degree range, obtained through comparison of the measurements with the ICDD PDF-4 database.

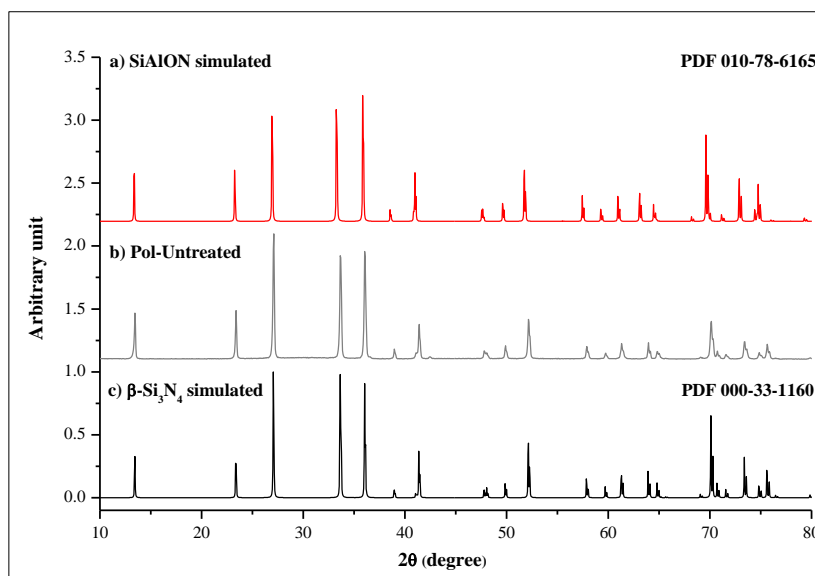


Fig. 32. XRD pattern of Pol-Untreated sample.

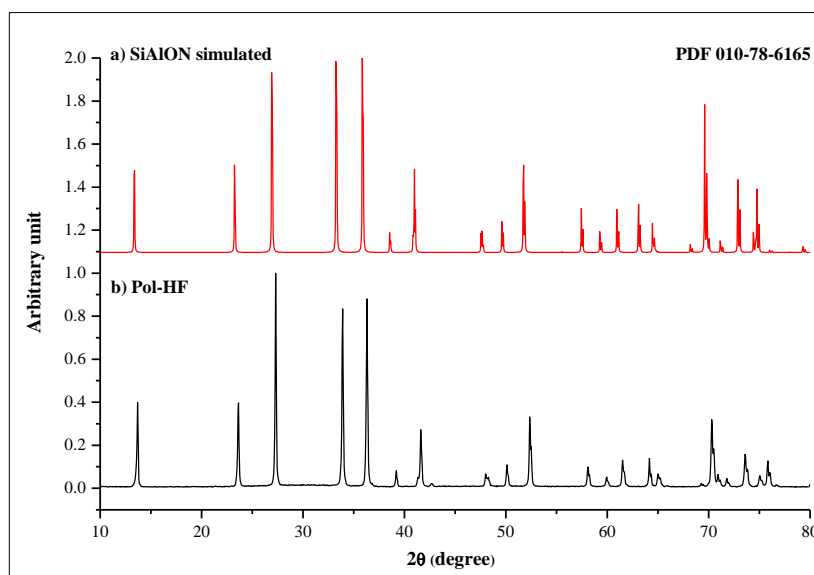


Fig. 33. XRD pattern of Pol-HF sample.

As shown in the graphs, both treatments are equal, present the same peaks position, and the well-defined sharp diffraction peaks imply that the particles have high crystallinity. Furthermore, the analyses of Figs. 32 and 33 illustrate that the two diffractions correspond to the simulated patterns of the powder diffraction file (PDF) of SiAlON (PDF 010-78-6165) and β -Si₃N₄ (PDF 000-33-1160).

The only detail that has not been identified consists of a minor peak, which presented a very low intensity, at about $2\theta = 42^\circ$, most probably due to impurities or contamination. SiAlON and β -Si₃N₄'s patterns are identical, and this re-marks again that the structure of SiAlON is isomorphous to that of β -Si₃N₄. Although these two materials have the same crystal structure, the intrinsically properties together with the atomic substitution and replacement allow the SiAlON to present itself as a resulting element with superior features to the original pure Si₃N₄ [91]. For this reason, in Fig. 33 is shown only the XRD simulated pattern of SiAlON and not that of β -Si₃N₄.

For the two remaining treatments should be given additional interpretations.

In Fig. 34 are reported the XRD measurements of Pol-N₂ and Pol-Thermally oxidized samples together with the simulated hypothetical secondary phases. The spectra are reported only in the range between 18-50° 2 θ degree, because in this area it is possible to detect the presence of additional and distinct peaks from those of the principal phase.

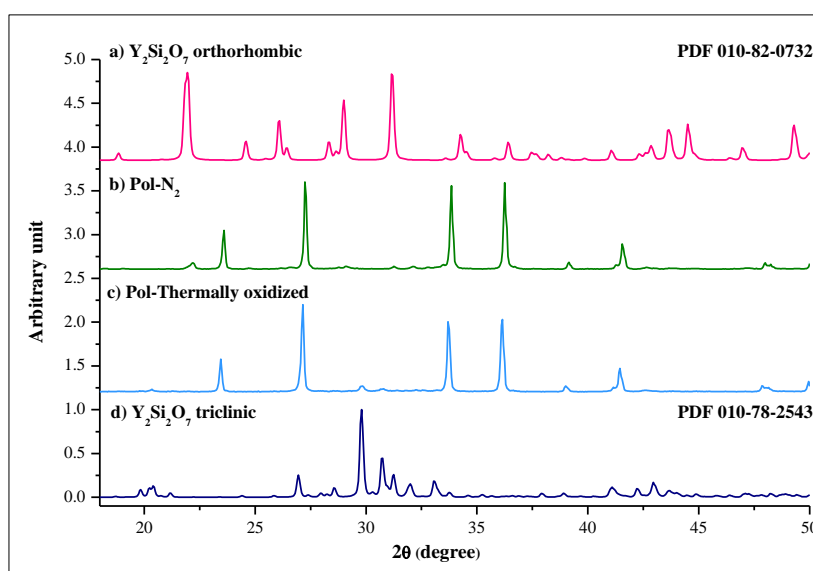


Fig. 34. XRD patterns of *polished* thermally treated samples in N₂ and in air.

Although the peaks of SiAlON continue to be present in the whole spectra, it is possible to observe additional low-intensity peaks especially in the $2\theta = 25$ - 35° range. From the comparison with the ICDD PDF-4 database, they may be explicable in the presence of different yttrium silicates on the surface layers of Pol-N₂ and Pol-Thermally oxidized. Yttrium silicates have been investigated in great detail, as they represent interesting materials not only because of their optical characteristics but also from a structural point of view. Up to now, it is known two different yttrium silicates with composition Y₂Si₂O₇

and Y_2SiO_5 , but only the first has received increased attention due to its complex polymorphism. In literature, are reported seven different modifications of this compound: α , β , γ , δ , ϵ , ζ , and η . The polymorphs differ from each other by the degree of polymerization and the arrangement of the Si-O tetrahedral and/or by the coordination number of Y. Forms β , γ , δ , ϵ , and ζ can be classified as sorosilicates, while forms α and η belongs to the group of the so-called mixed anion silicates [92, 93].

Fig. 35 shows the magnification in the $2\theta = 20-50^\circ$ range of both the spectrum of the specimen treated in N_2 and that simulated $Y_2Si_2O_7$ in orthorhombic unit cell (PDF 010-82-0732).

The symbols “♦” reported both in Figs. 35 and 36 specify the peaks of SiAlON.

The overlap of the two spectra illustrates the complex situation that is found in the study of this surface. The complete and accurate description of the numerous new diffraction

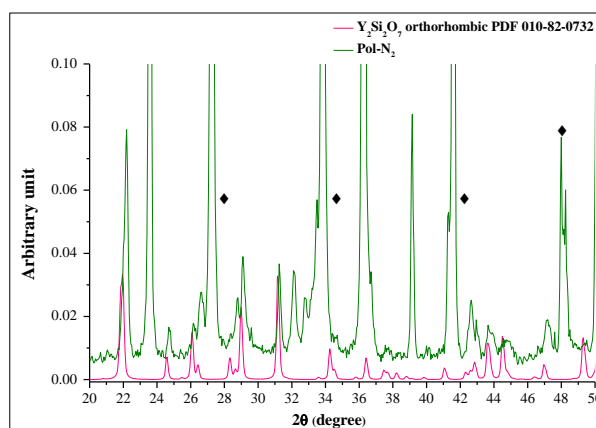


Fig. 35. XRD patterns of Pol- N_2 sample and $Y_2Si_2O_7$ in orthorhombic system.

peaks in this particular sample does not seem to be satisfied by the mere presence of the simulated spectrum of $Y_2Si_2O_7$. Probably, the XRD analyses performed on the surface of Pol- N_2 have detected the growth and formation of several forms of silicates with different stoichiometry.

Moreover, it is important to keep in mind and to underline two observations: the

first is that the formation of silicates requires oxygen to take place; the second is that this heat treatment is not carried out in the atmosphere, but conducted in the presence of nitrogen, and thus the only source of this element is the matrix of SiAlON. Therefore, this may explain the appearance of the new shifted triplet in the Pol- N_2 Raman spectrum (Fig. 30 c)), which could be attributed to a SiAlON layer with a different content of oxygen.

In the case of the sample treated in air (Fig. 36), the XRD in the $2\theta = 18-40^\circ$ range evidence some new peaks especially in regions $2\theta = 19^\circ-21^\circ$ and $2\theta = 29^\circ-33^\circ$, which are associated more likely to the secondary phase of α - $Y_2Si_2O_7$ in triclinic unit cell (PDF 010-78-2543).

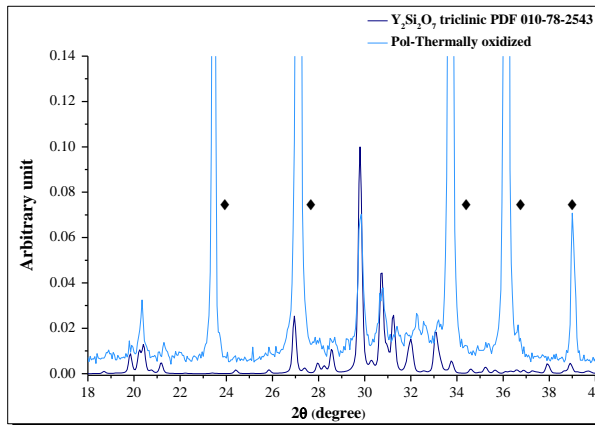


Fig. 36. XRD patterns of Pol-Thermally oxidized sample and $Y_2Si_2O_7$ in triclinic system.

The general trend of the spectrum of Pol-Thermally oxidized seems to be also less complex compared to the previous. Moreover, the position of the peaks of the simulated spectrum of $Y_2Si_2O_7$ in triclinic system gives a good explanation to the appearance of new diffraction peaks in the analyzed sample. It is probably due to the fact that the treatment in air has the possibility of

having a greater and easier availability of oxygen from the atmosphere. This does not alter the surface layer of sample, because the triplet bands representing the matrix do not change position and not present broadening, just as highlighted by the Raman spectrum reported in Fig. 30 d). However, the appearance of the background could be related to the growth of the new phase of α - $Y_2Si_2O_7$.

To conclude the XRD data presentation and discussion, in Fig. 37 are graphically summarized all previous observations.

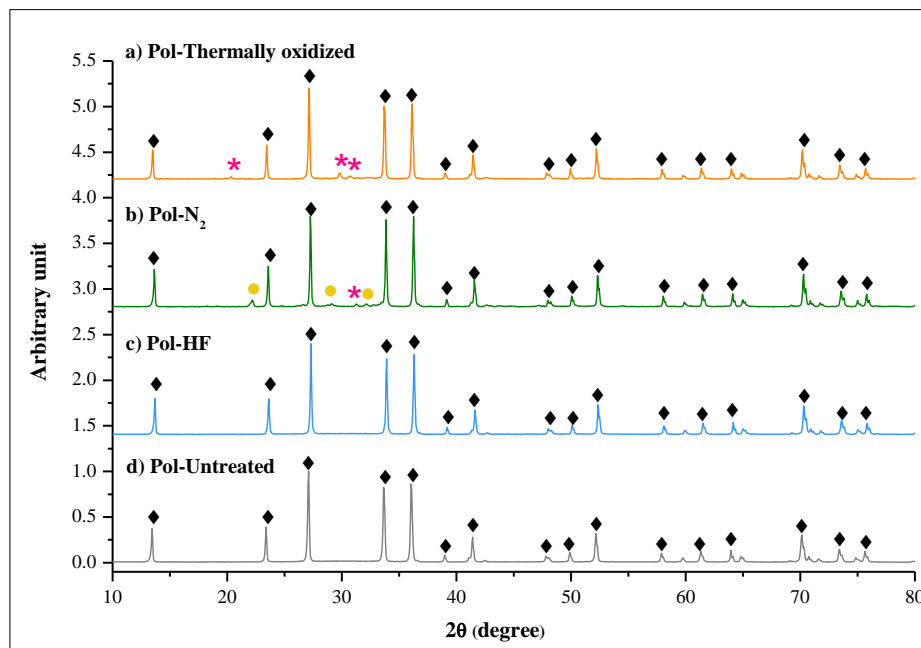


Fig. 37. Phase identification in all β - Si_3N_4 samples in XRD patterns.

◆ = SiAlON; ● = $Y_2Si_2O_7$ triclinic; * = $Y_2Si_2O_7$ orthorhombic.

Microstructural characterizations of Si_3N_4 surface preparations are conducted using scanning electron microscope (SEM) and energy dispersive X-ray microanalysis (EDX). The latter is a non-destructive and very fast technique, which exploits the emission of X-rays of specific wavelength. It allows the semi-quantitative characterization of solid substances and their elemental analysis.

Firstly will be consider the investigations of the surface morphology and microanalyses of the Pol-Untreated and Pol-HF samples (Fig. 38 a) and b)); secondly will be describe the Pol- N_2 and Pol-Thermally oxidized biomaterials (Fig. 41 c) and d)).

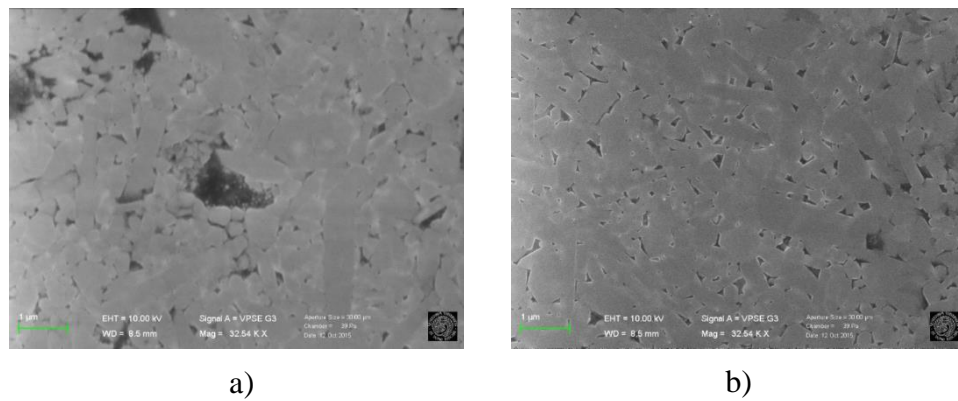


Fig. 38. Electron photomicrographs of surface preparations: a) Pol-Untreated and b) Pol-HF.

As evidenced in images, the sample's surfaces of Pol-Untreated (Fig. 38 a)) exhibits the classic microstructure with large elongated $\beta\text{-Si}_3\text{N}_4$ grains, which have a length of about 2-3 μm . Furthermore, when the untreated material is etched in HF (Fig. 38 b)), both the resulting surface and the overall topography show many characteristics similar to the Pol-Untreated case, with the exception of etching damage at the tips of the protruding grains. The magnifications at 200 nm of both samples are reported in Fig. 39.

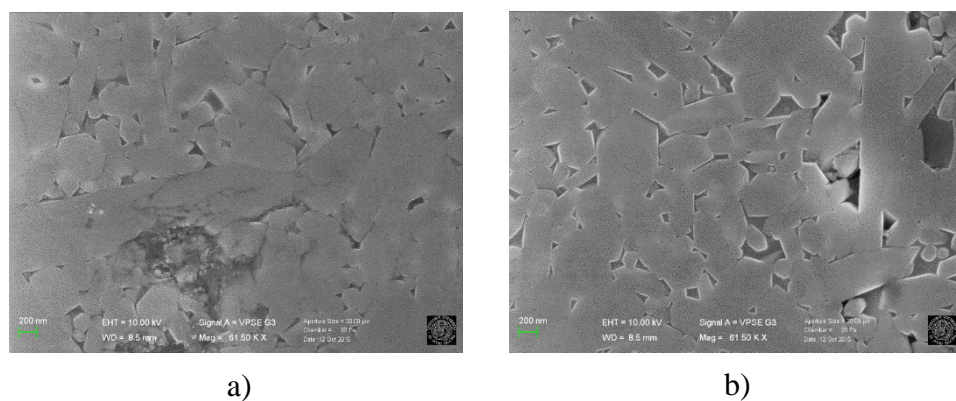


Fig. 39. SEM magnification on: a) Pol-Untreated and b) Pol-HF surface.

In the previously XRD analyses, it has been stated that Pol-Untreated and Pol-HF contain only the SiAlON phase. This statement is also confirmed by EDX, as shown in Fig. 40 a) and b).

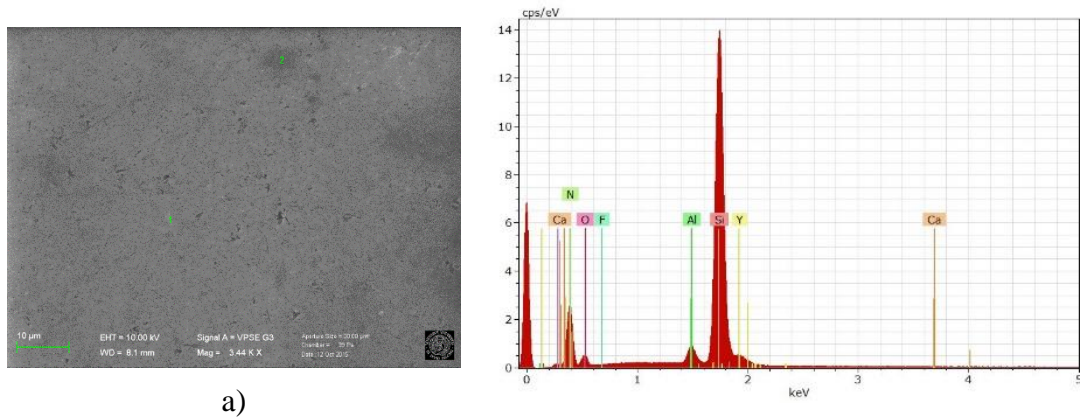


Fig. 40 a. Result of EDX performed on Pol-Untreated.

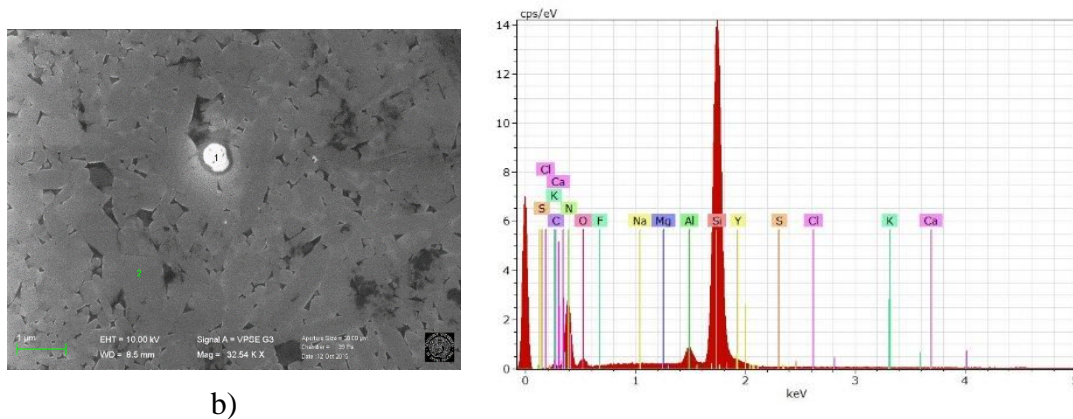


Fig. 40 b. Result of EDX performed on Pol-HF.

The comparison of the spectra of SiAlON matrix emphasizes the fact that the two samples have the same trend and almost the same absolute intensity of the coupled band Si-Y and N-O. This confirms the hypotheses know until now.

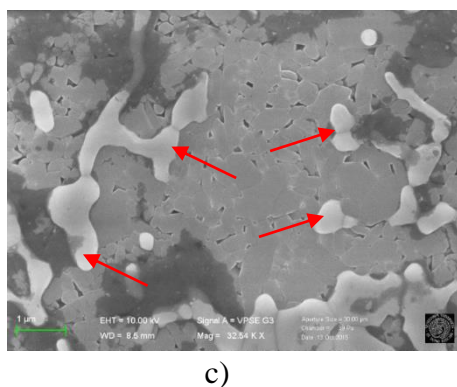


Fig. 41 c. Electron photomicrograph of Pol-N₂ surface preparation.

The morphology of the surface that has undergone the heat treatment in N₂ shown in Fig. 41 c) appears very similar to Pol-Untreated sample, because it is still possible to observe its classic texture. Anyway, it is evident the presence of both new visible white particulates (indicated by red arrows), and elongated crystalline forms (clearly visible in next Fig. 42) that cover the surface.

Also in this case, the use of microanalysis (Fig. 42) permits a better and thorough analysis of the surface's evolution after polishing and N₂-heat treatment.

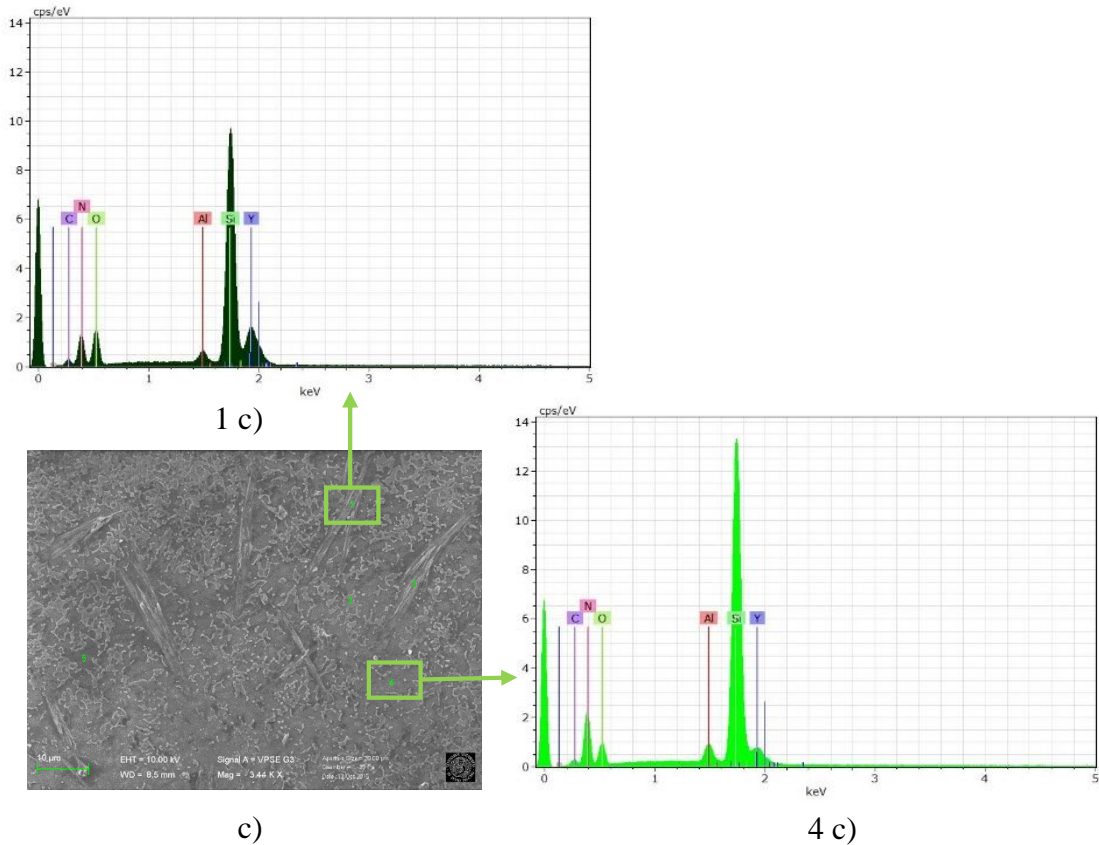
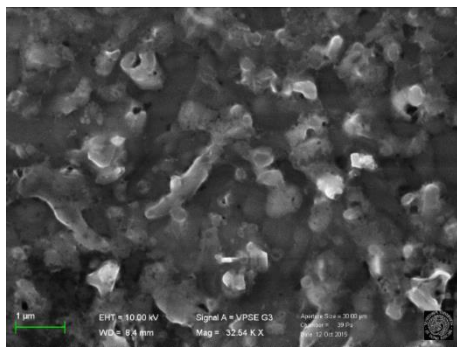


Fig. 42. Results of EDX performed on Pol-N₂.

As inferred from the observation of the graphs, when analyzing the elongated crystalline forms (1 c)) and the particulates (omitted here) the intensity of the peaks of Si and N decrease considerably, while that of the peaks of Y and O increase. When, instead, is studying the matrix (4c)) the resulting graph returns to show the same trend as those seen



d)

Fig. 41 d. Electron photomicrograph of Pol-Thermally oxidized surface preparation.

for Pol-Untreated and Pol-HF. This could be explained by associating the growth of crystals on the surface with the formation of yttrium silicates with different stoichiometry, which requires the loss of oxygen from the silicon and the reorganization of matrix's bond.

Finally, specimen subjected to the oxidation treatment (Fig. 41d)) exhibits a very different microstructure and it shows the formation of a new

compound, which covers and spans the grains, traced to α - $\text{Y}_2\text{Si}_2\text{O}_7$ by XRD measurements.

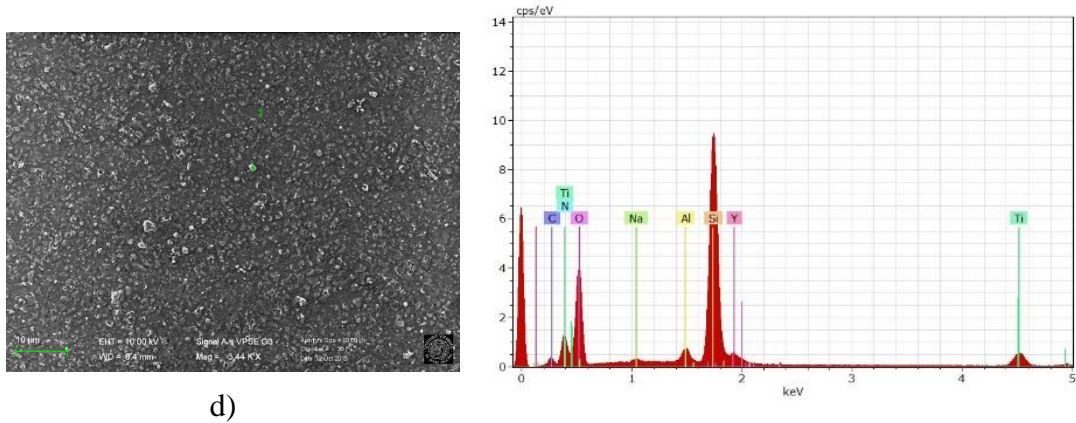


Fig. 43. Result of EDX performed on Pol-Thermally oxidized.

The microanalysis conducted on this bioceramic and illustrated in Fig. 43 underlines that the surface is very rich in O than N, as demonstrated by the inversion of the intensity ratio of their peaks.

To conclude the study of Pol-Thermally oxidized sample, in Fig. 44 is shown its Raman spectrum in the complete wavenumber region ($142\text{-}764\text{ cm}^{-1}$), and are also reported its characteristic features.

However, it is possible to observe that its trend is completely changed and appear additional peaks in the regions $253\text{-}433\text{ cm}^{-1}$ and $643\text{-}713\text{ cm}^{-1}$.

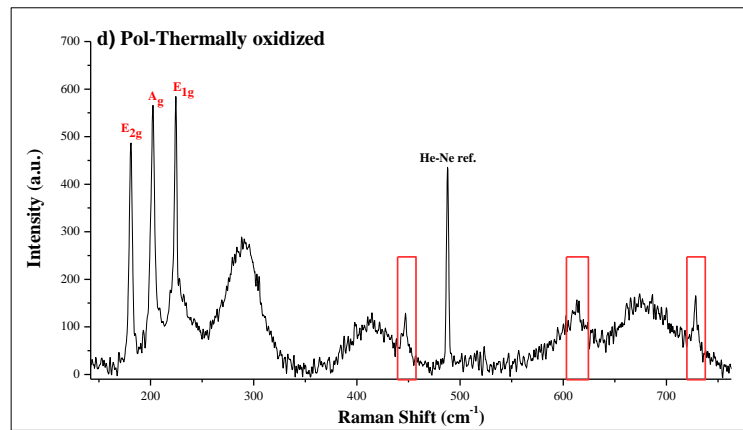


Fig. 44. Raman spectrum in the wavenumber region $142\text{-}764\text{ cm}^{-1}$ of Pol-Thermally oxidized sample. It is still possible to see the three intense bands (E_{2g} , A_g , E_{1g}), the signal of He-Ne lamp, and three typical band of the material highlighted by red rectangles.

As the previous analyses with XRD, SEM and EDX have all been shown the growth and the presence of a layer of α - $Y_2Si_2O_7$, looking in literature it was possible to find the Raman spectra of all the seven different forms of this silicate.

Observing Fig. 45, which shows the spectrum of α - $Y_2Si_2O_7$, it is possible to assume that

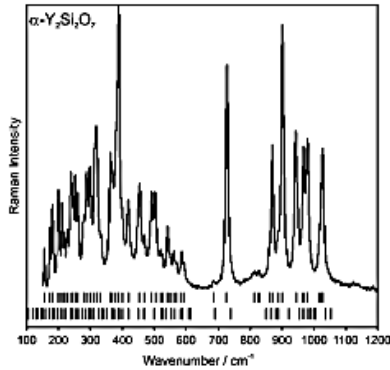


Fig. 45. Raman spectrum of α - $Y_2Si_2O_7$.

the additional bands appear in the spectrum of Pol-Thermally oxidized sample may be explicable to those of the α -phase.

The similarity between the spectrum obtained experimentally and the α one found in literature is remarkable, although in the first are not present two sharp and intense bands located at 388 cm^{-1} (Y-Si-O bending mode) and 728 cm^{-1} (Si-O-Si bending mode), and the peaks are not very distinguishable from each other.

To conclude this discourse, in Fig. 46 a) and b) are schematically depicted the modification induced by the thermal treatments, who have been given a greater interest throughout the handling of data.

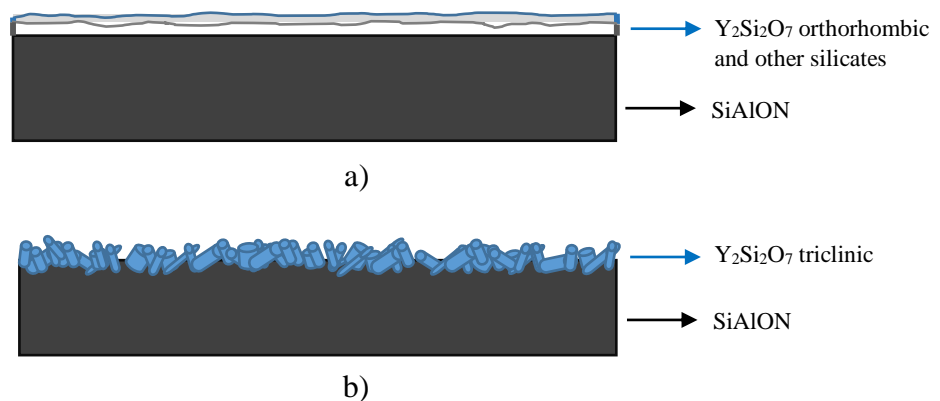


Fig. 46. Surface schematic representation of: a) Pol- N_2 and b) Pol-Thermally oxidized.

In summary, XRD data, SEM micrographs and EDX microanalyses have been used to contribute for the characterization of the superficial behavior of Si_3N_4 ceramics. These analyses confirmed the existence of marked differences between the manufacturing processes, particularly between samples subjected to the same thermal treatment, already identified by Raman spectroscopy and laser scanning microscope.

5.2 Interaction of bacteria and Si₃N₄ surface

5.2.1 Labeling the Raman spectra of bacterial strains

In this study, the Raman spectroscopic technique is not only used to characterize the different surfaces of Si₃N₄, but has also been employed to study the cellular compositions and the changes of the metabolism of three bacteria, *P. gingivalis*, *T. denticola* and *T. forsythia*, when they are in contact with this material. These microorganisms belong to an important cluster, called “red complex”, and, as described in the introductory part, are responsible for periodontal diseases.

In Fig. 47 are shown averaged Raman spectra collected on living bacterial cells before exposure to Si₃N₄ surfaces.

The total spectral region monitored, which lies between 600 and 1800 cm⁻¹, is characterized by numerous vibrational bands typical of the four classes of macromolecules: nucleic acids, proteins, lipids and carbohydrates.

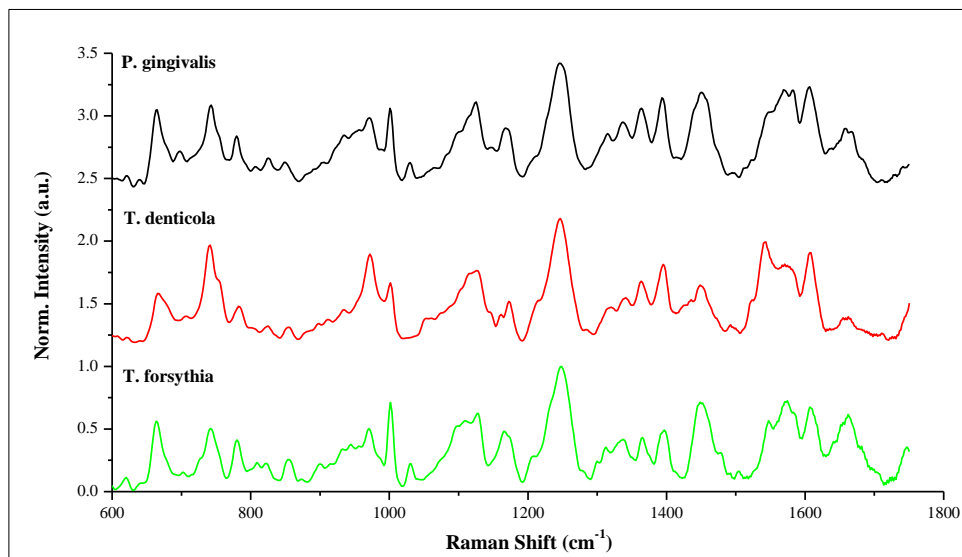


Fig. 47. Averaged Raman spectra of red complex's components.

Although the bacteria have unique features in their species, the three representative spectra are very similar to each other. The most obvious exceptions are related to the absence of the peak located at about 1030 cm⁻¹ in the bacterium *T. denticola*, to the presence of a double peak located at about 1568 and 1582 cm⁻¹ in *P. gingivalis*, besides the fact that the peaks present different intensity values.

An evidence of successful acquisition of bacteria's spectra is reported in Fig. 48.

The comparison of Raman data allows to notice some remarkable similarities between the peaks of *P. gingivalis* obtained experimentally, shown in Fig. 48 a), and others of main biopolymers reported in literature, shown in Fig. 48 b) [89].

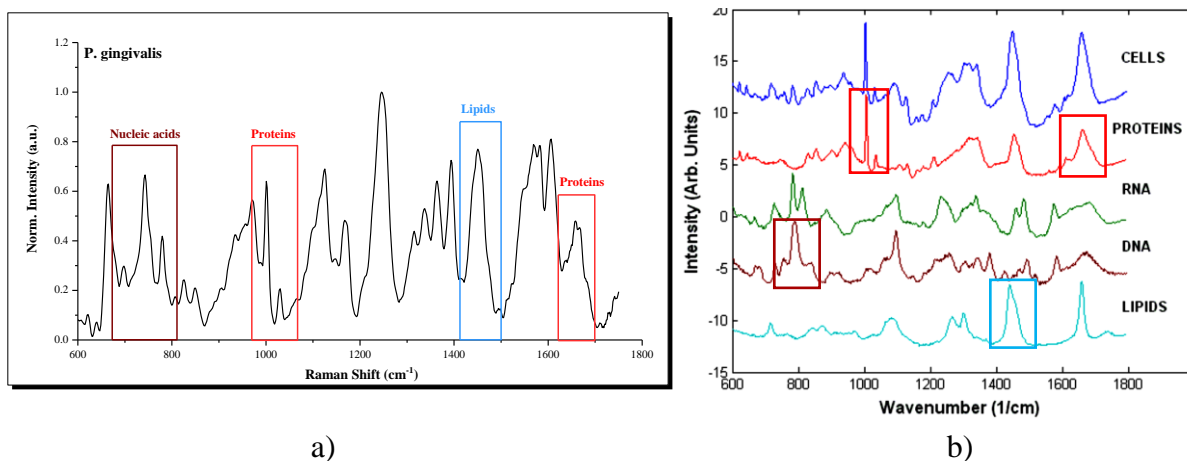


Fig. 48. a) Average spectra of *P. gingivalis* and b) typical spectrum of macromolecules found in cells.

In both images is possible to see the vibrational peaks corresponding to nucleic acids (identified by burgundy rectangle), proteins (detected by red rectangle) and lipids (observed by blue rectangle).

The three spectra reported in Fig. 47 can also be divided into IV zones from lower toward higher frequencies. As an example of such partition is taken again the Raman spectrum of *P. gingivalis* (Fig. 49), as is considered the representative strain and the most pathogenic of this complex. All peaks, in addition, have been numbered to facilitate the identification of the bands and the comparison between the spectra. Moreover, the spectral location of all bands and their tentative assignment are reported in Table 11.

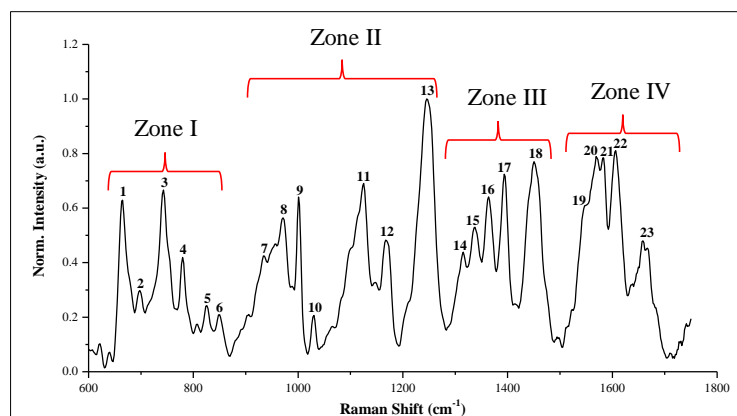


Fig. 49. Main peaks identification in *P. gingivalis* spectrum.

Table 11. Peaks assignment for bacterial Raman spectra [94].

Label	Spectral location (cm ⁻¹)	Assignment			
		Nucleic Acids	Proteins	Lipids	Carbohydrates
1	664	T, G ring	v(C-S) of cysteine		
2	694		v(C-S) of methionine		
3	743	T ring br mode			
4	780	C, T based ring br mode in DNA			
5	821	v(O-P-O)			
6	850	Single bond v vibrations			
7	936		v(C-C) of proline and valine		
8	971		Phosphate monoester group	=CH bend	
9	1000/2		Sym ring br Phe		
10	1030		C-H in-plane Phe		
11	1125		v(C-N)	v(C-C) skeletal of acyl bk (trans conformation)	
12	1167		C-H in-plane bend Tyr	v(C-C)	
13	1245		v(C-N) Amide III		
14	1315	G		CH ₃ CH ₂ tw mode	
15	1337/9		Trp	CH ₂ /CH ₃ wag, tw and/or bend mode	
16	1364	G	Trp		
17	1394/8	sym v(C-O) in COO ⁻ groups			CH ₂ def
18	1450		CH ₂ bend	CH def	CH def
19	1543		Amide II		
20	1568		Amide II		
21	1582	A, G	Phe		
22	1607		C=C Phe		
23	1658/65		Amide I (α -helix and β -sheet)		

Abbreviations: A = adenine; T = thymine; C = cytosine; G = guanine; Phe = phenylalanine; Ty r= tyrosine; Trp = tryptophan; v = stretching; br = breathing; bk = backbone; def = deformation; bend = bending; tw = twisting; wag = wagging; sym = symmetric.

Most bands correspond to functional groups in the main constituents of a microbial cells, proteins, carbohydrates, lipids and nucleic acids. Some are more specific for smaller molecular compounds, like very characteristic sharp band of phenylalanine at about 1001 cm^{-1} . So, the obtained Raman spectra contain multidimensional information on the presence and relative abundance of all major cellular compounds, without adding any chemical reagents to mark specifically these components. Obviously, in a complex multicomponent system such as a bacterial cell, peaks attributions remained somewhat a tentative.

Analyzing Zone I, the low-frequency side of Raman region between 600 and 900 cm^{-1} , is possible to observe that bands relating to nucleic acids mainly dominate this left zone, and DNA can be identified by Raman bands characteristic of nucleotide and sugar-phosphate backbone vibrations. This spectral range includes one main band at lower frequencies at about 664 cm^{-1} (labeled as band 1) and a less intense peak at 694 cm^{-1} (band 2), which could be related to the C-S stretching mode of cysteine in DNA structure and to thymine and guanine ring, and to a C-S stretching trans in amino acid methionine, respectively. A quadruplet also appears at 743 , 780 , 821 and 850 cm^{-1} , which are assigned to thymine and cytosine ring breathing mode (bands 3 and 4, respectively), $\text{C}_5'\text{-O-P-O-C}_3'$ stretching mode (band 5), and to single bond stretching vibrations for amino acids (band 6).

Also the successive region between 936 and 1245 cm^{-1} , designated as Zone II, includes important spectral features related, however, to proteins bands. Peaks located at 934 cm^{-1} (band 7) and 972 cm^{-1} (band 8) representing C-C backbone stretching mode of proline and valine in α -helix conformation, and the phosphate monoester groups of phosphorylated proteins, respectively. The sharp and intense band at around 1001 cm^{-1} (band 9) arises from symmetric aromatic ring breathing mode of phenylalanine (Phe). Even the peak at 1030 cm^{-1} (band 10), that is absent in *T. denticola* spectrum, is referred to C-H in plane bending mode of this important amino acid. The doublet at 1125 (band 11) and 1167 cm^{-1} (band 12) belongs the first both to C-C skeletal stretching of acyl backbone in lipids (trans conformation) and C-N stretching vibration mode of proteins, and the second to C-H in-plane bending mode of tyrosine, respectively. Finally, the strong band positioned at 1245 cm^{-1} (band 13) originates from C-N stretching mode of Amide III. This peak was used to normalize to 1 all bacteria spectra.

Zone III corresponds to the range 1316 - 1450 cm^{-1} . The Raman emission at a frequency of 1315 cm^{-1} (band 14) is assigned to guanine and CH_3CH_2 twisting mode in lipids, while that of 1337 cm^{-1} (band 15) to tryptophan and CH_2/CH_3 wagging, twisting and/or bending mode

of lipids. The two neighbours bands at 1364 cm^{-1} and 1395 cm^{-1} (band 16 and 17) represent amino acid tryptophan, symmetric C-O stretching in carboxylate COO^- groups, and CH_2 deformation in carbohydrates, respectively. Band 18 at 1450 cm^{-1} belongs both to CH_2 bending mode of protein and C-H deformation mode of lipids and carbohydrates.

Finally, in the right side of spectrum is positioned the high-frequency region between 1543 and 1665 cm^{-1} , indicated as Zone IV. Amide II and Amide I, identified by the peaks 1543 cm^{-1} , 1568 cm^{-1} , and the range $1658\text{-}1665\text{ cm}^{-1}$ (band 19, 20, and 23, respectively) dominate this spectral area. But, two further bands are found at 1582 (band 21) and 1607 cm^{-1} (band 22). The first represents Phe and the nucleotides adenine (A) and guanine (G), while the second the C=C bending in Phe.

5.2.2 Monitoring bacteria metabolism by Raman spectroscopy

From the experimental results obtained analyzing the spectra of healthy bacteria, it is possible to postulate that Raman technique can be also used to identify metabolic changes that microorganisms experience during their interaction with the Si_3N_4 biomaterial surface. This hypothesis is substantiated by numerous data of previous literature works [95-97]. Tang et al. [95] applied Raman microspectroscopy to discriminate mycobacteria and Gram-negative bacteria on the basis of their different biochemical components and on the presence or absence of various Raman peaks. Instead, Moritz et al. [96] and Jung et al. [97] analyzed the effect of antibiotic agents on the biofilms of *Escherichia coli* and *Pseudomonas aeruginosa* by Raman spectroscopy, and both the studies described the metabolic changes experience by those bacteria during exposure to different treatments through spectral variations.

It is important to underline that to date has been given much more attention to the investigation of therapeutic effects of antimicrobial agents (as antibiotics, drugs or toxins) with different bacterial strains, underestimating the importance of the study and comprehension of the direct contact between bacteria and biomaterials. From this point of view, the present analysis aims to investigate this interaction, placing itself in an innovative way in the scientific field.

This section will be treated the comparison between the spectra of healthy bacterial strains with the Untreated surface to identify the main spectral differences. Both surface morphologies, *as fired* and *polished*, will be considered.

As the number of bands to evaluate in the 600-1800 cm^{-1} spectral region is very high, four main peaks are selected:

1. 780 cm^{-1} (band 4) belonging to Zone I
2. 1001 cm^{-1} (band 9) belonging to Zone II
3. 1450 cm^{-1} (band 18) belonging to Zone III
4. range 1658-1665 cm^{-1} (band 23) belonging to Zone IV

The choice is made on the basis of the pronounced changes in intensity of this bands.

- *Porphyromonas gingivalis*

Fig. 50 compares the living cells of *P. gingivalis* with its cells after the exposition and the interaction with Si_3N_4 Untreated surface.

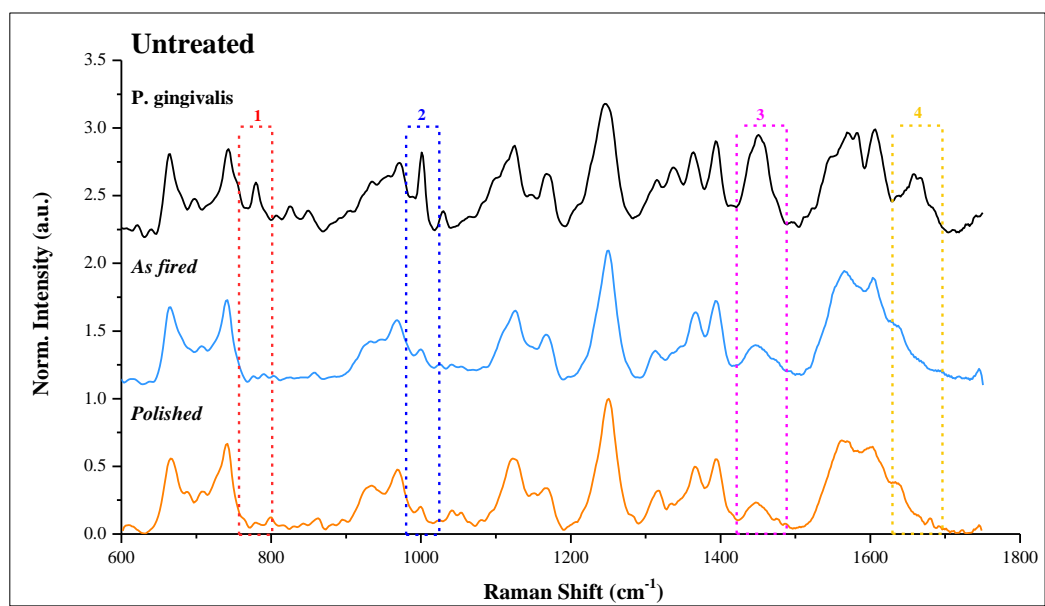


Fig. 50. Raman spectra comparison between *P. gingivalis* and Untreated samples.

The striking variations of selected bands can be listed, as follows:

1. In Zone I, band 4 positioned at 780 cm^{-1} is very intense when the bacterial cells are metabolically active, while is conspicuously lowered and almost disappeared when cells are decaying. This band represents in fact ring vibrations of DNA corresponding to cytosine (C) and thymine (T) that are the pyrimidine bases and has been reported to be very sensitive to cell death. In particular, its accentuate decrease indicates the breaking of the chemical bond between the nitrogen bases of

DNA (A-T and C-G), and then the disintegration of the deoxyribonucleic acid strands. In this area, it would be important to highlight the presence of an additional peak located at 664 cm^{-1} (band 1). It is labeled in Fig. 51 as “**” and represents the C-S stretching mode of cysteine in DNA structure.

Cysteine plays a fundamental role in cross-linking proteins, thus supporting their tertiary structure and increasing their rigidity. In this microorganism, the Raman C-S band in both surface morphologies remained apparently insensitive to the exposure to a Si_3N_4 surface. In other words, the direct contact with the biomaterial does not affect the tertiary structure of the DNA “stair”, but damaged the individual A-T and C-G “steps”, namely the primary structure of individual nucleotides.

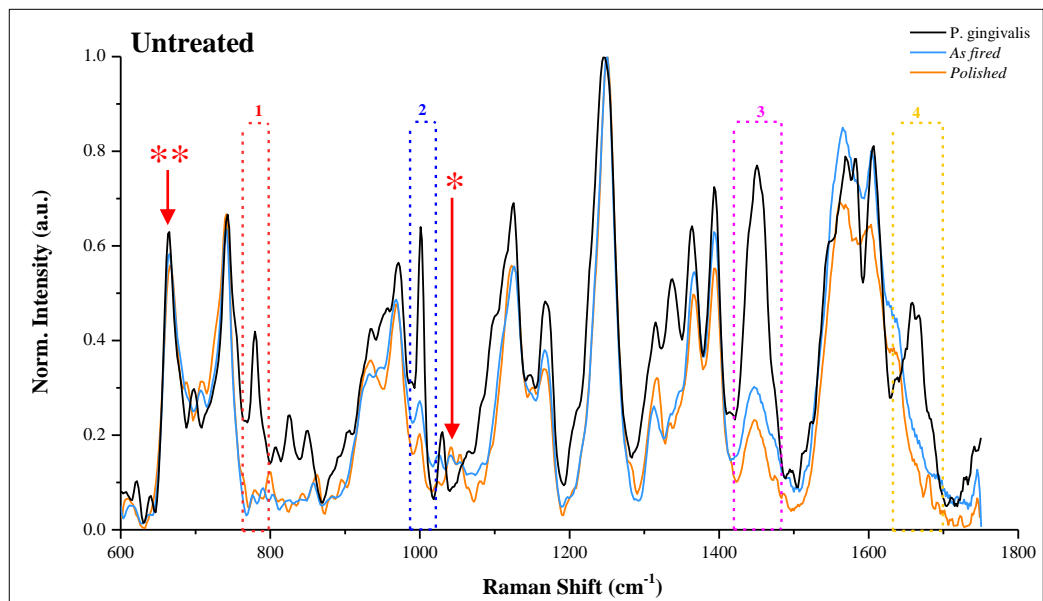


Fig. 51. Overlapping of Raman spectra of *P. gingivalis*, *as fired* and *polished* Untreated samples.

2. In Zone II, band 9 at 1001 cm^{-1} , assigned to the breathing mode of Phe, became significantly weaker after the exposure to the Untreated Si_3N_4 surface. This protein is considered a key element for the metabolism and growth of bacterium, as it is the basis for the phenylacetic acid production, which is one of the major fermentation products of *P. gingivalis* [98]. Moreover, Phe is an aromatic and hydrophobic residue highly conserved in the last ten amino acid residues of the carboxy-terminus of outer membrane proteins of most Gram-negative bacteria. Its conserved presence in position 1 suggesting an important function of this amino acid in OM localization and an essential role in assembly the protein into the OM

[99, 100]. Taking as a reference the spectrum of bacteria in their living state, the Phe metabolic activity of *P. gingivalis* on the Untreated Si₃N₄ surface became very low.

Another striking feature found in Zone II is the appearance of a new Raman band at 1044 cm⁻¹, labeled as “*” in Fig. 51. This band is assigned to the *cis* conformation of peroxyxynitrite (NO₃⁻) and it belongs to a spectral area in which no overlap occurs with Raman bands intrinsic to the constituent molecules of *P. gingivalis* cells. The peroxyxynitrite anion (O=N-O-O⁻) is a strong oxidant and a particularly toxic substance for a number of bacteria, which forms from the reaction between superoxide and nitric acid. The O=N-O-O⁻ anion is capable to quickly get across cell membranes through anion channels and to directly react with lipids, DNA, and proteins through oxidative reactions. These reactions in turn trigger drastic cellular responses that include oxidative injury and bacterial necrosis.

3. In Zone III, a drastic reduction in intensity is noticed for band 18 settled in 1450 cm⁻¹. Mainly related to the CH₂ bending mode of protein and C-H deformation mode of lipids and carbohydrates, this band is an important probe of cell viability. If its intensity decreases drastically due to the interaction with the Si₃N₄ surface, this is because all components of the cellular envelope are damaged.

Probably, the first to be degraded are the double concentric lipid membrane layers (OM and IM) that surround and protect the cell, followed by carbohydrates and proteins, which denatured or unfolded, and lose their higher-order structure. The presence of these elements are essential for the proper cellular biochemistry, because they play the role of receptors, control the transport systems of nutrients and waste products, participate in energy production, lipid biosynthesis, and secretion and transport of proteins.

The appearance of the new peak at about 1044 cm⁻¹ can be directly connected with the conspicuously degradation of this band. A major aspect of peroxyxynitrite-dependent cytotoxicity relies on its ability to trigger lipid peroxidation in membranes, liposomes, and lipoproteins by abstracting a hydrogen atom from polyunsaturated fatty acids. The products of such reactions include lipid hydroperoxyradicals, conjugated dienes, and aldehydes. A chain-reaction then propagates free radical and the degeneration of membrane lipids, causing membrane permeability and fluidity changes with drastic biological consequences.

4. The analysis of the last band in Zone IV numbered as 23 is strongly connected to the above description. It can be assigned to Amide I in both α -helix and β -sheet and also this peak is relevant to the metabolic activity of *P. gingivalis*. The Amide I band can be defined as “the spectroscopic signature of life” and its intensity depends on the nutrient conditions of the bacteria, the stronger the band the higher their metabolic activities.

Moreover, in previous works found in literature is reported that Amide I could be involved in chemical and structural composition of lipid A, because it intervenes in the fatty acid linkage of lipid chains as amide-linked acyl group. Lipid A has received worldwide scientific attention, and in 1957, it was postulated to constitute the endotoxic center and immunomodulating principle of LPS. This element is in fact responsible for the toxicity of Gram-negative bacteria [101, 102].

A comparison between spectra from living and exposed bacteria on the Untreated sample showed the complete disappearance of the Amide I, which marks the disappearance of the β -sheet structure as a consequence of bacteria/ Si_3N_4 -surface interactions.

Finally, observing Fig. 51 it is possible to assert that the *polished* morphology shows a slightly more decrease of peaks than the *as fired*, although this observation derives from simple qualitative observation of the image.

- *Treponema denticola*

T. denticola is the most controversial bacterium of the complex. It is very strange because is evolutionarily quite distinct from both Gram-negative and Gram-positive eubacteria, but in the same time it presents characteristics of both species.

Moreover, only in recent years with the development of continuous culture it has been possible to obtain more information on this microorganism, because it was very difficult to grow its bacterial cells on the surface of agar plates using standard methods.

Its highly unique feature and its contrasting behavior are emphasized by Raman spectra, as shown in Fig. 52 and 53.

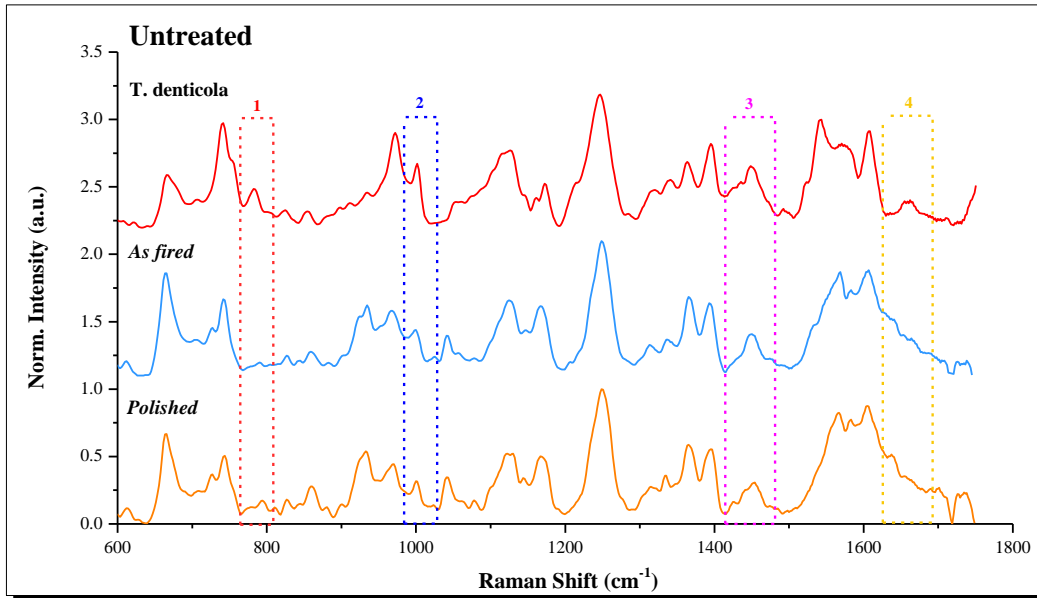


Fig. 52. Raman spectra comparison between *T. denticola* and Untreated samples.

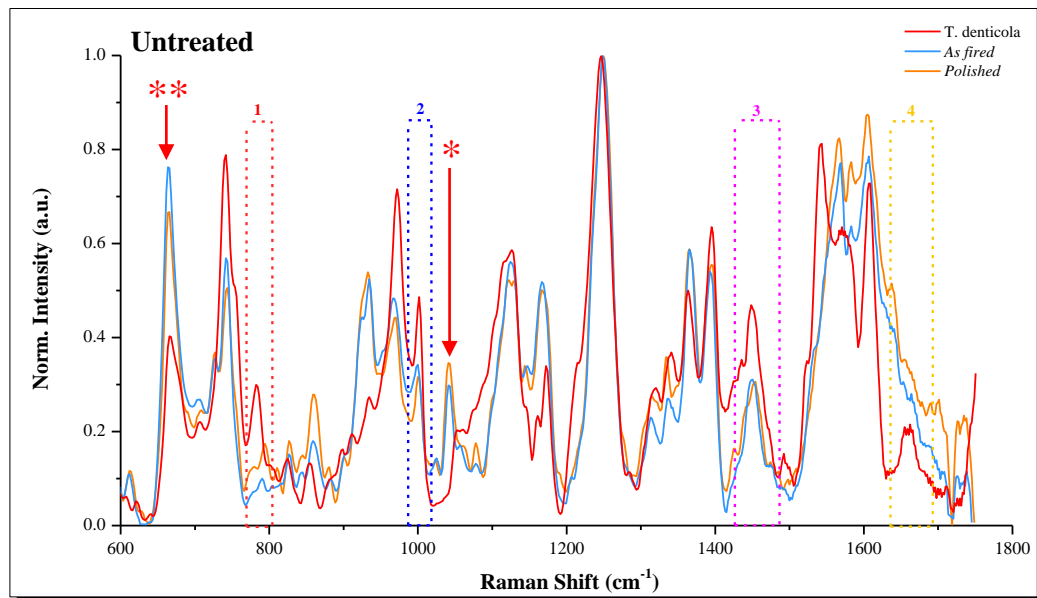


Fig. 53. Overlapping of Raman spectra of *T. denticola*, *as fired* and *polished* Untreated samples.

Both images allow to appreciate the main differences between the selected bands of this microorganism and the one described above, which may be submitted following the same order as before:

1. In Zone I, both the intensity and degradation of band 4, which represents the vibration of pyrimidine nitrogen bases of DNA, seem much less intense and marked than the spectrum of *P. gingivalis*. Furthermore, the peak located at 664 cm^{-1} (band

- 1) labeled as “**” increases considerably in intensity in both morphologies surfaces. The answer to both these observations may lie right on the complexity of the cellular structure and envelope of this strain.
2. The same statement can be made for the peak of Phe (band 9) in Zone II, which intensity is reduced only in slightly way. In the case of *T. denticola*, the amino acid Phe is localized in the structural composition of propyl-phenylalanine-specific serine protease, also called dentilisin or chymotrypsin-like protease. This is a major extracellular protease and pathogenic factor produced by this microorganism, and also in this case the aromatic residue is localized in position 1 [103]. The reduction of Phe peak can mean both the loss of activity and dissociation of the enzyme, but also the loss of the physiology of the bacterium and its failure to adhere to the Untreated Si_3N_4 surfaces. Moreover, in this region appearances the new, sharp and very evident peak at 1044 cm^{-1} , indicated in Fig. 53 with “**”. The presence of this band thus leads to think that this bacterium has experienced damage when put into contact with the material, even if the spectra do not detect a drastic reduction of selected bands like *P. gingivalis*.
3. Also band 18 located to 1450 cm^{-1} in Zone III has a lower intensity in comparison to that of *P. gingivalis*, but in this case the degradation would appear to be more marked than the other peaks. This means that the three classes of macromolecules (lipids, carbohydrates and proteins) experience a degradation upon contact with the two different surfaces of Si_3N_4 biomaterial. Besides, this could be connected with the appearance of the new peak, which is a toxic substance (NO_3^-) for bacterial cell.
4. The last band to be analyzed is the number 23. It is placed in Zone IV between $1658\text{-}1665\text{ cm}^{-1}$ range and is related to Amide I. The behavior of this band is even stranger because the intensity of both material's peaks do not decrease but increase. In the discussion above it has been described the involvement of Amide I in the composition of Lipid A, a constituent of LPS. But, the OM of *T. denticola* has fatty acyl chain composition similar to the external layer of Gram-positive bacteria containing LPA, and at the same time it is similar to Gram-negative microorganism for the function of LPS [70]. So, this particular attitude of peaks can be explained again by the complexity and uniqueness of bacterium's structure.

Raman analyses have allowed the study of the biochemistry of *T. denticola* and highlighted the unique nature of this particular strain, adding useful information for its better knowledge.

Lastly, it is quite difficult to say in this case which surface morphology experiences a greater degradation or a possible antibacterial activity.

- *Tannerella forsythia*

T. forsythia is a Gram-negative bacterium that possesses a so far unique cell surface architecture in comparison with other S-layer-carrying bacteria. It is the only known Gram-negative species that is covered with a glycosylated SL, with, again uniquely, two SL glycoproteins simultaneously present.

But, a lot of knowledge on this organism remains to be determined and clarified, because of its unique growth requirements and the fact that it is a somewhat difficult to grow.

Raman spectra of this particular microorganism are shown in Fig. 54 and 55.

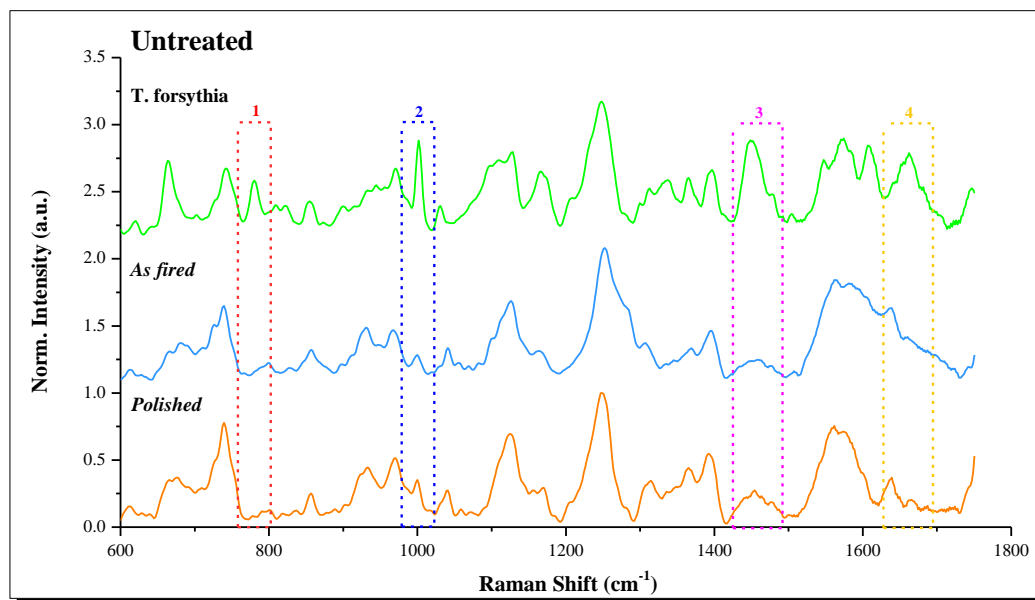


Fig. 54. Raman spectra comparison between *T. forsythia* and Untreated samples.

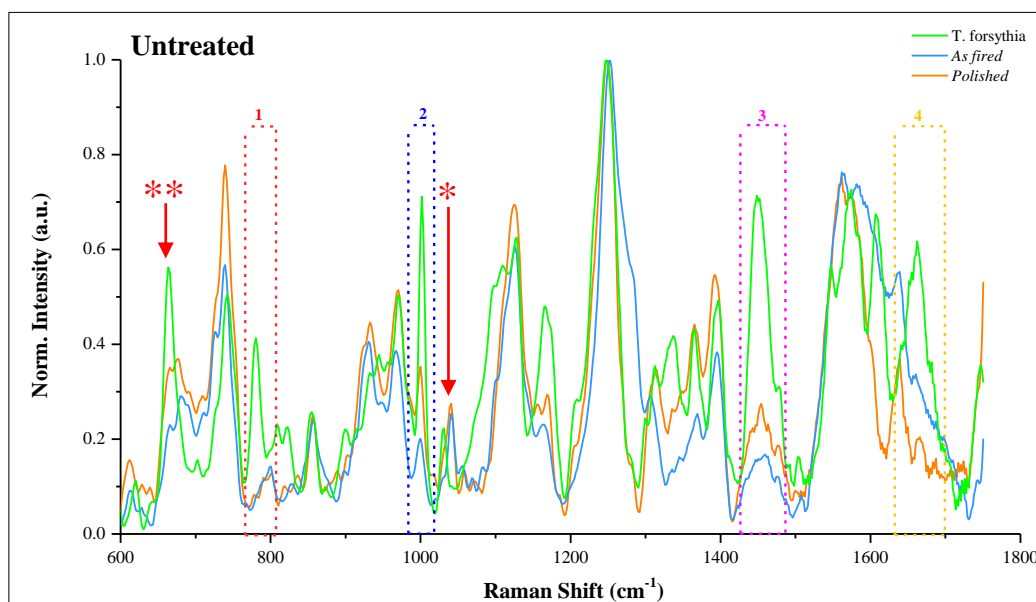


Fig. 55. Overlapping of Raman spectra of *T. forsythia*, *as fired* and *polished* Untreated samples.

1. In Zone I, band 4 at 780 cm^{-1} is conspicuously lowered when the bacterial cells are in contact with the surfaces. Moreover, it is interesting to observe that for the first time also the intensity of the band at 664 cm^{-1} (band 1, labeled as “**”) decreases considerably, indicating both the degradation of the DNA structure that the loss of tertiary and quaternary structures of the proteins, from which depends their biological action.
2. In Zone II, the Phe band numbered as 9 at 1001 cm^{-1} experiences a significantly decrease. In *T. forsythia* is possible to identify the presence of this amino acid in the conserved C-terminal domain of C-terminal region of BspA, acronym of Bacteroides surface protein. BspA is involved in secretion and trafficking of bacterial proteins to the OM even if recently a proteomic study has shown that this protein is also in turn associated with the OM fraction [104].
The degradation of Phe would result in a loss of functionality of this system, which would interrupt the secretion and the supplying of the protein portion to the OM.
3. Also in Zone III is noticed a quite drastic reduction in intensity for band 18 positioned at 1450 cm^{-1} . The OM composed of lipids, proteins and carbohydrates and responsible for communication and contact with the external environment in contact with the biomaterials has lost its functionality and caused the cellular death.

In particular, the degradation of proteins will be considered more in detail in the next point.

4. Finally, band 23 that described the behavior of Amide I in Zone IV showed a marked drop. The last two bands mentioned are directly connected to the presence of regularly 2D crystalline SL, whose unique architecture is composed of two glycoproteins.

The reduction of the peak is correlated with the degradation of the S-layer and therefore with the consequent degradation of the OM, as previously observed and described.

The inherent high molecular specificity of Raman spectroscopy provided rich information on the metabolic activity of living bacterial cells and on the Untreated Si_3N_4 biomaterial substrate.

Raman data showed clear signs of degradation in DNA, protein, and phospholipid structures after the exposure to the Untreated Si_3N_4 surface.

5.2.3 Linking Si_3N_4 surface modulation to bacterial strains metabolism

As the explanation of the variation of the most interesting bands together with the description of the unique characteristics of each bacterium studied in this work have already been presented in paragraph 5.2.2, in this section will be highlighted only the most marked differences between Raman spectra of different superficial treatments.

The alteration of the chemistry of the Si_3N_4 surface by HF-etching and thermal oxidation in N_2 and air does not cancel out the main signs of antibacterial behavior in bacterial spectra recorded on the Untreated Si_3N_4 samples.

However, some differences can be noticed by monitoring each bacterium metabolism on the surfaces of chemically modified samples.

- *Porphyromonas gingivalis*

The main differences among *P. gingivalis* spectra belonging to the various manufacturing processes are shown in Fig. 56.

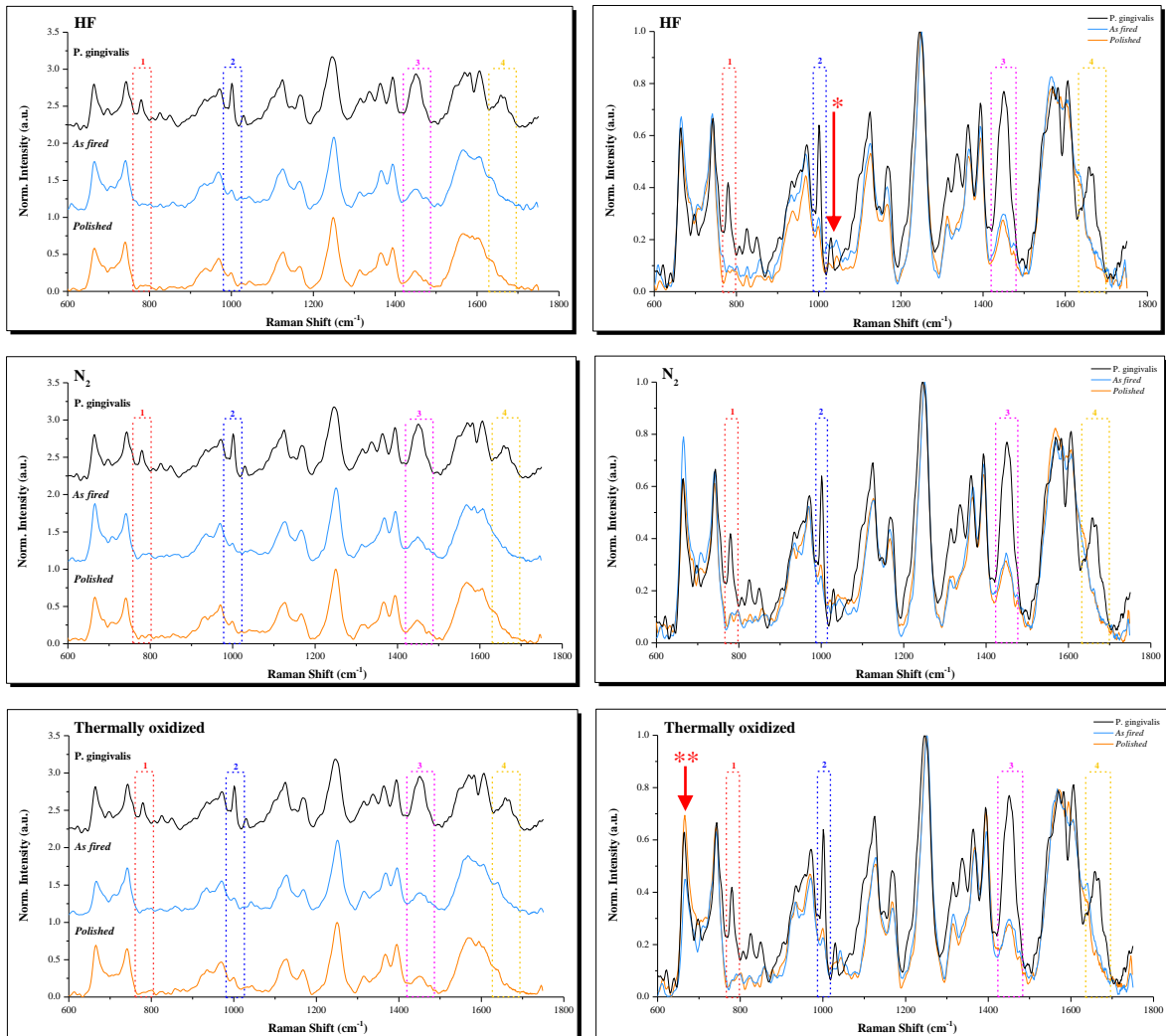


Fig. 56. Raman spectra overlapping and comparison between *P. gingivalis* and HF, N₂ and Thermally oxidized samples.

They can be listed as follows:

1. In the Zone I of all surface-modified samples, the DNA band at 780 cm⁻¹ is equally damaged. The exposure to the treated sample surfaces does not alter significantly the morphology of the spectral Zone I as compared to exposure to the Untreated Si₃N₄ surface. However, is observed a significant intensity decrease for band at 664 cm⁻¹ for the Thermally oxidized sample (“**”), in particular in *as fired*

morphology, which is a trend undetected in either the Untreated or HF sample. The variations of these bands are a further proof of DNA degradation in its structure and the loss of the genetic heritage of the bacterium.

2. The band 9 of Phe located in Zone II at 1001 cm^{-1} presents the same trend in all compounds. The compound peroxyxynitrite positioned at 1044 cm^{-1} is not detected on the oxidized Si_3N_4 sample, while it is again found (i.e., although with a weaker intensity) on the HF sample (“*”) similar to the Untreated Si_3N_4 one. Raman intensities of this peroxyxynitrite band, collected under exactly the same spectroscopic conditions, were systematically null for *P. gingivalis* spectrum cultured on Thermally oxidized Si_3N_4 and twofold lower on HF as compared to the Untreated case.
3. In Zone III, a significant reduction in Raman intensity of band 18 at 1450 cm^{-1} is recorded for all samples. This characteristic indeed proves, as discussed in the previous section, the common degradation of the lipid, protein and carbohydrate structures in the bacterial cell membrane.
4. Regarding Zone IV, in all samples the wavenumber range between 1658 and 1665 cm^{-1} assigned to Amide I (band 23) in α -helix and β -sheet are similar to that described in the previous section for *P. gingivalis* cultured on the Untreated sample. The behavior of Amide I band consistently reveals a low metabolic activity of the bacterial cells, and the lowered Raman intensity directly representing the loss of their chemical composition and functionality.

As in the previous description, it is not easy to define which surface morphology demonstrates a greater antibacterial activity, because in all Si_3N_4 samples both spectra (*as fired* and *polished*) showed a similar trend.

It would be necessary to perform additional experiments and further Raman acquisitions.

- *Treponema denticola*

The interpretation of the data obtained about this bacterium appears to be always the most complex.

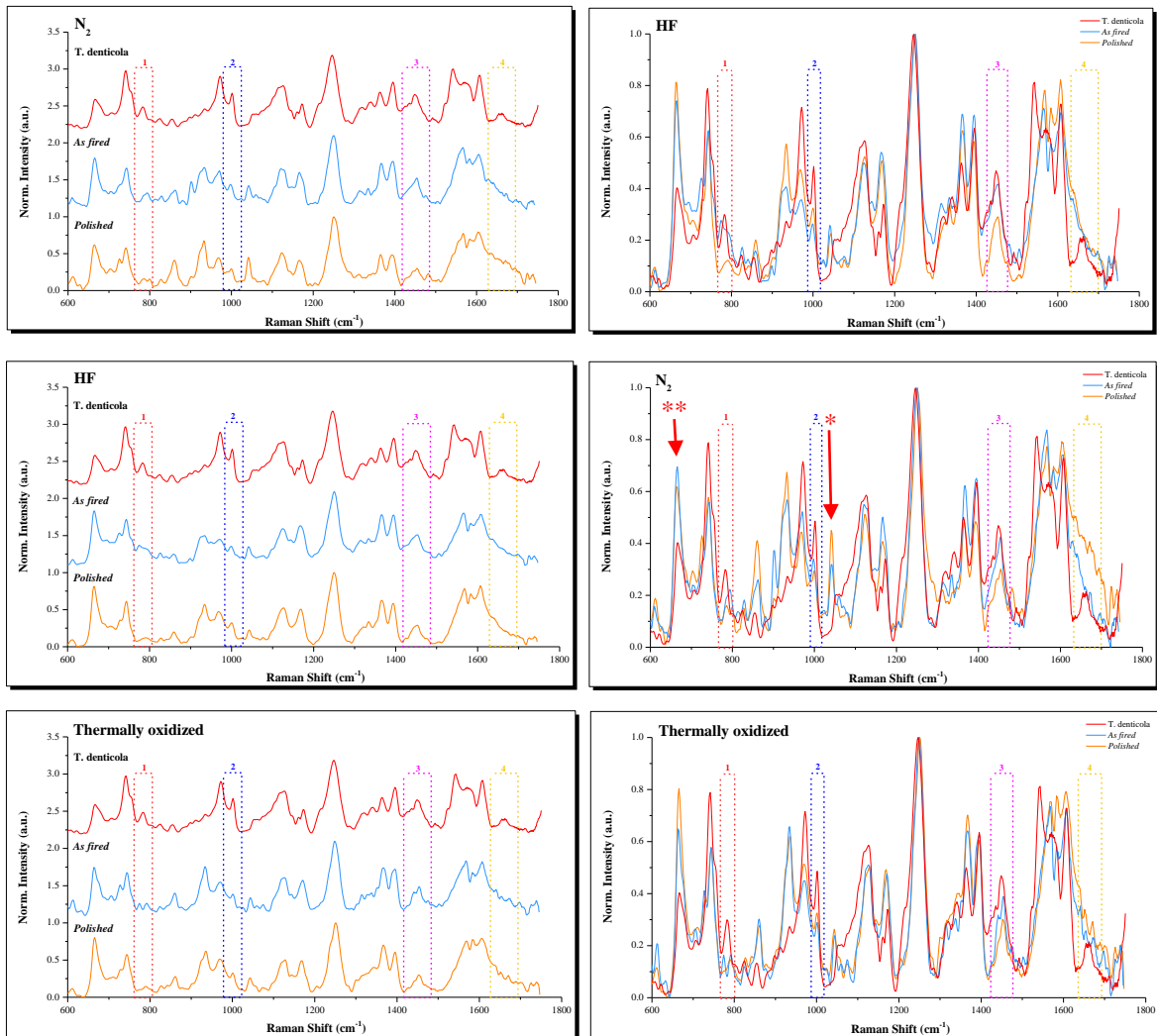


Fig. 57. Raman spectra overlapping and comparison between *T. denticola* and HF, N₂ and Thermally oxidized samples.

From Fig. 57 is possible to deduce the following differences:

1. The degradation of band 4 in Zone I appears to remain unchanged in thermally oxidized in air sample, while in others it seems to be less marked and damaged than the Untreated material.

The peak located at 664 cm⁻¹ (band 1) does not undergo significant variations, with the exception of chemical treatment in N₂ (“**”) that experiences a slight reduction in intensity. However, the trend of the peaks of the three superficial processes in

this spectral region mainly remains very similar to that observed in the Untreated case.

2. Regarding the peaks in Zone II, for that relating to Phe, whose band 9 is located at 1001 cm^{-1} , is possible to observe a similar behavior to that described in the previous section for *T. denticola* cultured on the Untreated layer. So, the degradation of this amino acid in the carboxyl terminal portion of serine protease involves the inactivation of the enzymatic activity and the loss by the bacterium of its capacity of adherence and virulence. Instead, that relating to the new peak that appears at 1044 cm^{-1} , it is associated to a strong and visible increase of intensity, in particular in the N_2 -treated sample (“*”).

The decrease in intensity of both the band of nitrogenous bases that of Phe are strongly connected with the increase of peroxyxynitride’s band intensity, because due to its oxidizing properties, peroxyxynitrite can damage many molecules within the cell, including DNA and proteins.

3. The Raman intensity of band 18 in Zone III remains unchanged and does not monitor any significant variation at this specific frequency.
4. The spectroscopic situation regarding the frequency band of Zone IV is more complex. The development of this area is very tired: the treatment in air does not change, one in N_2 increases in intensity while the HF appears to decrease slightly.

Raman spectra collected for *T. denticola* once again demonstrate the uniqueness of this species. The fact that the data collected for the different treatments are nearly equal to those found for Untreated could mean that the external composition of the bacterium is not affected by the different superficial manufacturing, or for this species may be required a more prolonged exposure time to see most marked changes in its biochemical composition.

- *Tannerella forsythia*

Also spectra of *T. forsythia* seem to present a trend much more complex than those of *P. gingivalis*. But, in this case, the intensity of the bands are very similar to those of the Untreated specimen, as shown in Fig. 58.

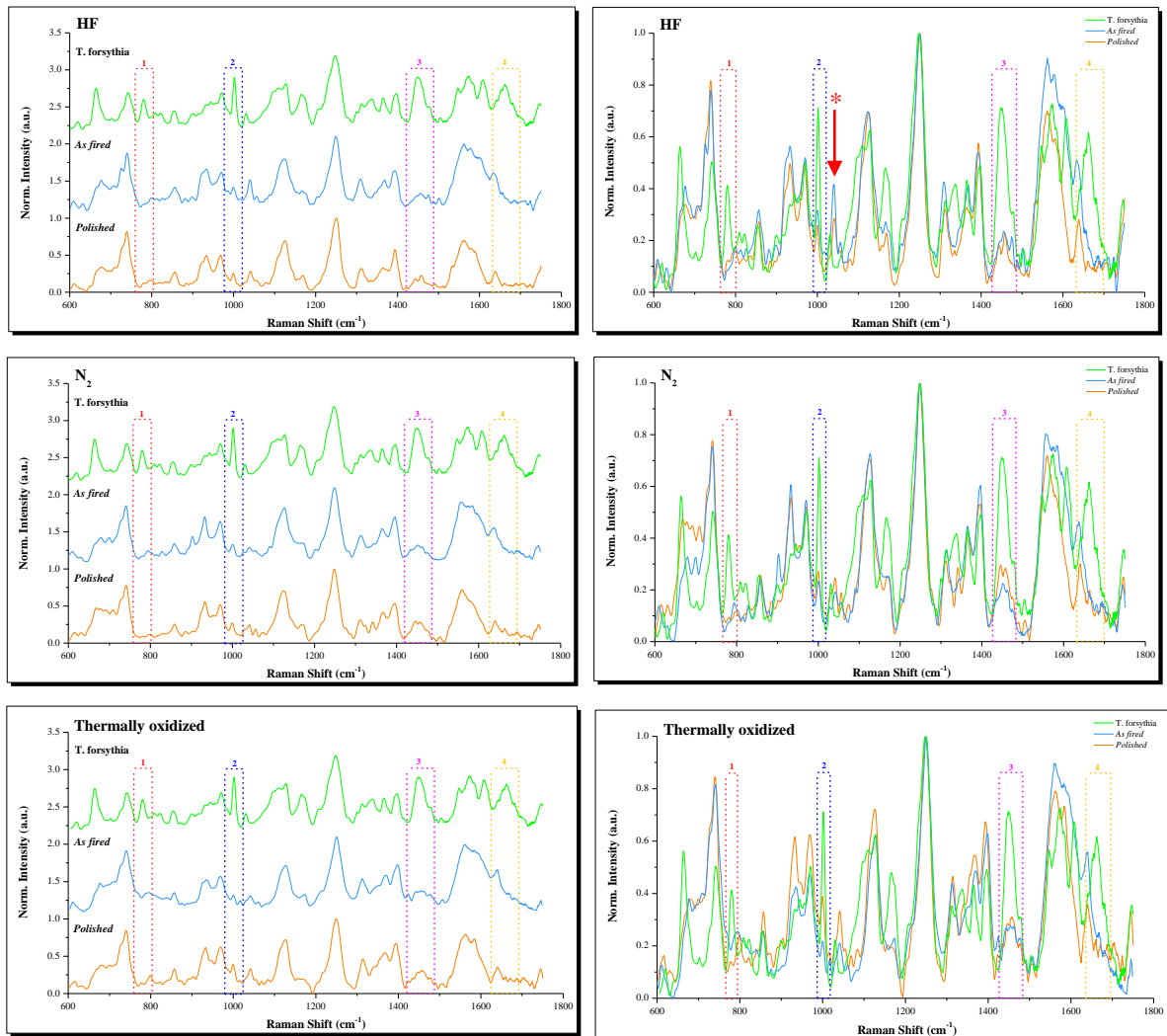


Fig. 58. Raman spectra overlapping and comparison between *T. forsythia* and HF, N_2 and Thermally oxidized samples.

The main observations that can be derived are the following:

1. The degradation in Zone I of band 4 relative to the nitrogen bases of nucleic acid at 780 cm^{-1} remains unchanged in both the HF-etching treatment and in the N_2 oxidative process. The only exception is for the sample treated in air, where the band related to the *as fired* superficial morphology increases in intensity. Also the

band localized at 664 cm^{-1} experiences a considerable reduction. The decrease of intensity in both bands is related to the loss of genetic information necessary for the biosynthesis of DNA and protein molecules essential for the development and the correct operation of these microorganisms.

2. In Zone II, the peak of the Phe (band 9) remains unaltered, and is not detected any change. The appearance of sharp and intense Raman band of peroxytrifluoride at 1044 cm^{-1} , collected under exactly the same spectroscopic conditions, is similar to that on the Untreated Si_3N_4 , even if there is an increase of the *as fired* peak in the case of the treatment in HF (“*”).
3. The representative peak of Zone III, which appears to 1450 cm^{-1} and is connected to the CH_2 bending mode of protein and C-H deformation mode of lipids and carbohydrates, is not subject to any variation in the intensity than the precedent treatment.
4. The Raman intensity of band 23 in Zone IV related to Amide I is prone to considerable degradation especially in the case of *polished* morphology. The trend of the peaks is very similar in all three treatments, and this characteristic proves, as discuss in the previous section of *T. forsythia*, the common degradation of the protein structure in the bacterial SL, which constitutes an additional barrier to the external environment.

At the end of this explanation and description, which have tried to analyze and compare the variation of the main significant band of all data collected experimentally by Raman vibrational spectroscopy, is possible to affirm that the spectra of different surface treatments do not show significant differences and strongly marked than those collected on Untreated sample.

In fact, all selected peaks follow the same trend of the Untreated sample.

5.3 Fluorescence analysis of *P. gingivalis* bacterial cell

Confirmation for the death of *P. gingivalis* bacteria after the exposure to the Si_3N_4 surface can be obtained by conventional fluorescence microscopy after staining the microorganism with PI and CFDA markers, which colored in red and green the dead and alive bacteria, respectively. This experiment was conducted only on *P. gingivalis* cells and not on the other two strains because, as mentioned in the paragraph 5.2.1, it is the representative of the red complex and also because this experimental project is still in a preliminary stage. Moreover, the fluorescence analyses were performed only on *polished* samples and they have not been conducted on the N_2 -treated surface.

The results of the experiments are shown in Fig. 59 a) and b) for the Pol-Untreated and Pol-Thermally oxidized surfaces, respectively. A micrograph of stained bacteria on the Pol-HF surface is omitted here because it appeared conspicuously the same as that shown in a) for the Pol-Untreated one.

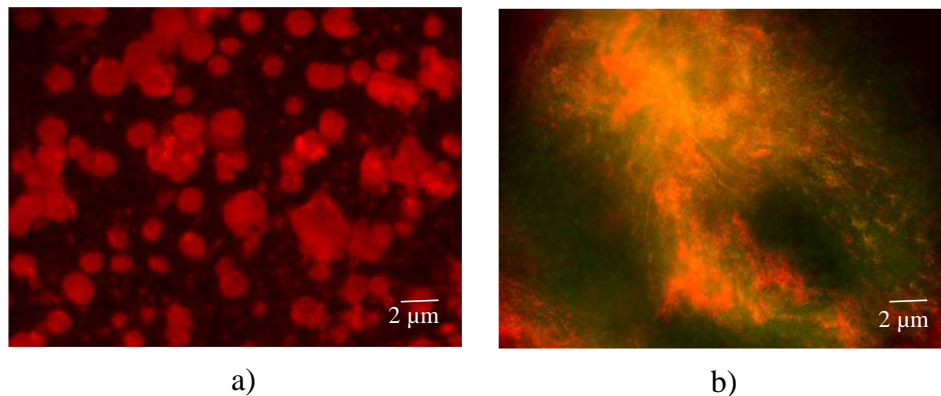


Fig. 59. Fluorescence microscopic visualization of adherent bacteria on: a) Pol-Untreated and b) Pol-Thermally oxidized.

Considering the two-color fluorescent assay, the staining capacity of the dyes seems to correlate with the physiological state of *P. gingivalis* cells. In the Pol-Untreated and Pol-HF specimens, all bacteria have absorbed the molecules of the compound PI, and for this reason, they are completely red-stained. The accumulation inside the cell of dye is a clear signal both of the disruption of the double-membrane structure and the loss of permeability barrier, which represent irreparable damage and thus cell death.

On the other hand, bacterial cells on the oxidized surface widely spread and colonized. The greenish areas with some orange rather than red stain prove a less progressed lytic behavior as compared to Pol-Untreated and Pol-HF surfaces for the same testing conditions. In the

case of CFDA marker, only viable bacterial cells can accumulate it, indicating membrane permeability, metabolic activity and viability, because this dye has the ability to penetrate intact membranes and contrasting cell nuclei and chromatin for live cell fluorescence microscopy [105].

5.4 Chemical at the surface of Si_3N_4 bioceramics

Before starting to present the chemical results obtained with the pH microscopy, it is important to specify that also in this case all experimental measures were conducted exclusively on *polished* samples, and it has not been considered the N_2 treatment.

In Fig. 60 is shown the room-temperature evolution of pH around the Pol-Untreated Si_3N_4 as a function of time.

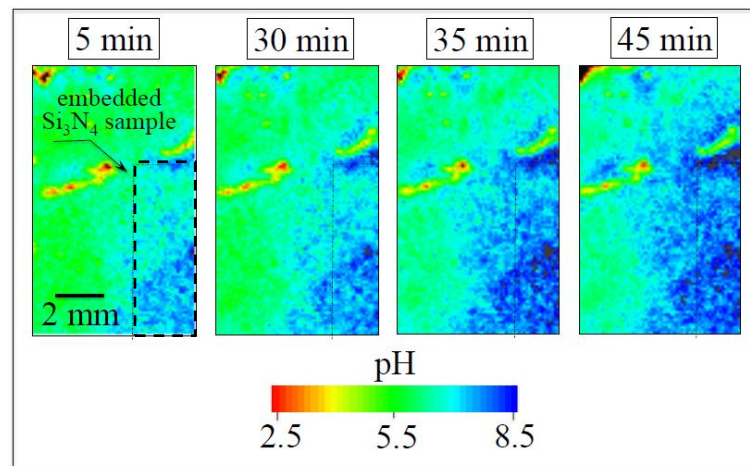


Fig. 60. Evolution of pH on Pol-Untreated surface.

As seen, the pH-buffering action at the surface of the Si_3N_4 sample becomes evident through the gradual conversion into alkaline values (pH \sim 8.5) of increasingly wider regions of the surrounding acidic gel. Note that these regions originally are strongly acidic (average pH of the unperturbed gel = 4.5).

The gradual spread of the alkaline environment around the sample can clearly be visualized in a time frame in the order of few tens of minutes. However, the initial change in alkalinity at the interface between Si_3N_4 sample and acidic gel film is rather quick, which made it difficult to map the situation at nearly time zero. Moreover, the pH buffering effect is found independent of the sample size.

The same effect can also be observed by repeating the experiment with a smaller sample (about 400 x 300 μm in size; data not shown here) machined from the same Si_3N_4 sample analyzed in Fig. 60. The pH mapping experiments were repeated on samples with exactly the same geometry of the disks employed in bacterial experiments, and a direct comparison was carried out among Pol-Untreated, Pol-Thermally oxidized, and Pol-HF samples.

The results of pH microscopy performed after 45 min exposure to acidic gel on the former two samples, respectively, are presented in Fig. 61 a) and b). The output of this experiment on the Pol-HF sample is undistinguishable from that of the Pol-Untreated sample in Fig. 61 a), so it is not explicitly displayed here.

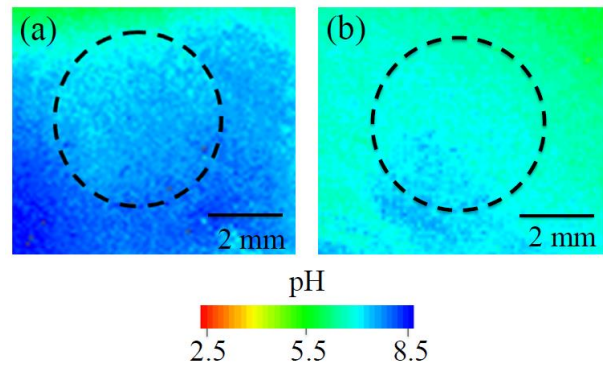


Fig. 61. pH microscopy performed on: a) Pol-Untreated and b) Pol-Thermally oxidized sample.

From a comparison among different samples, it can be stated that the observed trends are basically the same, although the efficiency of the pH buffering effect seems to be mitigated by thermal oxidation, when testing the samples on an equal footing. Based on this experimental finding, Fig. 62 tries to show a schematic draft of the sequence of chemical events leading to the observed phenomenon of pH buffering.

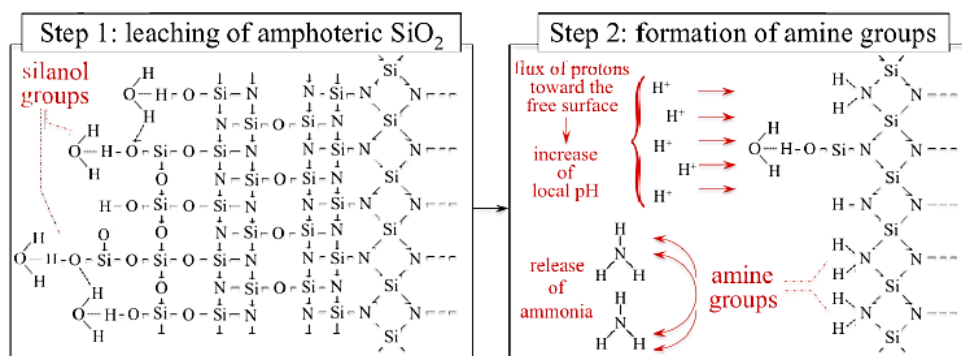


Fig. 62. Explanation of the succession of events during the pH experiments on Pol-Untreated Si_3N_4 surface.

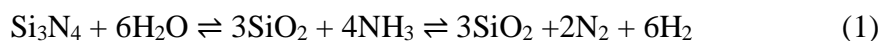
A layer of amphoteric SiO_2 , which gradually incorporates increasing amounts of N ions toward the bulk Si_3N_4 core, covers the surface of the Pol-Untreated sample. The initial step of the reaction in the acidic media (Step 1) consists in the dissolution of amphoteric silica through detachment of silanol adsorbates, Si-OH , from its surface in the form of silicic acid, Si(OH)_4 . Note, however, that Si(OH)_4 is unstable in water and its molecules should

readily condense with one another to form water and polymeric chains. With progressing the dissolution of the amphoteric silica layer, amine adsorbates, Si₂-NH (and a minor fraction of Si-NH), start to proliferate on the Si₃N₄ surface (Step 2), and to fully replace the population of silanol adsorbates. Unlike silanols, the amine adsorbates are quite strongly bonded to the surface, but tend to attract H⁺ protons to form ammonia, NH₃. The strong driving force to produce ammonia indeed induces a massive flux of protons toward the adsorbed amine species. This flux depletes the solution of protons and raises the local pH at the solid/liquid interface, which is exactly what is observed in pH mapping experiments. Note that oxidation of the surface results in a thicker layer of glassy silica on top of the surface structure, which in turn involves longer times needed for exposing the buffering agents to the external environment. This observation can explain the results shown in Fig. 61 a) and b).

So, thanks to the presentation and description of data disclosed so far, it is possible to declare that the degradation and the resulting bacterial cells lysis of the three strains considered in the present work and observed on Si₃N₄ surfaces cannot be simply attributed to osmotic shock. Accordingly, the mere rise in pH, which are observed in Figs. 60 and 61, cannot be the cause of the bacterial lytic behavior.

The experiments described in this paper were originally designed to investigate and clarify the effect of surface charge on the bacteriostatic behavior of Si₃N₄ bioceramics. However, according to fluorescence microscopy, it is reached the conclusion that the *polished* Thermally oxidized (hydroxyl-rich) Si₃N₄ surface, namely the most negatively charged surface in the tested series, experienced reduced effectiveness in inducing bacterial lysis as compared to (amine-rich) *polished* Untreated and HF surfaces. Accordingly, one cannot either simply rationalize the lytic behavior by invoking the electrical repulsion of bacteria from the Si₃N₄ surface. These considerations drove toward searching for an explanation of chemical nature to the observed antibacterial behavior.

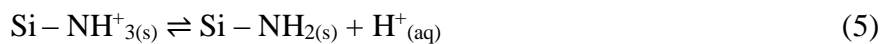
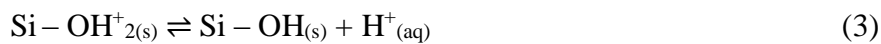
The main reactions that classical surface chemistry recognizes for the overall process of chemisorption-oxidation-dissolution at the surface of Si₃N₄ bioceramic can be written, as follows:



Reactions (1) and (2) are important in biomedical applications since they play a role in the tribological and bioinertness of Si₃N₄. Moreover, they explicitly show the formation in a sequential cascade of ammonia gas, which is a well-known characteristic of the slurries of Si₃N₄ powder employed for sintering ceramic components, and silicic acid.

Furthermore, in a previously published paper [106], it was directly measured an increase in pH at the immediate surface of silicon nitride immersed in water for various equilibrium (acidic) pH values by means of Raman spectroscopy. Such pH-buffering effect was the same as that observed here by direct pH microscopy.

In aqueous solution, the predominant functional groups at the very surface of Si₃N₄, namely Si-NH₂ and Si-OH, might further dissociate via acid-base reactions, as follows:



where the subscripts (s) and (aq) refer to the solid and aqueous state of the molecules, respectively. Note that Eq. (3), which represents the protonation of silanol groups, can only occur in highly acidic environment, which is not the case here. Accordingly, the two reactions represented by Eqs. (4) and (5) are the key in deciding the pH environment at the Si₃N₄ surface with changing the concentration balance between of H⁺ and OH⁻ ions.

There are numerous studies that have investigated the surface chemistry of Si₃N₄, and Fubini and co-workers conducted one of these [107]. They were able to establish that the presence of active sites at ground and polished ceramic surfaces interfered with macrophage metabolism stimulating fibrogenic factors. Based on electron paramagnetic resonance, which only detects unpaired electrons, these researchers were able to distinguish surface reactive species of two types: one type implying homolytic cleavage of Si bond, and the second type relating to heterolytic bond cleavage. Some of the detected active species were superoxide radicals, such as radicals ($\equiv \text{Si-O}^*$) and superoxide radicals ($\equiv \text{Si}^*\text{O}_2^-$).

In other words, the most important feature in the surface of Si₃N₄ bioceramics and its related dissociation reactions is that they make it available important ionic precursors to the formation of peroxyxynitrite, which have indeed directly detected in this study by Raman spectroscopy in bacterial cultures exposed to amine-rich Si₃N₄ surfaces. Unpaired

electrons react with the adsorbed O_2 on the Si_3N_4 surface to yield $O_2^{\cdot-}$ radical anions and, subsequently, other highly oxidative protonated radicals active in bacterial inactivation. The bacterial strains investigated in the present work, *P. gingivalis*, *T. denticola* and *T. forsythia*, are all asaccharolytic microorganisms capable to metabolize nitrogenous compounds as a source of energy and to generate a microenvironment abundant in ammonia and other important metabolic by-products. But, the nitrate-nitrite-ammonia conversion process also involves the production of nitric oxide (NO) from nitrite reduction. Despite NO being a freely diffusible, highly reactive, and cytotoxic gas, i.e., *P. gingivalis* under normal metabolic conditions is capable to efficiently remove it through reactions with oxyhemoglobin to promptly form nitrate. These reactions actually prevent NO from directly reaching oxygen.

Now, looking at the dissociation reactions occurring at the surface of Si_3N_4 (i.e., Eqs. (1) and (4)), one might figure out a simultaneous process in which the transient Eq. (1) actually serves to efficiently *feed* *P. gingivalis* of nitrogen, thus inviting it to abundantly produce NO among other metabolic by-products. Simultaneously, Eq. (4) produces active oxygen species, eventually including superoxide radicals, in close proximity to NO.

These circumstances might lead to the quick formation of peroxynitrite (i.e., as detected by Raman spectroscopy), which actually *poisons* the microorganisms. Note also that NO and active oxygen species do not need to be produced within the same cell to form peroxynitrite, because NO can readily move through membranes between bacterial cells. The proposed mechanism of *feeding/poisoning* operated by the Si_3N_4 surface is schematically shown in Fig. 63.

The important component of NO stress resistance in bacterial strains is exactly their ability to maintain non-toxic NO intracellular concentrations.

However, the cascade of chemical reactions taking place at the surface of Si_3N_4 bioceramics helps the activity of cellular systems by tilting the local chemical equilibrium toward peroxynitrite rather than nitrate formation.

According to this interpretation, one can also explain why the effectiveness of the antibacterial activity of Si_3N_4 strongly depends on surface chemistry modulation, for the balance between feeding and poisoning compounds needing to reach an optimal gain.

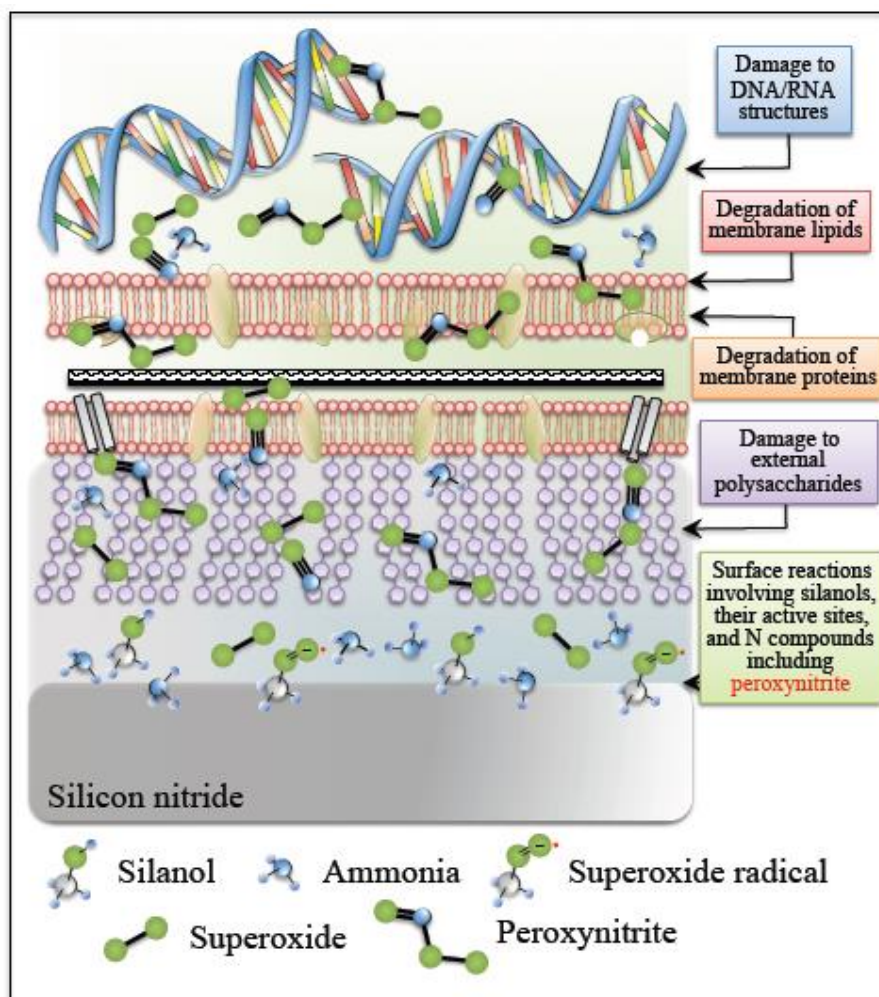


Fig. 63. Schematic description of degradative events on Si_3N_4 surface.

The better performance of the *polished* Untreated surface suggests that a balance between amine and hydroxyl groups on the surface leads to a better lytic performance as compared to surfaces shifted toward amine- or hydroxyl-rich sides.

However, the best balance has yet to be experimentally identified and there are ongoing studies to fulfill this task.

CHAPTER VI: CONCLUSION

Several analysis techniques were employed in the present work to study the surface chemistry and morphology of Si_3N_4 bioceramic. The information gathered from the Raman spectroscopy, 3D laser-scanning microscope, X-ray diffraction, SEM and EDX provide a comprehensive understanding of the various composition of this material. It was found that its surface could be varied significantly through conventional mechanical, chemical and thermal treatments, and also through different surface morphology.

Raman spectroscopic monitoring of bacterial strains lying on the surface of Si_3N_4 bioceramics revealed relevant alterations in their metabolism, including degradation of nucleic acid, and drastic reductions in phenylalanine, Amide I proteins, and lipids. Such alterations specifically related to the formation of peroxyxynitrite, is in turn a consequence of nitric oxide metabolic release by bacteria meeting active oxygen species at the Si_3N_4 surface.

Moreover, a mechanism of *feeding/poisoning* of the three Gram-negative bacteria was hypothesized, which originated from the peculiar chemical reactions occurring at the Si_3N_4 surface.

Si_3N_4 bioceramics appear to possess a unique surface chemistry to satisfy synergistic interactions between solid surface and biological environment at the molecular scale. Affinity to oxygen is one main property of the Si_3N_4 surface with its surface “passivation layer” of tunable stoichiometry at the molecular scale, which is shown here to be key in designing bioceramics with improved functionalities. The peculiar formation of amine and silanol adsorbates on the Si_3N_4 surface lies at the origin of a stream of positive interactions between the solid surface and the biological environment. They include a pronounced pH-buffering effect (newly demonstrated here) through attraction toward the Si_3N_4 surface of H^+ protons, and local formation of ammonia, which is interfaced with antibacterial activity. Using Si_3N_4 in dentistry promises an improved bacteriostatic effectiveness in dental implants coupled with a unique capacity of “downregulating” the bacterial metabolism. The surface of Si_3N_4 naturally drifts towards a protective chemical action, which parallels the action of cellular systems in activating enzyme complexes to produce superoxide species and to favor the formation of peroxyxynitrite.

In conclusion, it is important to remark that Si_3N_4 seem to possess the “right chemistry” to

evolve toward an increasingly beneficial state with respect to a diseased oral environment. This useful aspect of Si_3N_4 surface chemistry definitely deserves further studies. With its direct impact on bacterial metabolic responses, it reflects the intrinsic capacity of implanted Si_3N_4 components of re-establishing healthy biological environments and stimulating specific functions of the human body through their friendly evolution *in vivo*.

REFERENCE

- [1] F. L. Riley, "*Silicon nitride and related materials*". J. Am. Ceram. Soc., 2000. **83** (2): 245-265.
- [2] R. J. S. (Lord) Rayleigh, "*Nitrogen, argon, and neon in the Earth's crust with applications to cosmology*". Proc. R. Soc. (London), 1939. **170** No. 943, 451-464.
- [3] L. R. Nittler, R. Strebler, R. M. Walker, and E. Zinner, "*Silicon nitride from supernovae*". Astrophys. J., 1995. **453** (1): 25-28.
- [4] M. R. Lee, S. S. Russell, J. W. Arden, and C. T. Pillinger, "*Nierite (Si_3N_4), a new mineral from ordinary and enstatite chondrites*". Meteoritics, 1995. **30** (4): 387-398.
- [5] H. Sainte-Claire Deville and F. Wöhler, "*On the direct compound silicon nitride*". Liebigs Ann. Chem. Pharm., 1859. **110**: 248-250.
- [6] (a) Carborundum Co., "*Silicon Nitride Bonded Articles*". U.S. Pat. No. 2 618 565, Nov. 18, 1952.
(b) Carborundum Co., "*Silicon Nitride Bonded Refractory Articles*". U.S. Pat. No. 2 636 828.
- [7] G. G. Deeley, J. M. Herbert, and N. C. Moore, "*Dense silicon nitride*". Powder Metall., 1961. **4** (8): 145-151.
- [8] (a) R. N. Katz, "*Progress in nitrogen ceramics*", U.S. National Programmes for Energy Conversion. NATO ASI Series E: Applied Sciences, No. 65. Edited by F. L. Riley. Martinus Nijhoff, Boston, MA, 1983. 727-735.
(b) W. Bunk, and M. Böhmer, "*Ceramic components for vehicular gas turbines*" Status Report 1981 on the German BMFT-Sponsored Programme; see Ref. 18(a), 737-751.
(c) H. Suzuki, "*Current Japanese research programmes into nitrogen ceramics*"; see Ref. (a), 755-768.
- [9] C. B. Carter, and M. G. Norton, "*Ceramic materials: Science and Engineering*". Springer, 2007. 27.
- [10] B.S. Bal, and M.N. Rahaman, "*Orthopedic applications of silicon nitride ceramics*". Acta Biomaterialia, 2012. **8** (8): 2889-2898.
- [11] B.S. Bal, and M.N. Rahaman, "*The rationale for silicon nitride bearings in orthopaedic applications*". Advances in ceramics - Electric and Magnetic Ceramics, Bioceramics, Ceramics and Environment, 2011. 421-432.
- [12] J. Lang, "*Some aspects of the structure and crystal chemistry of nitrides*". Nitrogen Ceramics, NATO ASI Series E: Applied Science, No. 23. Edited by F. L. Riley. Noordhoff, Leyden, The Netherlands, 1977. 89-107.
- [13] P. Popper, and S. N. Ruddlesden, "*The preparation, properties, and structure of silicon nitride*". Trans. Br. Ceram. Soc., 1961. **60**: 603-626.
- [14] W. Wang, M. Hadfield, and AA. Wereszczak, "*Surface strength of silicon nitride in relation to rolling contact performance*". Ceramics International., 2009. **35** (8): 3339-3346.
- [15] C. Wang, X. Pan, and M. Rohle, "*Silicon nitride crystal structure and observations of lattice defects*". Mater. J. Science, 1996. **31** (20): 5281-5298.
- [16] S. Hampshire, "*Silicon nitride ceramics: review of structure, processing and properties*". J. of Achievement in Materials and Manufacturing Eng., 2007. **24** (1): 43-50.
- [17] J. Z. Jiang, F. Kragh, D. J. Frost, K. Stahl, and H. Lindelov, "*Letter to the editor: Hardness and thermal stability of cubic silicon nitride*". J. Physics: Condensed Matter, 2001. **13** (22): 515-520.

- [18] P. Popper, and S.N. Ruddlesden, "Crystal structure of silicon nitride". Bulletin of the Chemical Society of Japan, 1959. **32**: 417-419.
- [19] J.P. Luongo, "Infrared characterization of α - and β -crystalline silicon nitride". J. Electrochem. Soc., 1983. **130** (7): 1560-1562.
- [20] S.N. Ruddlesden, and P. Popper, "On the crystal structure of the nitrides of silicon and germanium". Acta Crystallogr., 1958. **11**: 465-468.
- [21] D. Hardie, and K.H. Jack, "Crystal Structures of Silicon Nitride". Nature, 1957. **180**: 332-333.
- [22] G. Ziegler, J. Heinrich, and G. Wotting, "Relationships between processing, microstructure and properties of dense and reaction-bonded silicon nitride". Mater. J. Science, 1987. **22** (9): 3041-3086.
- [23] F. C. Chen, and A. J. Ardell, "Fracture toughness of ceramics and semi-brittle alloys using a miniaturized disk-bend test". Mater. Res. Innovat., 2000. **3** (5): 250-262.
- [24] B. Cappi, S. Neuss, J. Salber, R. Telle, R. Knüchel, and H. Fischer, "Cytocompatibility of high strength non-oxide ceramics". Biomed. J. Mater. Research, 2009. **93A** (1): 67-76.
- [25] GL. Fisher, KL. McNeill, and JT. Smith, "In vitro effects of fibrous and nonfibrous silicon nitride on bovine pulmonary macrophages". Environ. Res., 1989. **50** (2): 279-288.
- [26] CR. Howlett, E. McCartney, and W. Ching, "The effect of silicon nitride ceramic on rabbit skeletal cells and tissue. An in vitro and in vivo investigation". Clin. Orthop. Relat. Res., 1989. **244**: 293-304.
- [27] M. Mazzocchi, and A. Bellosi, "On the possibility of silicon nitride as a ceramic for structural orthopaedic implants. Part I: processing, microstructure, mechanical properties, cytotoxicity". J Mater. Sci.: Mater. Med., 2008. **19** (8): 2881-2887.
- [28] M. Mazzocchi, D. Gardini, P. L. Traverso, M. G. Faga, and A. Bellosi, "On the possibility of silicon nitride as a ceramic for structural orthopaedic implants. Part II: chemical stability and wear resistance in body environment". J Mater. Sci.: Mater. Med., 2008. **19** (8): 2889-2901.
- [29] C.C. Sorrell, P.H. Hardcastle, R.K. Druitt, and E.R. Mc Cartney, Proceedings 5th Meeting and Seminar on: Implants for Spine. Ceramics, Cells and Tissues annual conferences, Faenza (Italy), ed. by A. Ravaglioli, A Krajewski (ISTEC-CNR edn, 1999). 47
- [30] D. W. Richerson, and D.W. Freita, "Opportunities for Advanced Ceramics to Meet the Needs of the Industries of the Future". Oak Ridge National Laboratory, 1998.
- [31] "Space Shuttle main engine enhancements". NASA. Retrieved, 2009.
- [32] Y. S. Zhou, M. Ohashi, N. Tomita, K. Ikeuchi, and K. Takashima, "Study on the possibility of silicon nitride – Silicon nitride as a material for hip prosthesis". Mater. Sci. Eng., 1977. **125**: 125-129.
- [33] M. Akazawa, and K. Kato, "Wear properties of Si_3N_4 in rolling-sliding contact". Wear, 1988. **124** (1): 123-132.
- [34] Y.S. Zhou, K. Ikeuchi, and M. Ohashi, "Comparison of the friction properties of four ceramic materials for joint replacements". Wear, 1997. **210** (1-2): 171-177.
- [35] G. Willmann, "Improving bearing surfaces of artificial joints". Adv. Eng. Mater., 2001. **3** (3): 135-141.
- [36] A. Neumann, C. Unkel, C. Werry, C.U. Herborn, H.R. Maier, C. Ragoss, and K. Jahnke, "Prototype of a silicon nitride ceramic-based miniplate osteofixation system for the midface". Otolaryngol. Head Neck Surg., 2006. **134** (6): 923-930

- [37] C.C. Sorrell, P.H. Hardcastle, R.K. Druitt, C.R. Howlett, and E.R. McCartney, Results of 15-year clinical study of reaction bonded silicon nitride intervertebral spacers, in: Proc. 7th World Biomater. Conf. (2004) 1872.
- [38] D. A LaVan, T. McGuireand, and R. Langer, "Small-scale systems for in vivo drug delivery". Nature Biotech., 2003. **21**: 1184-1191.
- [39] J. Kotzar, M. Freas, P. Abel, A. Fleischman, S. Roy, C. Zorman, J.M. Moran, and J. Melzak, "Evaluation of MEMS materials of construction for implantable medical devices". Biomaterials, 2002. **23**: 2737-2750.
- [40] B.W. Kristensen, J. Noraberg, P. Thiébaud, M. Koudela-Hep, and J. Zimmer, "Biocompatibility of silicon-based arrays of electrodes coupled to organotypic hippocampal brain slice cultures". J. Brain Res., 2001. **896** (1-2): 1-17.
- [41] C.S. Giannoulis, and T.A. Desai, "Characterization of proteins and fibroblasts on thin inorganic films". J. Mater. Sci: Mater. Med., 2002. **13** (1): 75-80.
- [42] D. J Gorth, S. Puckett, B. Ercan, T. J Webster, M. Rahaman, and B. S. Bal, "Decreased bacteria activity on Si₃N₄ surfaces compared with PEEK or titanium". Int. J. Nanomedicine, 2012. **7**: 4829-4840.
- [43] M. Handfield, H. V. Baker, and R. J. Lamont, "Beyond good and evil in the oral cavity: insights into host-microbe relationships derived from transcriptional profiling of gingival cells". J. Dent. Res., 2008. **87** (3): 203-223.
- [44] J Highfield, "Diagnosis and classification of periodontal disease". Australian Dental Journal, 2009. **54** (1 Suppl): S11-S26.
- [45] L. A. Christersson, J. J. Zambon, and R. J. Genco, "Dental bacterial plaques. Nature and role in periodontal disease". J. Clin. Periodontol., 1991. **18** (6): 441-446.
- [46] F. Trindade, F. G. Oppenheim, E. J. Helmerhorst, F. Amado, P. S. Gomes, and R. Vitorino "Uncovering the molecular networks in periodontitis". Proteomics Clin Appl., 2014. **8** (0): 748-761.
- [47] P. I. Eke, B. A. Dye, L. Wei, G. O. Thornton-Evans, and R. J. Genco, "Prevalence of periodontitis in adults in the United States: 2009 and 2010". J. Dent. Res., 2012. **91** (10): 914-920.
- [48] C. A. Negrato, O. Tarzia, L. Jovanović, and L. E. Montenegro Chinellato, "Periodontal disease and diabetes mellitus". J. Appl. Oral Sci., 2013. **21** (1): 1-12.
- [49] N. Silva, L. Abusleme, D. Bravo, N. Dutzan, J. Garcia-Sesnich, R. Vernal, M. Hernández, and J. Gamonal, "Host response mechanisms in periodontal diseases". J. Appl. Oral Sci., 2015. **23** (3): 329-355.
- [50] Amin E. Hatem, "Epidemiology and risk factors of periodontal disease". Periodontal Diseases – A Clinician's Guide, 2012. 1-19.
- [51] Y. A. AlJehani, "Risk factors of periodontal disease: Review of the literature". International Journal of Dentistry, 2014. 1-10.
- [52] A. Mariotti, and A. F. Hefti "Defining periodontal health". BMC Oral Health, 2015. **15** (Suppl 1): S6.
- [53] B. J. Paster, I. Olsen, J. A. Aas, and F. E. Dewhirst, "The breadth of bacterial diversity in the human periodontal pocket and other oral sites". Periodontol. 2000, 2006. **42** (1): 80-87.
- [54] A. P. V. Colombo, S. K. Boches, S. L. Cotton, J. M. Goodson, R. Kent, A. D. Haffajee, S. S. Socransky, H. Hasturk, T. E. Van Dyke, and B. J. Paster, "Comparisons of subgingival microbial profiles of refractory periodontitis, severe periodontitis, and periodontal health using the human oral microbe identification microarray". J. Periodontol., 2009. **80** (9): 1421-1432.

- [55] Y. Jiao, M. Hasegawa, and N. Inohara, “*The role of oral pathobionts in dysbiosis during periodontitis development*”. *J. Dent. Res.*, 2014. **93** (6): 539-546.
- [56] S. C. Holt, and J. L. Ebersole, “*Porphyromonas gingivalis, Treponema denticola, and Tannerella forsythia: the “red complex”, a prototype poly bacterial pathogenic consortium in periodontitis*”. *Periodontol.* 2000, 2005. **38**: 72-122.
- [57] T. J. Silhavy, D. Kahne, and S. Walker, “*The bacterial cell envelope*”. Cold Spring Harb. Perspect Biol., 2010. **2**: 1-17.
- [58] S. Jordan, M. I. Hutchings, and T. Mascher, “*Cell envelope stress response in Gram-positive bacteria*”. *FEMS Microbiol. Rev.*, 2008. **32**: 107-146.
- [59] M. P. Bos, V. Robert, and J. Tommassen, “*Biogenesis of the Gram-negative bacterial outer membrane*”. *Annu Rev. Microbiol.*, 2007. **61**: 191-214.
- [60] M. P. Bos, and J. Tommassen, “*Biogenesis of the Gram-negative bacterial outer membrane*”. *Current Opinion in Microbiology*, 2004. **7** (6): 610-616.
- [61] N. Suzuki, M. Yoneda, and T. Hirofuji “*Mixed red-complex bacterial infection in periodontitis*”. *International Journal of Dentistry*, 2013. 1-7.
- [62] S. S. Socransky, and A. D. Haffajee, “*Periodontal microbial ecology*”. *Periodontol.* 2000, 2005. **38**: 135-187.
- [63] S. S. Socransky, A. D. Haffajee, M. A. Cugini, C. Smith, and R. L. Jr Kent, “*Microbial complexes in subgingival plaque*”. *J. Clin. Periodontol.*, 1998. **25**: 134-144.
- [64] Y. Jiao, M. Hasegawa, and N. Inohara, “*The role of oral pathobionts in dysbiosis during periodontitis development*”. *J. Dent. Res.*. 2014. **93**(6): 539-546.
- [65] J. Mysak, S. Podzimek, P. Sommerova, Y. Lyuya-Mi, J. Bartova, T. Janatova, J. Prochazkova, and J. Duskova, “*Porphyromonas gingivalis: major periodontopathic pathogen overview*”. *J. Immunol. Res.*, 2014. 1-9.
- [66] H. N. Shah, and M. D. Collins, “*Proposal for reclassification of Bacteroides asaccharolyticus, Bacteroides gingivalis, and Bacteroides endodontalis in a new genus, Porphyromonas*”. *International Journal of Systematic Bacteriology*, 1988. **38**: 128-131.
- [67] D. Mayrand, and S. C. Holt, “*Biology of asaccharolytic black-pigmented Bacteroides species*”. *Microbiol Rev.*, 1988. **52** (1): 134-152.
- [68] S.G. Dashper, C.A. Seers, K.H. Tan, and E.C. Reynolds, “*Virulence factors of the oral spirochete Treponema denticola*”. *J. Dent. Res.*, 2011. **90** (6): 691-703.
- [69] P. D. Veith, S. G. Dashper, N. M. O’Brien-Simpson, R. A. Paolini, R. Orth, K. A. Walsh, and E. C. Reynolds, “*Major proteins and antigens of Treponema denticola*”. *Biochimica et Biophysica Acta (BBA) – Proteins and Proteomics*, 2009. **1794** (10): 1421-1432.
- [70] K. Ishihara, and K. Okuda, “*Molecular pathogenesis of the cell surface proteins and lipids from Treponema denticola*”. *FEMS Microbiology Letters*, 1999. **181**: 199-204.
- [71] A. C. R. Tanner, M. A. Listgarten, L. J. Ebersole, and M. N. Strzempko, “*Bacteroides forsythus sp. nov., a slow-growing, fusiform Bacteroides sp. from the human oral cavity*”. *Int. J. Syst. Bacteriol.*, 1986. **36** (2): 213-221.
- [72] M. Sakamoto, M. Suzuki, M. Umeda, I. Ishikawa, and Y. Benno, “*Reclassification of Bacteroides forsythus (Tanner et al. 1986) as Tannerella forsythensis corrig., gen. nov., comb. nov.*”. *International Journal of Systematic and Evolutionary Microbiology*, 2002. **52**: 841-849.

- [73] G. Sekot, G. Posch, Y. J. Oh, S. Zayni, H. F. Mayer, D. Pum, P. Messner, P. Hinterdorfer, and C. Schäffer, "Analysis of the cell surface layer ultrastructure of the oral pathogen *Tannerella forsythia*". Arch. Microbiol., 2012. **194**: 525-539.
- [74] G. Posch, M. Pabst, L. Brecker, F. Altmann, P. Messner, and C. Schäffer, "Characterization and scope of S-layer protein O-glycosylation in *Tannerella forsythia*". J. Biol. Chem., 2011. **286**: 38714-38724.
- [75] T. Mineoka, S. Awano, T. Rikimaru, H. Kurata, A. Yoshida, T. Ansai, and T. Takehara, "Site-specific development of periodontal disease is associated with increased levels of *Porphyromonas gingivalis*, *Treponema denticola*, and *Tannerella forsythia* in subgingival plaque". J. Periodontol., 2008. **79**: 670-676.
- [76] A. D. Haffajee, R. P. Teles, and S. S. Socransky, "Association of *Eubacterium nodatum* and *Treponema denticola* with human periodontitis lesions". Oral Microbiol. Immunol., 2006. **21**: 269-282.
- [77] K. H. Tan, C. A. Seers, S. G. Dashper, H. L. Mitchell, J. S. Pyke, V. Meuric, N. Slakeski, S. M. Cleal, J. L. Chambers, M. J. McConville, and E. C. Reynolds, "*Porphyromonas gingivalis* and *Treponema denticola* exhibit metabolic symbioses". PloS Pathog., 2014. **10** (3): 1-11.
- [78] Y. Zhu, S. G. Dashper, Y. Chen, S. Crawford, N. Slakeski, and E. C. Reynolds, "*Porphyromonas gingivalis* and *Treponema denticola* synergistic polymicrobial biofilm development". PloS One., 2013. **8** (8): 1-8.
- [79] A. Smekal, "Zur quantentheorie der Dispersion". Naturwissenschaften, 1943. **11** (43): 873-875.
- [80] C.V. Raman, and K.S. Krishnan, "A new type of secondary radiation". Nature, 1928. **121** (3048): 501-502.
- [81] T. Cremer, and C. Cremer, "Considerations on a laser-scanning-microscope with high resolution and depth of field". Microscopica Acta, 1978. **81** (1): 31-44.
- [82] D. McMullan, "Von Ardenne and the scanning electron microscope". Proc. Roy Microsc. Soc., 1988. **23**: 283-288.
- [83] K. Smith, and C. Oatley, "The scanning electron microscope and its fields of application". British Journal of Applied Physics, 1955. **6** (11): 391-399.
- [84] M. Laue, "Zur theorie des Versuches von Trouton und Noble". Annalen der Physik, 1912. **343** (7): 370-384.
- [85] R. M. Bock, B. J. McEntire, B. S. Bal, M. N. Rahaman, M. Boffelli, and G. Pezzotti, "Surface modulation of silicon nitride ceramics for orthopaedic applications". Acta Biomater., 2015. **26**: 318-330.
- [86] S.I. Raider, R. Flitsch, J.A. Aboaf, and W.A. Pliskin, "Surface oxidation of silicon nitride films". J. Electrochem. Soc., 1976. **123**: 560-565.
- [87] D.P. Butt, D. Albert, and T.N. Taylor, "Kinetics of thermal oxidation of silicon nitride powders". J. Am. Ceram. Soc., 1996. **79**: 2809-2814.
- [88] B. D. Beier, R. G. Quivey, and A. J Berger, "Raman microspectroscopy for species identification and mapping within bacterial biofilms". AMB Express, 2012. **2** (35): 1-6.
- [89] I. Notingher, "Raman spectroscopy cell-based biosensors". Sensor 2007, **7**: 1343-1358.
- [90] K. Honda, S. Yokoyama, and S. Tanaka, "Assignment of the Raman active vibration modes of β -Si₃N₄ using micro-Raman scattering". J. of Applied Physics, 1999. **85** (10): 7380-7384.
- [91] N. Hirotsaki, R. Xie, and K. Kimoto, "Characterization and properties of green-emitting β -SiAlON: Eu²⁺ powder phosphors for white light-emitting diodes". Applied Physics Letter, 2005. **86**: 211905-3.
- [92] R. Kaindl, D. M. Többens, and V. Kahlenberg, "DFT-aided interpretation of the Raman spectra of the polymorphic forms of Y₂Si₂O₇". Raman J. Spectr., 2010. 1-8.

- [93] V. Kahlenberg, W. Wertl, D. M. Többens, R. Kaindl, P. Schuster, and H. Schottenberger, "Rietveld analysis and Raman spectroscopic investigations on α - $Y_2Si_2O_7$ ". *Z. Anorg. Allg. Chem.*, 2008. **643**: 1166-1172.
- [94] I. Rehman, Z. Movasaghi, and S. Rehman, "Vibrational spectroscopy for tissue analysis". *Series in Medical Physics and Biomedical Engineering*. Chapter 8, 212-294.
- [95] M. Tang, G. D. McEwen, Y. Wu, C. D. Miller, and A. Zhou, "Characterization and analysis of mycobacteria and Gram-negative bacteria and co-culture mixtures by Raman microspectroscopy, FTIR, and atomic force microscopy". *Anal. Bioanal. Chem.*, 2013. **405**: 1577-1591.
- [96] T. J. Moritz, C. R. Polage, D. S. Taylor, D. M. Krol, S. M. Lane, and J. W. Chan, "Evaluation of *Escherichia coli* cell response to Antibiotic Treatment by Use of Raman Spectroscopy with Laser Tweezers". *Clin. J. Microbiol.*, 2010. **48** (11): 4287-4290.
- [97] G. B. Jung, S. Won Nam, S. Choi, G. Lee, and H. Park, "Evaluation of antibiotic effects on *Pseudomonas aeruginosa* biofilm using Raman spectroscopy and multivariate analysis". *Biom. Opt. Exp.*, 2014. **5** (9): 1-14.
- [98] G. Bourgeau, and D. Mayrand, "Phenylacetic acid production by *Bacteroides gingivalis* from phenylalanine and phenylalanine-containing peptides". *Can. J. Microbiol.*, 1983. **29**: 1184-1189.
- [99] M. Struyvé, M. Moons, and J. Tommassen, "Carboxy-terminal Phenylalanine is essential for the correct assembly of a bacterial outer membrane protein". *J. Mol. Biol.*, 1991. **218**: 141-148.
- [100] H. De Cock, M. Struyvé, M. Kleerebezen, T. Van der Krift, and J. Tommassen, "Role of the Carboxy-terminal Phenylalanine in the biogenesis of outer membrane protein PhoE of *Escherichia coli* K-12". *J. Mol. Biol.*, 1997. **269**: 473-478.
- [101] H. Kumada, Y. Haishima, T. Umemoto, and K. Tanamoto, "Structural study on the free Lipid A isolated from *Lypopolisaccharide* of *Porphyromonas gingivalis*". *J. Bacter.*, 1995. **177** (8): 2098-2106.
- [102] E. T. Rietschel, T. Kirikae, F. U. Schade, U. Mamat, G. Schmidt, H. Loppnow, A. J. Ulmer, U. Zähringer, U. Seydei, F. Di Padova, M. Schreier, and H. Brade, "Bacterial endotoxin: molecular relationships of structure to activity and function". *FASEB J.*, 1995. **8**: 217-224.
- [103] K. Ishinara, H. Kuramitsu, T. Miura, and K. Okuda, "Dentilisin activity affects the organization of the outer sheath of *Treponema denticola*". *J. Microb.*, 1998. **180** (15): 3837-3844.
- [104] A. Sharma, "Virulence mechanisms of *Tannerella forsythia*". *Periodontol.* 2000, 2010. **54** (1): 106-116.
- [105] P. N. Tawakoli, A. Al-Ahmad, W. Hoth-Hannig, M. Hannig, and C. Hannig, "Comparison of different live/dead staining for detection and quantification of adherent microorganisms in the initial oral biofilm". *Clin. Oral Invest.*, 2013. **17**: 841-580.
- [106] G. Pezzotti, L. Puppulin, A. La Rosa, M. Boffelli, W. Zhu, B. J. McEntire, S. Hosogi, T. Nakahari, and Y. Marunaka, "Effect of pH and monovalent cations on the Raman spectrum of water: basics revised and application to measure concentration gradients at water/solid interface in Si_3N_4 biomaterial". *Chem. Phys.*, 2015. **463**: 120-136.
- [107] B. Fubini, E. Giamello, M. Volante, V. Bolis, "Chemical, Functionalities at the silica surface determining its reactivity when inhaled. Formation and reactivity of surface radicals". *Toxicol. Ind. Health*, 1990. **6**: 571-597.